

REPORT DOCUMENTATION PAGE			Form Approved OMB No. 0704-0188	
AD-A218 057			1b. RESTRICTIVE MARKINGS NONE	
			3. DISTRIBUTION / AVAILABILITY OF REPORT APPROVED FOR PUBLIC RELEASE; DISTRIBUTION UNLIMITED.	
4. PERFORMING ORGANIZATION REPORT NUMBER(S)			5. MONITORING ORGANIZATION REPORT NUMBER(S) AFIT/CI/CIA-89-144	
6a. NAME OF PERFORMING ORGANIZATION AFIT STUDENT AT UCLA		6b. OFFICE SYMBOL (if applicable)	7a. NAME OF MONITORING ORGANIZATION AFIT/CIA	
6c. ADDRESS (City, State, and ZIP Code)			7b. ADDRESS (City, State, and ZIP Code) Wright-Patterson AFB OH 45433-6583	
8a. NAME OF FUNDING / SPONSORING ORGANIZATION		8b. OFFICE SYMBOL (if applicable)	9. PROCUREMENT INSTRUMENT IDENTIFICATION NUMBER	
8c. ADDRESS (City, State, and ZIP Code)			10. SOURCE OF FUNDING NUMBERS	
			PROGRAM ELEMENT NO.	PROJECT NO.
			TASK NO.	WORK UNIT ACCESSION NO.
11. TITLE (Include Security Classification) (UNCLASSIFIED) QUANTIFYING AND REDUCING UNCERTAINTY IN THE ASSIMILATIVE MAPPING OF IONOSPHERIC ELECTRODYNAMICS				
12. PERSONAL AUTHOR(S) DELORES J. KNIPP				
13a. TYPE OF REPORT THESE /DISSERTATION		13b. TIME COVERED FROM TO	14. DATE OF REPORT (Year, Month, Day) 1989	15. PAGE COUNT 176
16. SUPPLEMENTARY NOTATION APPROVED FOR PUBLIC RELEASE IAW AFR 190-1 ERNEST A. HAYGOOD, 1st Lt, USAF Executive Officer, Civilian Institution Programs				
17. COSATI CODES			18. SUBJECT TERMS (Continue on reverse if necessary and identify by block number)	
FIELD	GROUP	SUB-GROUP		
19. ABSTRACT (Continue on reverse if necessary and identify by block number)				
<div style="text-align: center;">DTIC S ELECTE D FEB 15 1990 D as D</div> <div style="text-align: center; font-size: 2em; font-family: cursive;">90 02 14 049</div>				
20. DISTRIBUTION / AVAILABILITY OF ABSTRACT <input checked="" type="checkbox"/> UNCLASSIFIED/UNLIMITED <input type="checkbox"/> SAME AS RPT. <input type="checkbox"/> DTIC USERS			21. ABSTRACT SECURITY CLASSIFICATION UNCLASSIFIED	
22a. NAME OF RESPONSIBLE INDIVIDUAL ERNEST A. HAYGOOD, 1st Lt, USAF			22b. TELEPHONE (Include Area Code) (513) 255-2259	22c. OFFICE SYMBOL AFIT/CI

89-144

UNIVERSITY OF CALIFORNIA

Los Angeles

Quantifying and Reducing Uncertainty in the
Assimilative Mapping of Ionospheric Electrodynamics

A dissertation submitted in partial satisfaction of the
requirements for the degree of Doctor of Philosophy
in Atmospheric Science

by

Delores J. Knipp

1989

Accession For	
NTIS CRA&I	<input checked="checked" type="checkbox"/>
DTIC TAB	<input type="checkbox"/>
Unannounced	<input type="checkbox"/>
Justification	
By	
Distribution/	
Availability Codes	
Dist	Avail and/or Special
A-1	



The dissertation of Delores J. Knipp is approved

Arthur D. Richmond
Arthur D. Richmond

Nancy U. Crooker
Nancy U. Crooker

George L. Siscoe
George L. Siscoe

Robert L. McPherron
Robert L. McPherron

David D. Jackson
David D. Jackson

Richard P. Turco
Richard P. Turco

S.V. Venkateswaran
S. V. Venkateswaran, Committee Chair

University of California, Los Angeles

1989

This dissertation is dedicated to my family

Harold and Carmelita

Rosella

Sylvia

Juanita

Thelma

Vincent

Sharon

who gave so much encouragement and support

TABLE OF CONTENTS

I. CHAPTER 1: INTRODUCTION	1
II. CHAPTER 2: HISTORICAL PERSPECTIVE	3
Figure Captions	10
Figures	11
III. CHAPTER 3: THE AMIE PROCEDURE	12
I. Introduction	12
II. Technique	13
III. Uncertainty	17
IV. Error Propagation	24
V. Summary	28
Figure Captions	29
Figures	31
IV. CHAPTER 4: IONOSPHERIC CONDUCTION SOURCES, MEASURE- MENTS AND UNCERTAINTIES	36
I. Introduction	36
II. Ionization, X-ray sources and conductances	36
III. Instruments and errors	46
Figure Captions	59
Figures	62

V. CHAPTER 5: MAGNETIC PERTURBATIONS AND CURRENTS	75
I. Introduction	75
II. Phenomenology	75
III. Estimating currents, Electric fields, and Joule heating	81
Figure Captions	93
Figures	95
 VI. CHAPTER 6: SENSITIVITY	 101
I. Weightings	101
II. Goodness of Fit Tests	101
Figure Captions	104
Figures	105
 VII. CHAPTER 7: GEOPHYSICAL RESULTS	 110
I. Introduction	110
II. DP1 and DP2 Current System Variations	110
III. Response to IMF Variations for 23-24 July 1983	115
IV. Joule Heating	118
V. Summary	119
Figure Captions	120
Figures	123
 VIII. CHAPTER 8: SUMMARY	 141
I. Review	141
II. Future Work	143

APPENDIX I FITTING TECHNIQUES	
I. Standard Least Squares Estimation	145
II. Weighted Least Squares	146
III. Constrained Least Squares Fit	146
APPENDIX II OPTIMAL LINEAR ESTIMATION	148
I. Estimating \hat{s}	148
II. Uncertainty C_e	149
APPENDIX III CONDUCTION DERIVATIVES	152
APPENDIX IV ELECTRODYNAMIC RELATIONSHIPS	156
I. Horizontal Currents	156
II. Field-Aligned Currents	160
REFERENCES	161

FIGURE LIST

- Figure 2.1. Data Sources
- Figure 3.1. Assimilative Mapping of Ionospheric Electrodynamics Schematic
- Figure 3.2. Conductance Basis Functions
- Figure 3.3. Statistical Variability of Conductance
- Figure 3.4. Error Propagation Example
- Figure 3.5. Error Envelopes
- Figure 4.1. Pedersen Conductance Model
- Figure 4.2. Spatial Relationships Between Plasma Sheet and Aurora
- Figure 4.3. Empirical Values of Conductance (Robinson et al., 1987)
- Figure 4.4. Altitude Profiles of Electron Density, Pedersen and Hall
Conductance
- Figure 4.5. Graph of Fuller-Rowell and Evan's (1987) Conductance Look-Up
Functions
- Figure 4.6. Bremsstrahlung Production Functions (Gorney et al., 1986)
- Figure 4.7. Bremsstrahlung Deconvolution (Gorney et al., 1986)
- Figure 4.8. Examples of Data Coverage
- Figure 4.9. Evolution of Conductance Estimates
- Figure 4.10. Conductance Uncertainty
- Figure 4.11. Time Series of Geophysical Variations--January 1984
- Figure 4.12. Pedersen Conductance and Electric Potential 1810, 1950 and
2130 UT.
- Figure 4.13. Pedersen Conductance and Electric Potential 2320, 0100 and
0240 UT.
- Figure 5.1. Average and Instantaneous Field-Aligned Current Patterns

- Figure 5.2. DP1 and DP2 current system diagrams (Clauer and Kamide, 1985)
- Figure 5.3. Magnetic Perturbations, Magnetic Potential and Equivalent Current
- Figure 5.4. Idealized Magnetic Perturbation Distributions Due to Overhead Current
- Figure 5.5. Impact of Vertical Component of Ground Magnetic Data
- Figure 5.6. Impact of Satellite Magnetometer Data.
- Figure 6.1. Weighting Ratio for 23-24 July 1983
- Figure 6.2. Fit Ratio for 23-24 July 1983
- Figure 6.3. Impact of Vertical Component of Ground Magnetic Data
- Figure 6.4. Impact of Satellite Magnetometer Data
- Figure 6.5. Data Contributing to Estimates in Figure 6.4
- Figure 7.1. IMF Data, Geophysical and Derived Parameters for 19 September 1984
- Figure 7.2. The AU and AL Indices for September 1984
- Figure 7.3. Comparison of Derived and Statistical Electric Potential Values for 19 September 1984
- Figure 7.4. Fitted Electrodynamic Patterns for 0950 UT 19 September 1984
- Figure 7.5. Fitted Electrodynamic Patterns for 1050 UT 19 September 1984
- Figure 7.6. Fitted Electrodynamic Patterns for 1150 UT 19 September 1984
- Figure 7.7. Fitted Electrodynamic Patterns for 1430 UT 19 September 1984
- Figure 7.8. Fitted Electrodynamic Patterns for 1530 UT 19 September 1984
- Figure 7.9. Fitted Electrodynamic Patterns for 1630 UT 19 September 1984
- Figure 7.10. IMF Data, Geophysical and Derived Parameters for 19 September 1984

- Figure 7.11. Electric Potential Plots for 0830-1100 UT 23 July 1983**
- Figure 7.12. Electric Potential Plots for 1130-1400 UT 23 July 1983**
- Figure 7.13. Electric Potential Plots for 1430-1700 UT 23 July 1983**
- Figure 7.14. Electric Potential Plots for 1730-2000 UT 23 July 1983**
- Figure 7.15. Electric Potential Plots for 1030-1000 UT 23 July 1983 (10 minute increments) and Comparison with Ahn et al. (1988) Results**
- Figure 7.16. Comparison of Crooker (1988) Convection Reversal Model with AMIE Results**
- Figure 7.17 Globally Integrated Joule Heating Time Series for 19 September and 23-24 July 1983**
- Figure 7.18. Joule Heating Patterns Produced Under Varying IMF Conditions**

ACKNOWLEDGEMENTS

This dissertation would not have been possible without the assistance of a large number of people. First and foremost, Dr. Art Richmond provided the basic procedure. He also provided encouragement and large doses of patient explanation. Dr. S. V. Venkateswaran gave me just the right amount of guidance and direction. The discussions and classroom interaction I had with Dr. David Jackson, Dr. Nancy Crooker, Dr. Bob McPherron, Dr. Richard Turco and Dr. George Siscoe were in many ways crucial to my understanding of the geophysical problems that can be tackled with the AMIE procedure. I also had many useful discussions with Dr. Geoff Crowley and Dr. Barbara Emery.

Data were provided by a number of principle investigators: Dr. David Evans provided NOAA satellite data, Dr. Fred Rich provided DMSP F/7 satellite data and Dr. David Gorney provided DMSP F/6 X-ray data. Ground magnetometer data came from the World Data Center A, courtesy of Dr. Herb Kroehl and Mr. Chris Wells and from Dr. E. Friis-Christensen of Greenland. Dr. J. A. Waldock provided SABRE coherent scatter radar data.

I am grateful to the U. S. Air Force for a scholarship which facilitated this work and to NCAR for a grant of computer time which allowed me to get the research started.

This study made use of the NCAR Incoherent-Scatter Radar Data Base, which along with the Millstone Hill and Sondrestrom radars is supported by the National Science Foundation. The Sondrestrom radar is supported by NSF grant ATM 85-16436. The Millstone Hill Radar is supported by NSF grant ATM 84-19117. The EISCAT Scientific Association is supported by Centre National de la Recherche Scientifique of France, Suomen Akatemia of Finland, Max-Planck-Gesellschaft of Germany, Norges Almenvitenskapelige Forskningsrad

of Norway, Naturvetenskapliga Forskningsradet of Sweden and the Science and Engineering Research Council of the United Kingdom.

There are a number of people who "lightened the load" for me. Ms. Louise Beierle assisted with typing manuscripts. Mr Ben Foster and the Scientific Computing Division staff at the National Center for Atmospheric Research (NCAR) assisted in programming and problem solving. Corky and Lee Fortier simply put up with me during long visits to Boulder. Finally, I must thank my sister Sharon without whom I never would have finished on time.

I would like to acknowledge use of several *Journal of Geophysical Research (JGR)* figures from various authors. The following figures have been extracted from *JGR* under the standard *JGR* consent agreement:

Figure 3.1 from Richmond and Kamide (1988)

Figure 4.2 from Lui et al. (1977)

Figure 4.4 from Brekke et al. (1974)

Figure 5.1 from Iijima and Potemra (1976)

Figure 5.2 from Clauer and Kamide (1985)

Figure 7.1 from Knipp et al. (1989)

Figure 7.3 from Knipp et al. (1989)

Figure 7.16 after Crooker (1988)

I would also like to acknowledge use of the following non-copyright material:

Figure 4.6 from Gorney et al. (1986)

Figure 4.7 from Gorney et al. (1986)

Figure 7.15 from Ahn et al. (1988).

VITA

December 20 1954	Born, Jefferson City Missouri
1976	B. S., Atmospheric Science University of Missouri Columbia, Missouri
1976	Commissioned U. S. Air Force Weather Officer
1984	M. S., Atmospheric Science University of Missouri Columbia, Missouri
1984	Instructor of Physics U.S. Air Force Academy Colorado Springs, Colorado
1988	M. S., Atmospheric Science University of California Los Angeles, California

PUBLICATIONS AND PRESENTATIONS

Knipp, D. J. The use of localized satellite observations for determining high-latitude electric fields and currents, M. S. Thesis, University of California, Los Angeles, 1988.

Knipp, D. J., A. D. Richmond, F. J. Rich, and D. S. Evans, The use of combined satellite and ground-based observations for determining high-latitude electric fields and currents, Proceedings of the Cambridge Workshop on Theoretical Geoplasma Physics, in press, 1989.

Knipp, D. J., A. D. Richmond, G. Crowley, O. de la Beaujardiere, E. Friis-Christensen, D. S. Evans, J. C. Foster, I. W. McCreia, F. J. Rich and J. A. Waldock, Electrodynamic Patterns for September 19, 1984, J. Geophys. Res. in press, 1989.

Knipp, D. J., A. D. Richmond, F. J. Rich, and D. S. Evans, Conductance Patterns for GISMOS: 18-19 January, 1984. Paper presented at the Fall 1988 American Geophysical Union Meeting, San Francisco, CA.

Knipp, D. J., A. D. Richmond, G. Crowley, Ionospheric Electric Fields During the Equinox Transition Study. Paper presented at the Fall 1988 American Geophysical Union Meeting, San Francisco, CA.

Knipp, D. J., A. D. Richmond, F. J. Rich, and D. S. Evans, Conductance Patterns for 19 September 1984-Equinox Transition Study. Paper presented at the Spring 1989 American Geophysical Union Meeting, Baltimore, MA.

ABSTRACT OF THE DISSERTATION

Quantifying and Reducing Uncertainty in the Assimilative Mapping of Ionospheric Electrodynamics

by

Delores J. Knipp

Doctor of Philosophy in Atmospheric Science

University of California, Los Angeles, 1989

Professor S. V. Venkateswaran, Chair

We have applied the Assimilative Mapping of Ionospheric Electrodynamics (AMIE) procedure, developed by Richmond and Kamide, (*JGR*, p. 5741, 1988) to three periods: 23-24 July 1983, 18-19 January 1984 and 19 September 1984. The mapping procedure obtains optimal estimates of electrodynamic patterns from basis functions multiplied by an appropriate set of coefficients which are determined from a constrained least squares fit to the data. We show the impact of several additions to the procedure and analyze some of the geophysics implied by our results. New estimates of auroral conductance are incorporated from satellite particle detectors and a satellite X-ray imager. We use this new information to produce global estimates of conductance and to study the effect of uncertainty in those estimates on the estimates of the polar electric field structure. We also incorporate new (but somewhat indirect) observations relating to the electric field: satellite magnetometer data and the vertical component of the ground magnetometer data. The addition of these data, as well as, increasing the number of estimated coefficients tend to reduce

2. Disinfectants. (40%)

QUANTIFYING AND REDUCING UNCERTAINTY IN THE ASSIMILATIVE MAPPING OF IONOSPHERIC ELECTRODYNAMICS

CHAPTER 1 INTRODUCTION

The high-latitude ionosphere is a region of linkage between the earth's magnetosphere above and the neutral atmosphere below. Accurate assessment of the electrodynamic state of the high-latitude ionosphere is important for modelling magnetospheric and ionospheric currents and plasma flows and for understanding the phenomena of ion drag and Joule heating in the neutral atmosphere. The ionosphere's impact on radio communication provides a practical consideration for timely assessment of the ionospheric state.

This dissertation deals with the general topic of high-latitude ionospheric electrodynamic variability. While this variability is visually easy to observe, as in the case of the aurora, it has proven difficult to quantify. Only within the last forty years have sufficiently powerful and sensitive instruments such as incoherent scatter radar and satellite magnetometers been available for determining such fundamental values as electric field intensity and current density at a given location or range of locations.

The development of these instruments, as well as improvements in spacecraft technology and international cooperation have aided in the acquisition of large data bases that can be used to describe average values of many high-latitude parameters, but descriptions of large scale, instantaneous electrodynamic variations are still on the forefront of ionospheric research. Dr. Arthur Richmond of the National Center for Atmospheric Research High

Observatory has recently designed a procedure for mapping variations in high-latitude electrodynamics. The procedure, known as the Assimilative Mapping of Ionospheric Electrodynamics (AMIE) procedure, incorporates a variety of direct and indirect electrodynamic measurements to yield coherent patterns of high-latitude conductances, electric fields and electric currents. In a recent publication Richmond and Kamide (1988) described this technique and suggested several possible additions that might improve the reliability of the procedure. I have chosen three of these for my dissertation research: (1) improving the estimates of auroral conductance patterns used to link the magnetic perturbations and the electric field, (2) including the vertical component of the ground magnetic perturbations in the mapping procedure and (3) further investigation into the utility of satellite magnetometer measurements for aiding in the electric field estimation.

In chapter 2 of this dissertation a short historical perspective of the studies of electrodynamic variations will be given. Chapter 3 contains a description of Richmond and Kamide's assimilation technique and some important specifics of the procedure. Chapter 4 provides the physical background of the high-latitude conductance variations and the impact of adding conductance measurements to the assimilation process. Chapter 5 is devoted to an analogous discussion of the high-latitude current systems. Results from sensitivity studies are presented in chapter 6. Chapter 7 contains results from selected case studies, along with appropriate geophysical interpretations. Chapter 8 summarizes the work in this dissertation and provides a broad outline of future work.

CHAPTER 2

HISTORICAL PERSPECTIVE

Auroral observations no doubt predate written history, but association between auroral and geomagnetic activity is a relatively recent one. Halley suggested a link between auroral activity and the geomagnetic field in 1621 and Celsius advanced the theory by relating auroral fluctuations and geomagnetic disturbances in 1741. The 19th century saw rather diverse and important accomplishments in the field of geophysics. Gauss's mathematical method of separating the geomagnetic field into its internal and external components, which laid the foundation for present day magnetometer studies, was published in 1839. Angström made the first observations of the auroral spectrum in 1868. By 1882 B. Stuart had hypothesized a connection between the sun and geomagnetism and developed the basic idea of an electrically conducting atmosphere.

In 1901 Marconi used, what we now know to be, the ionosphere to bounce the first artificial radio waves across the Atlantic Ocean. This led to further investigation of the conducting region by Heaviside in 1902. Such investigations continued into the early 1920's when Appleton and Barnett (1926) found evidence of the E layer and Bruit and Tuve (1925) began ionospheric sounding. Magnetic studies also figured into geomagnetic investigations in the early part of this century. In 1908 Birkeland used magnetic data to suggest that the polar current system was three-dimensional. In the 1930's Chapman began the study of equivalent current systems, coining the term "electrojet" as his investigations progressed. In 1931 he produced the theory of ionospheric layering.

Magnetometer data became the mainstay of geomagnetic analyses between 1930 and 1958. One of the first "coordinated campaigns" was carried out in the Second Polar Year (1931-1932). Such noted scientists as Vestine, Harang and Fukushima studied the equivalent current systems derived from ground magnetometer data taken during that period. Also during that era (1939) Alfvén proposed a horizontal ionospheric current system fed by magnetospheric field-aligned currents. But Chapman in 1935 had pointed out that ground magnetometer data could not be used to uniquely determine the contributions that field-aligned currents might make to the horizontal electrojets.

The International Geophysical Year (IGY) 1957-1958 brought a virtual explosion of new instruments, analysis techniques and theories. Theories on the solar-wind magnetosphere-ionosphere interaction were proposed by Dungey (1961) and Axford and Hines (1961). Dungey proposed an open model of the system in which tubes of the earth's magnetic flux are convected from the dayside to the nightside by merging the Interplanetary Magnetic Field (IMF) with the earth's field. This process would produce twin vortices of convection in the high-latitude ionosphere. Dungey also suggested the possibility of connection when a northward IMF prevailed. Axford and Hines suggested a "closed model" viscous interaction between the solar wind and the magnetopause as the driver of the two cell convection pattern.

In the early 1960's rocket probing of the aurora provided the first information on energy distributions of the precipitating auroral particles and all sky-cameras became an important tool for studying the behavior of the aurora (Akasofu, 1964). During that decade Boström (1964) proposed a theoretical three-dimensional current system, but Fukushima (1969) asserted that three

dimensional nature could not be determined from ground data alone. Although early satellite missions confirmed the presence of the ring current and the Chapman-Ferraro (magnetopause current) the question of field-aligned currents remained unsettled through the 1960's.

In 1970 Vasyliunas presented a self-consistent coupling scheme for the ionosphere magnetosphere system. The satellite and radar measurements of the early 1970's were used to verify the basic elements of this model as well as others derived from IGY data. The Atmospheric Explorer (AE) satellite confirmed the presence of the two cell convection pattern (Heppner, 1972 and 1977). Armstrong and Zmuda (1973) showed indisputable evidence of field-aligned currents from TRIAD satellite data. Satellites were also used to image and analyze the large scale structures of the aurora. Kamide and Rostoker (1977) used satellite magnetometer data, auroral imagery and particle precipitation measurements from Defense Meteorological Satellite Programs (DMSP) satellites to study the spatial relationships between field-aligned currents and the aurora. DMSP images were also used to examine the complexity and variations of nightside auroral forms (Akasofu, 1976). Chatanika incoherent scatter radar began providing coordinated measurements of conductance and ion drifts to yield local estimates of currents and electric fields (Brekke et al., 1974). Millstone Hill radar was used to study auroral convection patterns (Evans et al., 1980).

Despite increasing satellite coverage surface magnetic observations continued to provide the bulk of global geophysical measurements. Ground magnetic perturbations were coupled with model electric field and current systems to study theoretical links between the ionosphere and magnetosphere (McPherron et al., 1973 and Kawasaki et al., 1974). Russell (1972) suggested

solar wind-magnetosphere interaction associated with IMF B_z northward. Shortly thereafter, equivalent current patterns for such interactions were analyzed by Maezawa (1976). Meridian chains of magnetometers have made possible spatially detailed examination of current systems. Hughes and Rostoker (1977) and Akasofu et al. (1979) used data from these chains to study the relationship between field-aligned currents and the auroral electrojet.

Progress in geophysical research in the last 10-15 years can be broadly associated with four areas: (1) The development of large statistical data bases, (2) continuing improvement in spacecraft instrumentation and longevity, (3) improvements in computational efficiency and (4) coordinated data acquisition and analysis campaigns.

Data from satellites whose orbits periodically exit the magnetosphere to the solar wind and return have been crucial to specifying parameters such as solar wind velocity and plasma density and the magnitude and direction of the IMF components (Russell and McPherron, 1973). Such information has provided verification for computer simulations of solar wind-magnetosphere-ionosphere linkage (Harel et al., 1981a and 1981b and Crooker and Siscoe, 1981) and allowed scientists to correlate solar wind parameters with various modes of magnetospheric behavior (Russell, 1972) and substorm activity and energy deposition in the magnetosphere (Perreault and Akasofu, 1978) and electrical variations in the polar cap (Reiff and Burch, 1985 and Reiff and Luhmann, 1986).

Iijima and Potemra (1976a) published results from one of the first large data bases to be accumulated from satellite data. Their diagrams of average field-aligned current distributions are now classic representations of our understanding of the three dimensional nature of the ionosphere-

magnetosphere interaction. More recent satellite studies have provided insight into the current distributions associated with IMF B_z northward conditions. Foster et al. (1986) have binned nearly a decade of high-latitude plasma drift measurements from Millstone Hill according to level of magnetic activity, magnetic latitude and magnetic local time. From these data they have derived statistical patterns of ionospheric convection associated with ten levels of geomagnetic activity. Conductance estimates derived from 8 years of NOAA-TIROS satellites have been similarly binned by Fuller-Rowell and Evans (1987) to provide statistical patterns of Hall and Pedersen conductance. Hardy et al. (1987) have assembled a large data base of DMSP particle precipitation data from which they provide global maps of energy and number flux as well as Hall and Pedersen conductances for different levels of K_p . Rich et al. (1987) have coupled DMSP satellite magnetometer data and particle precipitation data for the purpose of developing statistical patterns of Joule heating. Satellite data have also figured into the development of comprehensive empirical models of polar cap convection developed by Heppner and Maynard (1987).

Kamide (1988) points out that the International Magnetosphere Study (1976-1979) coincided with the development of advanced numerical schemes designed to compute global distributions of ionospheric currents and field-aligned currents and self-consistent electric field distributions from ground magnetic data (Kisabeth, 1979, Mishin et al., 1979, Kamide et al., 1981). Kisabeth (1979) inverted ground magnetic data to derive a three dimensional current system. Ohm's Law and an assumed conductance pattern yielded the global electric field distribution. Kamide, Richmond and Matsushita (1981), in their KRM method, inverted ground magnetic perturbations to yield an equivalent current function that can be related (with assumed conductance

patterns) to the electric field distribution through second order differential equations. Applications of Ohm's Law to their results provides ionospheric currents. One shortcoming common to these investigations has been the reliance on simple conductance distributions which do not accurately link the ionospheric currents and electric fields.

In a partial answer to this problem Ahn et al., (1983) have used regression analysis to find empirical relations between conductance estimates from Chatanika radar and horizontal magnetic perturbations at College, Alaska. These relations can be applied to other auroral zone magnetometers to provide a more global estimate of conductance distribution. Mishin et al. (1986) have suggested that gradients in ground magnetic perturbations may also be used to estimate conductance. As we discuss in Chapter 4, satellite particle precipitation measurements can be combined with empirical models (Spiro et al., 1982 and Robinson et al., 1987) to estimate conductance below the satellite track (Fuller-Rowell and Evans, 1987 and Rich et al., 1987). Additionally, a broad spectrum of satellite imagery of the auroral zones is making global estimates of auroral conductances possible. Kamide et al. (1986), Rees et al. (1988), Kamide et al. (1989) and Robinson et al. (1989) used Dynamics Explorer (DE) ultraviolet imagery to improve global conductance estimates. Marklund et al. (1988) used similar images from the Viking satellite. Imhof et al. (1984), Rosenberg et al. (1987), Ahn et al. (1988) investigated bremsstrahlung X-ray images to estimate high-latitude conductance.

The focus of this investigation, the AMIE procedure, employs a constrained least squares fit of data to estimated electrodynamic distributions, and has the capability of incorporating conductance data to better define the

conductance distributions linking the current distributions to the electric field. The constraints, in the form of *a priori* information essentially stretch the information content of sparse observations and cause the estimated patterns to adhere to statistically reasonable values in regions of limited data. Additionally, AMIE incorporates a larger variety of near simultaneous data and provides quantitative estimates of the uncertainty in the derived distributions. The approach is a probabilistic one in terms of fitting the patterns to the data as opposed to an iterative solution of second order differential equations as in the KRM method.

The new emphasis on coordinated campaigns makes data assimilation procedures such as AMIE an important analysis tool. Data provided by the multitude of instruments operating during campaigns can be put into a global context with the aid of such procedures. Figure 2.1 shows the types of data incorporated into AMIE for one non-campaign period: 23-24 July 1983 and two campaign periods: 18-19 January 1984, the Global Ionospheric Modelling of Ionospheric Substorms (GISMOS) period and 19 September 1984, the Equinox Transition Study (ETS) period .

The following chapters discuss the AMIE procedure and the assimilated data and show the AMIE capability of deriving coherent electrodynamic patterns during a variety of seasons and geomagnetic conditions.

FIGURE CAPTION FOR CHAPTER 2

Figure 2.1 Data sources for AMIE procedure

X - indicates data originally incorporated by Richmond and Kamide (1988) or Richmond et al. (1988)

- indicates data type previously used in AMIE procedure but new to the period of investigation

* - indicates new data source assimilated for this study.

	JUL 23-24, '83	JAN 18-19, '84	SEP 19, '84
1. CONDUCTANCE			
ISR Radars			
EISCAT	#	X	#
Sondrestrom	#	X	#
Satellite Particles			
NOAA-6,-7 and or-8 North and South Pole	⊗	⊗	⊗
DMSP F/7		⊗	⊗
Satellite Images			
DMSP F/6 X-RAY	⊗	⊗	
Magnetometers			
Ahn et al. (1983)	#	X	#
2. ELECTRIC FIELDS			
Magnetometers			
Horizontal Comp	#	X	#
Vertical Comp	⊗		⊗
ISR Radars			
Millstone Hill	#	X	#
EISCAT		X	#
Sondrestrom	#	X	#
Coherent Scatter Radar			
SABRE		⊗	⊗
Satellite Magnetometer			
DMSP F/7		⊗	⊗

Figure 2.1

CHAPTER 3

THE AMIE PROCEDURE

I. INTRODUCTION

The large scale features of the high-latitude ionospheric electrodynamic patterns are generally well-behaved, continuous functions or distributions. The objective of this study is to estimate several fundamental distributions from a variety of physical measurements which are not spatially or temporally uniform. Further, some of the measurements provide only indirect information about the fields and distributions to be estimated. The process by which these data are assimilated into coherent electrodynamic patterns is the Assimilative Mapping of Ionospheric Electrodynamics (AMIE) procedure. This procedure, which has been developed and described by Richmond and Kamide (1988), is essentially a constrained least squares fit of the data to the estimated distributions. Specifically, the task is to describe physical features in terms of basis functions multiplied by appropriate expansion coefficients. The task is accomplished by using the data to estimate the coefficients.

Figure 3.1 is a schematic of the procedure. It highlights the central problem of determining a set of coefficients that can mathematically describe a wide variety of the electrodynamic features present at any given time in the high-latitude ionosphere. The sets of coefficients in use at any given time are derived both from *a priori* information and from observations via a linear inversion.

The data which may be incorporated into the AMIE procedure are also shown in Fig. 3.1. In general, the observations should provide all or most of the information about the coefficients. For some cases, however, observations of one type or another may not be available. In data sparse regions the AMIE

technique relies partly on statistical information to reconstruct reasonable electrodynamic patterns. In this manner we bypass the typical non-uniqueness problems usually associated with data poor regions.

II. TECHNIQUE

A. BASICS

In many cases it is possible to express inverse problems in a linear parametric form where the observations, ω , are a linear combination, L , of the unknown parameters, a , which we would like to estimate. Mathematically, the statement is

$$\omega = La + v \quad 3.1$$

where ω is a column vector containing J observations, a is a column vector of I unknown parameters, and L is a known $J \times I$ matrix consisting of I basis functions, L_i , evaluated at each of J observing points and v is a column vector of J random errors. The elements of v are presumed to have zero mean and known variances. We seek to estimate a from the observations we have, but if the observations are sparse, nonexistent or contain large errors then we are willing to use *a priori* information to aid in the estimation.

One can decompose a set of observations ω into average (expected) values and deviations therefrom:

$$\omega = \langle \omega \rangle + z \quad 3.2$$

The expected values can be determined from averages of large data sets. For example, Foster et al. (1986) provided average electric potential values and Fuller-Rowell and Evans (1987) provided average conductance values that are used in this study.

The set of coefficients, a , to be estimated from these data can be similarly decomposed:

$$\mathbf{a} = \langle \mathbf{a} \rangle + \mathbf{s} \quad 3.3$$

In this equation the column vector \mathbf{s} contains the deviation coefficients. Since the expected values have been pre-determined the focus of our study becomes the deviation coefficients. The relation between the deviation coefficients (model parameters) and the deviation observations is

$$\mathbf{z} = \mathbf{L} \mathbf{s} + \mathbf{v} \quad 3.4$$

where the matrices are dimensioned as in equation 3.1. In principle an infinite number of coefficients are needed for this estimation. We nominally calculate 121 coefficients and assign variations associated with the remaining coefficients to form a part of the noise or error in the estimation procedure (as we will discuss later we can calculate up 196 coefficients). This truncation error resides in the elements of the matrix \mathbf{v} along with the observational errors.

B. OPTIMIZATION

Optimal estimation theory (Liebelt, 1967) tells us that optimal estimates, $\hat{\mathbf{s}}$, of the unknown coefficients, \mathbf{s} , can be uniquely determined from a linear combination of observations:

$$\hat{\mathbf{s}} = \mathbf{A} \mathbf{z}. \quad 3.5$$

The form of \mathbf{A} is shown in Appendix I for three different cases: simple least squares, weighted least squares and constrained least squares. The last case is the one that we will use here.

In the AMIE procedure we optimize estimates of three independent sets of coefficients: the electric field coefficients and the Hall and Pedersen conductance coefficients. Richmond and Kamide (1988) showed how to optimize the estimates for the electric field. Since this study deals more with conductance estimation, we will explain how the conductance estimates are optimized. In the following example we consider a "general" conductance

estimate appropriate to either the Pedersen or Hall coefficients. The terminology and notation follow that of Richmond and Kamide (1988). One note of caution is necessary in the terminology: There are no instruments that measure conductance. As explained in the next chapter, all conductance "observations" are derived from other more basic measurements. For ease of discussion we will nonetheless refer to these derived quantities as observations.

-
- 1) We first transform the actual conductance observations, Σ , by dividing by the statistical (*a priori*) value, Σ_0 , appropriate to the location and taking the logarithm of this ratio:

$$z_j = \ln \left(\frac{\Sigma_j}{\Sigma_{0j}} \right) = \sum_{i=1}^I L_{ji} s_i + v_j. \quad 3.6$$

In this equation z_j becomes the transformed observation. This transformation allows us to deal with the highly variable nature of the conductance while maintaining linearity in the estimation procedure.

- 2a) A linear combination of the observations will be formed in the following manner:

$$\hat{s}_i = \sum_{j=1}^J A_{ij} z_j \quad 3.7$$

- 2b) The true and estimated deviation fields are given by

$$\sigma \equiv \ln \left[\frac{\Sigma}{\Sigma_0} \right] = \sum_{i=1}^I s_i L_i(\theta, \phi) \quad 3.8$$

$$\text{and} \quad \hat{\sigma} \equiv \ln \left[\frac{\hat{\Sigma}}{\Sigma_0} \right] = \sum_{i=1}^I \hat{s}_i L_i(\theta, \phi) \quad 3.9$$

respectively, where θ is co-latitude and ϕ is longitude.

2c) We optimize \hat{s} by minimizing the expected value of the difference of these two quantities over the polar region ($\theta < \theta_0 = 34^\circ$).

$$\left\langle \int_0^{\theta_0} d\theta \int_0^{2\pi} \sin\theta d\phi (\hat{s}_i - s_i)^2 \right\rangle = \min. \quad 3.10$$

2d) Assuming that the basis functions, L_i are orthonormal allows us to write

$$\int_0^{\theta_0} d\theta \int_0^{2\pi} \sin\theta d\phi L_k \cdot L_i = \begin{cases} 2\pi(1 - \cos\theta_0) & k = i \\ 0 & k \neq i. \end{cases} \quad 3.11$$

3.8 and 3.9 can be substituted into 3.10 to yield

$$\begin{aligned} & \left\langle \int_0^{\theta_0} d\theta \int_0^{2\pi} \sin\theta d\phi \left(\sum_{i=1}^I (\hat{s}_i - s_i) L_i - r \right)^2 \right\rangle \\ &= 2\pi(1 - \cos\theta_0) \left(\sum_{i=1}^I \langle (\hat{s}_i - s_i)^2 \rangle + \langle \bar{r}^2 \rangle \right) \rightarrow \min \end{aligned} \quad 3.12$$

$r = \sum_{i=1}^I s_i L_i$ where $\sum_{i=1}^I s_i L_i$ is the sum of truncated errors for \hat{s} and \bar{r}^2 is the mean square value of r poleward of θ_0 .

3a) Setting the partial derivatives with respect to each A_{ij} equal to zero yields

$$\frac{\partial}{\partial A_{ij}} \left\{ \sum_{i=1}^I \left\langle \left(\sum_{j=1}^J A_{ij} z_j - s_i \right)^2 \right\rangle + \langle \bar{r}^2 \rangle \right\} = 0 = 2 \left\langle z_i \left(\sum_{j=1}^J A_{ij} z_j - s_i \right) \right\rangle \quad 3.13$$

3b) Rearranging gives

$$\sum_{j=1}^J A_{ij} \langle z_i z_j \rangle = \langle z_i s_i \rangle \quad 3.14$$

$$\text{or} \quad \mathbf{A} \langle \mathbf{z} \mathbf{z}^T \rangle = \langle \mathbf{z} \mathbf{s}^T \rangle. \quad 3.15$$

3c) The solution for \mathbf{A} in 3.15 is

$$\mathbf{A} = \mathbf{C}_{sz} \mathbf{C}_z^{-1} \quad 3.16$$

where $C_z \equiv \langle zz^T \rangle$ and $C_{sz} \equiv \langle sz^T \rangle$.

4.) The estimated conductance is derived from using equations 3.5 and 3.9 and then applying

$$\hat{\Sigma} = \Sigma_0 \exp \left[\sum_{i=1}^I \hat{s}_i L_i \right] \quad 3.17$$

The discussion in Appendix I indicates why we must use a generalized least squares fitting procedure in the mapping procedure if we are to incorporate both observations and prior information. Derivations provided by Liebelt (1967), Jackson (1979) and Richmond and Kamide (1988) are combined in Appendix II to show that

$$C_{sz} = C_s L^T + C_{sv} \quad 3.18$$

$$C_z = (L C_s L^T + C_{sv}^T L^T + L C_{sv} + C_v) \quad 3.19$$

where C_{sv} is the cross variance between the model parameter vector, s , and the error vector, v , and C_v is the error covariance matrix. By assuming statistical independence between s and v we may set C_{sv} to zero and arrive at

$$A = (C_s L^T) (L C_s L^T + C_v)^{-1} \quad 3.20$$

Further matrix manipulation (see Appendix II) gives

$$A = (L^T C_v^{-1} L + C_s^{-1})^{-1} L^T C_v^{-1} \quad 3.21$$

Using these results in equation 3.5 yields:

$$\hat{s} = (C_s L^T) (L C_s L^T + C_v)^{-1} z = (L^T C_v^{-1} L + C_s^{-1})^{-1} L^T C_v^{-1} z \quad 3.22$$

as the best (minimum variance) estimate of s .

III. UNCERTAINTY

A. CALCULATIONS

Not only does the product of the variance matrices and basis functions yield an estimate of the coefficients for the derived fields and distributions, but, from an appropriate combination of these matrices we can calculate a measure

of the uncertainty in the derived distribution. Additionally, the individual elements of the multiplication allow us to determine what role the observations and the prior data are playing in the estimation. The minimization of equation 3.12 corresponds to minimization of the trace of the covariance matrix $C_{\hat{s}-s}$ defined by

$$C_{\hat{s}-s} = \langle (\hat{s} - s)(\hat{s} - s) \rangle \quad 3.23$$

We cannot calculate the individual errors $\hat{s} - s$ for an individual case because we do not know the true value of s . We can, however, calculate the expected mean square values of the errors and their cross correlations contained in equation 3.23. As shown in Appendices I and II the matrix A which minimizes the trace of $C_{\hat{s}-s}$ produces the result

$$C_{\hat{s}-s} = (L^T C_v^{-1} L + C_s^{-1})^{-1} \quad 3.24$$

(1) (2)

The right hand side contains both data errors, indicated by term (1), and resolving errors, indicated by term (2). Both terms propagate uncertainty into the estimated coefficients. The data errors propagate uncertainty from the observations into the estimates while the resolving error propagates uncertainty caused by fitting to the prior information (versus the observations) into the estimates. The larger the errors associated with the observations (C_v large) the greater the reliance on the prior information contained in C_s .

One might argue that eliminating term (2) would improve the fit to the observations and thus give a better result. Our reason for including the prior information is to (1) guarantee the existence of the inverse in equation 3.24 and (2) constrain the coefficients to reasonable physical values, where "reasonable" is defined by the prior knowledge. Removing the prior information could have obvious disastrous consequences. Therefore both

terms on the right hand side of equation 3.24 are essential to the estimation process. The elements of equation 3.25 merit further discussion since they provide a quantitative means of specifying the error in the estimated fields.

B. ELEMENTAL CALCULATIONS AND COMPOSITION

1. Basis Functions, L_i

For purposes of comparison this discussion closely follows the discussion on electric potential basis functions provided by Richmond and Kamide (1988). We specify that the basis functions, L_i , be orthonormal and that they be capable of reproducing any possible large scale high-latitude conductance pattern. Small scale features that cannot be reproduced are attributed to the truncation of the infinite series at i ($=121$) terms. The basis functions are constructed from generalized associated Legendre functions.

Specifically,

$$\begin{aligned} L_i &= K_{1i} P_n^{i|m|}(\cos \theta) f_m(\phi) & \theta < \theta_0, \theta > \pi - \theta_0 \\ &= K_{2i} [\cot^m(\theta/2) + \tan^m(\theta/2)] f_m(\phi) & \theta_0 < \theta < \pi - \theta_0 \end{aligned} \quad 3.25$$

where

$$\begin{aligned} f_m(\phi) &= \sqrt{2} \cos m\phi & m < 0 \\ &= 1 & m = 0 \\ &= \sqrt{2} \sin m\phi & m > 0 \end{aligned} \quad 3.26$$

and θ_0 is the co-latitude of the transition between high-latitude behavior and the region where the auroral enhancement of the conductance is small (which we choose to be 34°). The normalizing constants K_{1i} and K_{2i} cause equation 3.11 to be satisfied as well as causing L_i to be continuous at θ_0 . The longitudinal wavenumber, m , is a unique function of the index i and P_n^m is a generalized associated Legendre function with non-integral index, n (also a

unique function of λ). We can make the slope of the basis functions continuous at θ_0 by an appropriate choice of eigenvalues, n .

The eigenvalues, n , are determined by numerical iteration such that

$$\frac{1}{P_n^{(m)}(\cos\theta)} \frac{dP_n^{(m)}(\cos\theta)}{d\theta} = \frac{1}{\cot^m(\theta/2) + \tan^m(\theta_0/2)} \frac{d}{d\theta} [\cot^m(\theta/2) + \tan^m(\theta_0/2)] \quad 3.27$$

where P_n^m and $dP_n^m/d\theta$ are calculated by series summation as in Haines (1985). An infinite number of eigenvalues, n , satisfy 3.27 for each value of m . Increasing values of n for a given m correspond to increasing latitudinal wavenumbers, and thus we retain only the smaller values in our series. For the present work it is adequate to truncate m at ± 10 and to take only the first $11-|m|$ values of n , giving a total of 121 basis functions. Figure 3.2 shows a sample of some of the lower order functions for $m=8$.

The functions f_m are fully normalized with a root-mean square value of one and satisfy

$$\frac{df_m}{d\phi} = m f_{-m} \quad 3.28$$

The basis functions, L_i , satisfy

$$\begin{aligned} r^2 \nabla^2 L_i &= \frac{1}{\sin\theta} \frac{\partial}{\partial\theta} \left(\sin\theta \frac{\partial L_i}{\partial\theta} \right) - \frac{m^2}{\sin^2\theta} L_i \\ &= -n(n+1)L_i & \theta < \theta_0, \quad \theta > \pi - \theta_0 \\ &= 0 & \theta_0 < \theta < \pi - \theta_0 \end{aligned} \quad 3.29$$

and are orthogonal over the interval $0 < \theta < \theta_0$:

$$\begin{aligned} \int_0^{\theta_0} d\theta \int_0^{2\pi} d\phi L_k L_i &= 2\pi(1 - \cos\theta) & k=i \\ &= 0 & k \neq i. \end{aligned} \quad 3.30$$

2. Model Parameter Covariance Matrix, C_s

We do not use detailed information from any particular data set to generate the A_{ij} values of equation 3.7. Rather, we rely on statistical information about the basic physical features we wish to estimate to aid in determining the A_{ij} elements. The statistical information is brought into the procedure via the model parameter covariance matrix, C_s . Richmond and Kamide (1988) pointed out that complete statistical information needed to construct C_s is not commonly available, but that it is possible to construct the matrix elements such that they conform to certain known physical features. For instance the auroral zone features tend to be more extended in the east-west direction (versus the north-south direction). Richmond and Kamide built this constraint into the C_s matrix by setting

$$C_s = S^* C_s^* \quad 3.31$$

where

$$C_s^* = (G_0)^{-1} \quad 3.32$$

where C_s^* is an unnormalized covariance matrix and G_0 is a diagonal matrix whose elements represent a spatial power spectrum accounting for the directional anisotropy mentioned above. At very large wave numbers the elements of G_0 vary as the fourth power of the wave number. We have added a further constraint:

$$C_s^* = (G_0 + \lambda_1 G_1)^{-1} \quad 3.33$$

The component, $\lambda_1 G_1$, forces the conductance variability, which is defined as

$$\langle \sigma^2 \rangle = \left\langle \left(\ln \left(\Sigma / \Sigma_0 \right) \right)^2 \right\rangle = \sum_{i=1}^I \sum_{k=1}^I \langle s_i s_k \rangle L_i L_k \quad 3.34$$

where $\langle s_i s_k \rangle$ is an element of C_s and the error truncation term $\left\langle \frac{-2}{r} \right\rangle$ has been neglected, to be roughly constant over the polar regions. We accomplish this by setting the elements of G_1 equal to weighted areal integrals of products of

basis functions L_1 poleward of 70° , and choosing λ_1 by trial and error to cause the variability $\langle \sigma^2 \rangle$ to be approximately uniform. Richmond and Kamide (1988) also normalized C_s to the strength of the variations observed at the time of interest. This normalizing factor can be obtained from the observations in the following way

$$C_z = \langle zz^T \rangle = \langle (Ls+v)(s^T L^T + v^T) \rangle \quad 3.35a$$

$$= L \langle ss^T \rangle L^T + \langle vv^T \rangle \quad 3.35b$$

$$= L \langle C_s \rangle L^T + C_v. \quad 3.35c$$

Therefore

$$C_v^{-1} \langle zz^T \rangle - I = C_v^{-1} L \langle C_s \rangle L^T \quad 3.36$$

Removing the angular brackets from $\langle zz^T \rangle$, replacing C_s by $S^* C_s^*$ and equating the traces of each side of 3.36 gives

$$S^{*2} = \frac{\text{Tr}(C_v^{-1} zz^T - I)}{\text{Tr}(C_v^{-1} L C_s^* L^T)} \quad 3.37$$

The normalized matrix C_s is that actually used in the estimation procedure. Figure 3.3 is a polar plot of the statistical variability of $\ln(\Sigma / \Sigma_0)$ for a particular time when this variability is approximately one everywhere.

3. Error Covariance Matrix, C_v

Our knowledge about the true form of the error covariance matrix is also rather limited. Although the matrix is dimensioned $J \times J$, we confine our error inputs to the diagonal terms. This is done primarily for simplicity but with some justification. First, measurement errors at different locations should be uncorrelated if they come from different instruments or if each instrument making multiple measurements has negligible systematic errors (e.g., calibration errors). Second, correlations among truncation errors that contribute to C_v will be small if the measurement locations are widely spaced

with respect to the largest spatial scales of the truncated basis functions and if the truncation errors are suppressed by spatially smoothing the estimated fields and correspondingly averaging the data.

The contributions to the diagonal terms of C_v are not well known either, but we can make some educated guesses about several of the factors responsible for the contributions. The contributions, which will be discussed below, come mostly from the measurements. We make the primary assumption that the different contributions to the diagonal terms are independently distributed with zero mean value. This allows us to calculate the elements $\langle v_j^2 \rangle$ as the sum of the expected square value of the individual contributions (Richmond and Kamide, 1988).

One obvious error source is the temporal mismatch between observations and the time-of-interest. The AMIE procedure accepts conductance observations that fall within plus or minus 20 minutes of the time of interest. Temporally distant observations are considered less valid in the estimation procedure. We require the errors associated with temporal mismatches to increase as a function of time squared.

In order to increase the spatial coverage of observations we use southern hemisphere conjugate measurements from the satellites and map them to the northern hemisphere. We do not expect the conjugacy to be valid in all cases, therefore the errors associated with these measurements are substantially larger than those for northern hemisphere.

Errors from instrumental biases and inadequacies are more difficult to quantify. Since this is one of the first studies to attempt assimilation of conductance data from so many different sources we rely to some degree on information from principle investigators to make error estimates. Based on

such information, it appears that errors from instrumental biases are likely to be small compared to the errors arising from converting the actual electron and/or X-ray spectra to conductance estimates. These errors will be discussed more thoroughly in Chapter 4. Our degree of confidence in the observations is reflected in the weightings we assign to them. The weighting for any given datum is the inverse square of its expected error.

IV. ERROR PROPAGATION

A Background

Richmond and Kamide's work (1988) is among the first to quantify the uncertainty associated with estimating the electric field via an inversion procedure such as AMIE. The follow-on work by Richmond et al. (1988) gave additional examples and discussions of the utility of the uncertainty estimation. In these previous AMIE reports the authors have assumed, for the purpose of estimating the electric field uncertainty, that the conductance patterns were highly certain and contained no error. In fact such perfect knowledge does not exist and an estimation of the uncertainty propagated from the conductance patterns into the electric field estimation needs to be made. Two conclusions from these studies (and many others before them) were that better estimates of the conductance distributions are needed and that the uncertainty in such estimates also need to be quantified. A major portion of the dissertation work has been aimed at meeting those needs. We added a variety of satellite conductance estimates to the assimilation procedure and made modifications in the AMIE procedure to calculate the uncertainty in the derived conductance patterns. We took the work one step further and attempted to show how the uncertainty in the conductance patterns affects the derived electric field and electric current patterns. This latter step requires further explanation.

Within the AMIE procedure a significant fraction of the information about the electric fields is derived from inversion of magnetometer data. The pertinent physical relation is

$$\mathbf{I} = \Sigma \mathbf{E} \quad 3.38$$

where \mathbf{I} is the ionospheric current vector, \mathbf{E} is the ionospheric electric current vector and Σ is the ionospheric conductance tensor. As has been shown by Kamide and Richmond (1982) the conductance link is critical for a proper estimate of the electric fields from magnetometer data.

Section III of this chapter shows how to calculate the uncertainty in the conductance estimates. In order to quantify the uncertainty propagated into the electric field estimate from the conductance estimate we must consider the interrelationship between the three quantities in equation 3.39. The probability density function for these quantities is given by

$$P_E(\mathbf{E}) = \int P_I(\mathbf{I}) P_\Sigma(\mathbf{E} / \mathbf{I}) d\mathbf{I} \quad 3.39$$

where P_E , the probability density function (pdf) for the electric field, is the integral product of the probability density functions for the current, P_I , and the conductance, P_Σ . It appears that determining the probability density function for the electric field (and hence some measure of the uncertainty) should be straightforward. But, the problem is complicated by the fact that none of the pdf's are well known and that the conductance pdf is related in a non-linear way to the other pdf's. Thus, tracing the error propagation from the conductances to the electric field becomes a nonlinear problem which we want to avoid. If we expect the variability of the electric field and conductances to be small (<10%) then perturbation theory could lead us to reasonable estimates of the conductance error propagation into the electric fields (D. Jackson private

communications, 1989). Unfortunately, experience indicates that the variability is closer to 40-50% for both distributions in most cases.

Another option for accomplishing the task would be to use a Monte Carlo approach. Such an approach involves first generating a reasonable pdf for the conductance based on available data. Secondly, a random number generator would be used to select random conductance values from the pdf which would in turn be used to calculate the electric field from the conductance value and the observations (ground magnetometer data). This process would need to be repeated several hundred times with randomly varying conductance values for each grid cell (having a spatial coherence consistent with the information in C_s) in order to build up a reliable picture of the uncertainty in the derived electric field distribution. This approach is technically feasible but the computer time required would be substantial. Such an approach is on hold pending further study.

Our chosen approach to the error propagation problem is a rather simple enveloping procedure. The process is to run the AMIE program for any time or series of times of interest, and in doing so, determine the conductance and electric field distributions and the associated uncertainties. On subsequent runs for the same time, or times of interest, the absolute value of the conductance uncertainty is added or subtracted from the conductance distribution everywhere. This creates an envelope of:

$$\ln\left(\frac{\Sigma}{\Sigma_0}\right) \pm \text{uncertainty} \quad \text{in} \quad \ln\left(\frac{\Sigma}{\Sigma_0}\right)$$

which gives rise to the three corresponding estimates of the electric fields. The envelope around the baseline value of the electric field is the simple estimate

of the uncertainty introduced into the derived fields by uncertainty in the conductance.

This approach has the disadvantage of being a "worst case" approach to the problem. It is unlikely that the entire conductance distribution would be instantaneously skewed in such a manner that the uncertainty was completely positive or negative. This disadvantage is significant but the approach does allow us to make some quantitative statements about the impact of conductance uncertainty in the inversion procedure.

B. Example

Figure 3.4 illustrates the variations in the estimated electric potential patterns associated with the plus or minus conductance uncertainty envelope. The pattern in Fig. 3.4a is derived by adding the conductance uncertainty to the baseline estimate of the conductance. The resulting "increase" in conductance reduces the electric field everywhere and decreases the cross polar cap potential difference from 81.7 kV to 58.9 kV. Reducing the conductance by a corresponding amount increases the cross polar cap potential to 108.8 kV. The general of the distribution is changed little except for a slight rotation of the potential pattern.

The simple test of the influence of conductance uncertainty suggests that conductance errors may propagate a ± 25 -30% error into the electric field estimates. Errors in conductance affect not only the magnitude of the electric potential but its distribution as well. The slight rotation in the potential patterns seen in figures 3.4a-3.4c are consistent with the findings of Yasuhara and Akasofu (1977). They attribute the change in potential distribution to the effect of large conductivity gradients between the discrete and diffuse auroral zones. When the conductance near the boundary is reduced space charge build-up

cannot be effectively reduced by currents. Polarization electric fields induced by the charge build-up are superimposed on the pre-existing electric field resulting in a rotation of the potential pattern.

Figure 3.5 shows plus and minus envelope estimates of several parameters for the two day period: 23-24 July 1983. The electric potential is strongly influenced by the uncertainty in the conductance while the total equivalent current and integrated field-aligned current are much less so. These findings are in accord with those of Kamide and Richmond (1982). The total Joule heating estimates, which combine information from the electric field and conductance estimates are also strongly influenced by the uncertainty propagation.

Interpreting the electric field estimates from AMIE requires us to be mindful of the error propagated from the conductance estimation. More effort is needed to integrate the errors into the overall estimates of the electric field.

V. SUMMARY

In this chapter we reviewed certain calculations necessary for estimating basic electrodynamic patterns from observations and prior data. We have also explained how the uncertainty in the derived fields can be determined from this same set of information. Finally, we have explained a simple procedure for estimating how the uncertainty in the conductance distributions impacts the derivation of the electric field estimates. The following chapters discuss new data sources for the conductance and electric field estimates and show their impact on the derived electrodynamic distributions.

FIGURE CAPTIONS FOR CHAPTER 3

Figure 3.1. Schematic diagram of the mapping procedure described by Richmond and Kamide (1988). Several types of information can potentially be used to estimate the distribution of electric fields, currents, and conductances. The conductance distribution (Σ_p, Σ_h) is estimated first, and is then used to link electric currents and electric fields in the next step of the fitting process. The basis functions for the electric potential Φ are pre-specified, while those for the electric field E , height-integrated ionospheric current I , field-aligned current $J_{||}$, and magnetic perturbations ΔB are calculated directly from those for Φ using the appropriate physical interrelationships. A single set of coefficients a_i is fitted to all of the available electromagnetic data simultaneously in order to obtain the final fields.

Figure 3.2. A sample of the basis functions L_i . The first four functions for the longitudinal harmonic $m=8$ are plotted against colatitude θ . Each function is labeled with the value of n determined for the appropriate generalized Legendre function.

Figure 3.3. Statistical Variability of $\ln(\Sigma/\Sigma_0)$ where Σ_0 is the model value appropriate to each grid cell. The contour interval is 0.05. The variability is given by the square root of equation 3.34:

$$\sqrt{\langle \sigma^2 \rangle} = \left\langle \left(\ln(\Sigma / \Sigma_0) \right)^2 \right\rangle = \sum_{i=1}^I \sum_{k=1}^I \langle s_i s_k \rangle L_i L_k$$

Figure 3.4 Illustration of the effect of conductance uncertainty on the estimated electric potential pattern for 2000 UT on 19 September 1984. The bottom panel gives a polar plot of the baseline electric potential estimate using the standard conductance estimate. The top diagram shows the estimated pattern resulting from the use of conductance plus the estimated uncertainty in the conductance. Increasing the conductance while holding all other input fixed decreases the electric potential. The middle panel shows the effect of reducing the conductance by the same amount.

Figure 3.5 Envelopes of potential difference, equivalent current and integrated Joule heating for 19 September 1984 associated with plus/minus conductance uncertainty. The electric potential and Joule heating show significant sensitivity to the conductance pattern used in the estimation. The upper curves in figures 3.5a and 3.5c correspond to [conductance minus uncertainty in conductance] while the lower curves correspond to [conductance plus uncertainty in conductance]. The larger differences in the curves are associated with more geomagnetically active periods of the day.

ASSIMILATIVE MAPPING OF IONOSPHERIC ELECTRODYNAMICS (AMIE)

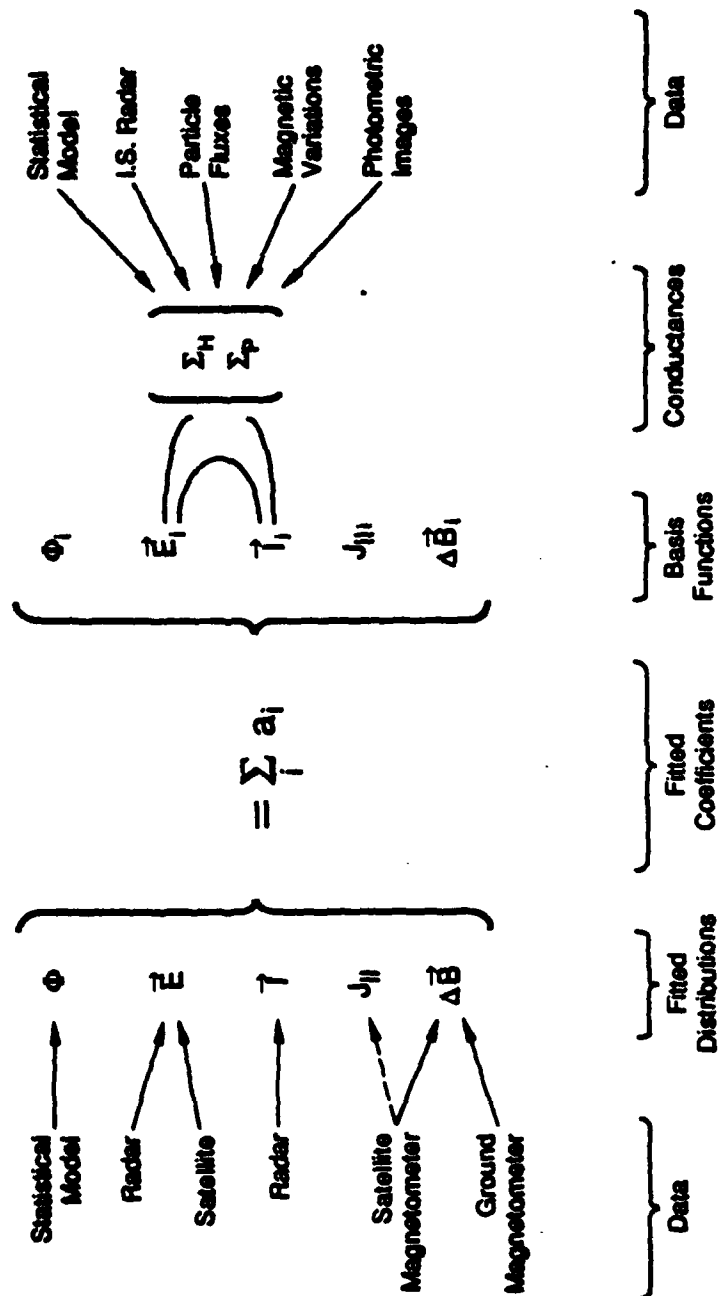


Figure 3.1

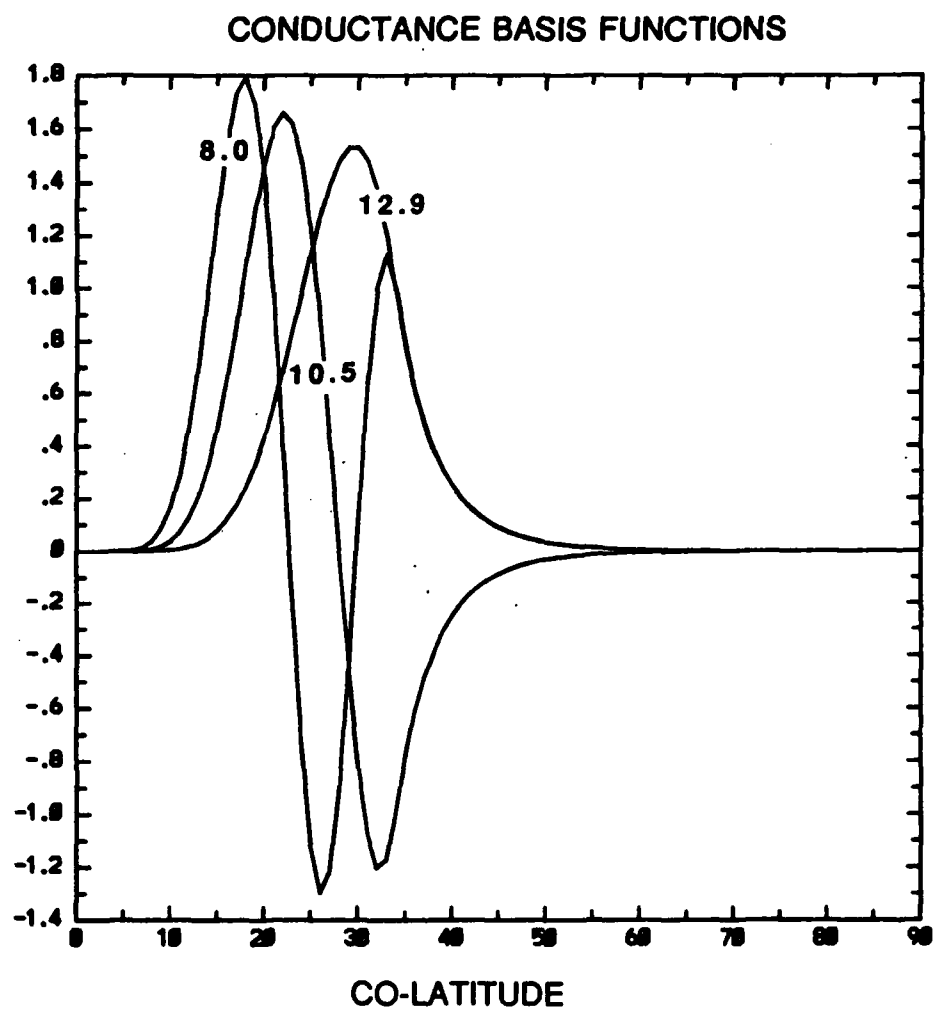


Figure 3.2

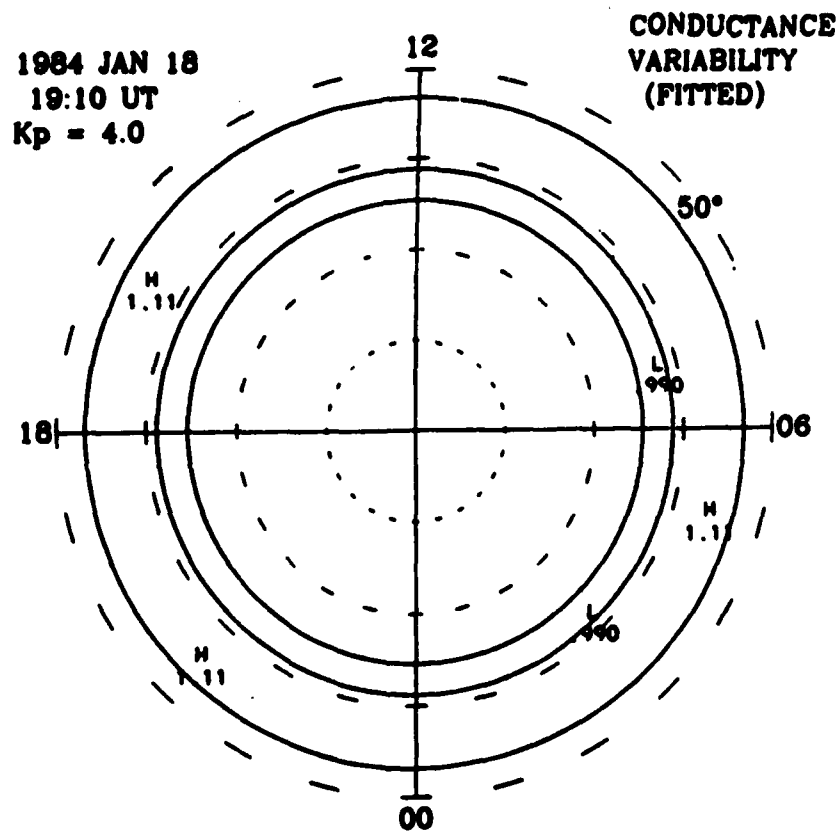


Figure 3.3

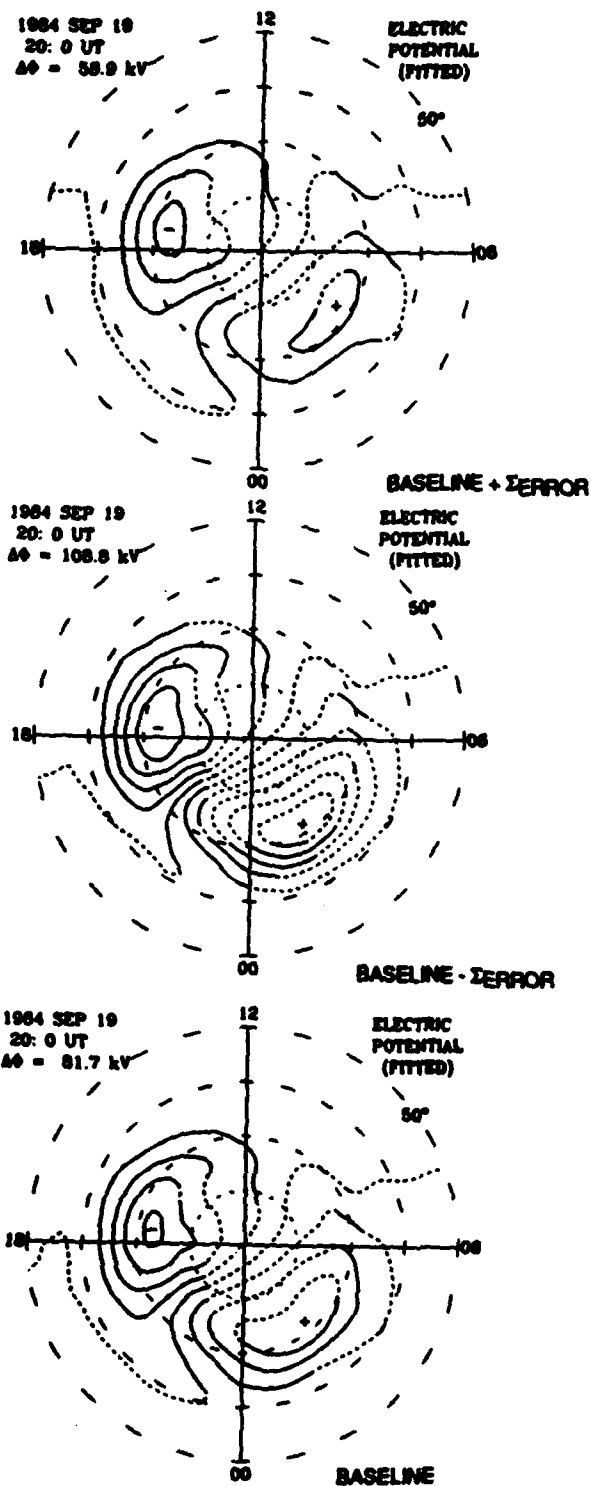


Figure 3.4

CONDUCTANCE ERROR PROPAGATION ENVELOPES,
19 SEPTEMBER 1984

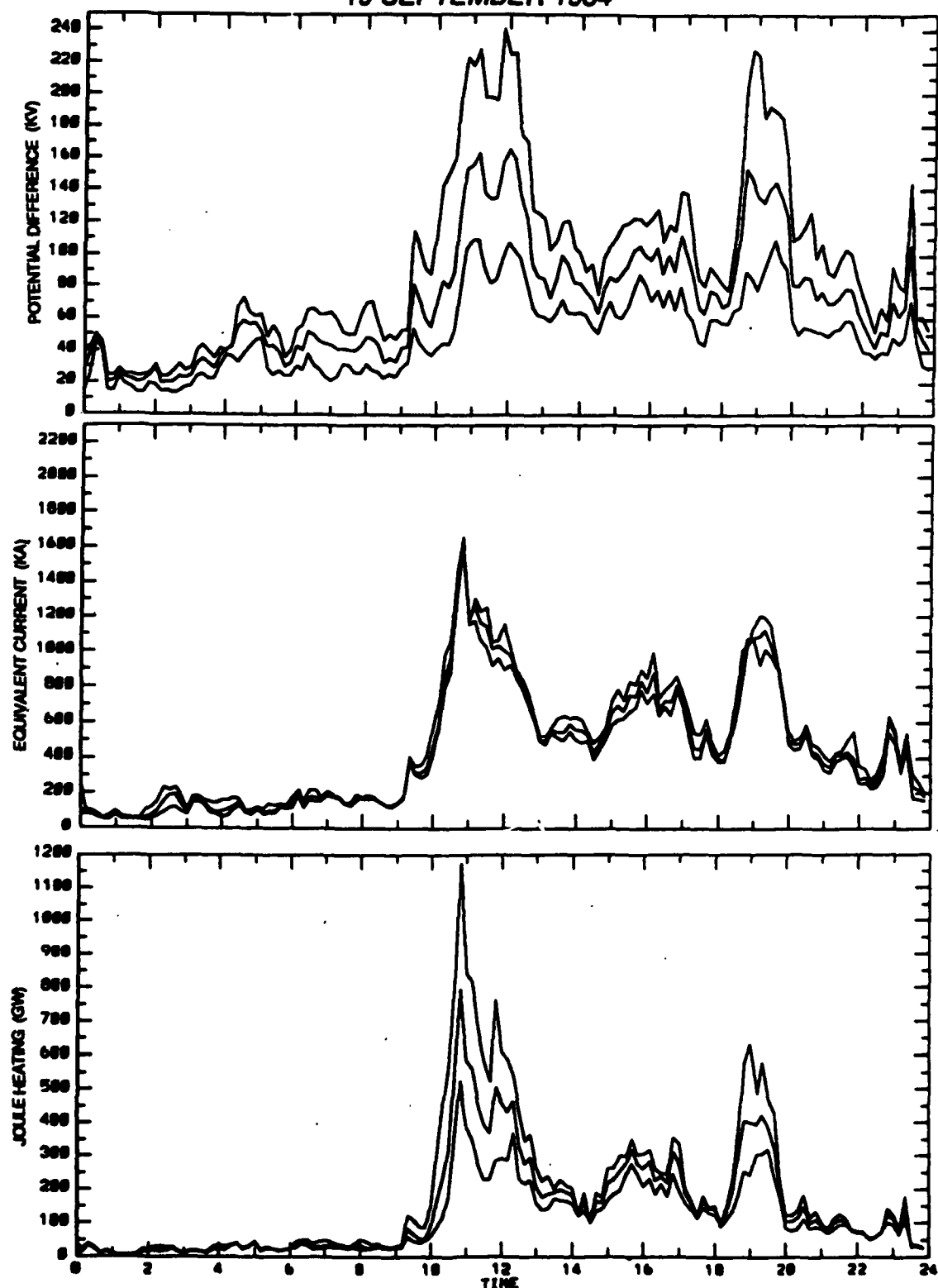


Figure 3.5

CHAPTER 4

IONOSPHERIC CONDUCTANCE

SOURCES, MEASUREMENTS AND UNCERTAINTIES

I. INTRODUCTION

This chapter deals with the general physical processes that produce ionization and the attendant enhancements of ionospheric conductance. Section II of this chapter covers the sources of ionization and X-ray emission and their relations to ionospheric conductance. Section III provides a discussion of the conductance estimates. The data behind these estimates, their derivations and the sources of uncertainty in the measurements are reviewed in section IV.

II. IONIZATION, X-RAY SOURCES AND CONDUCTANCES

A. Solar photoionization

Photoionization by solar ultraviolet and X-radiation is responsible for the general structure of the dayside ionosphere. In the early 1930's Chapman worked out the broad physical principles behind ionospheric layer formation. He showed that in the height range of 90-120 km (E-region) the combined effects of solar ionization and recombination of electrons and positive ions tends to produce electron density profiles with a characteristic square root dependence on the cosine of the solar zenith angle. Solar induced conductivity which is a function of electron density also exhibits the square root dependency (Robinson and Vondrak, 1984 and Brekke and Hall, 1988). Robinson and Vondrak (1984) showed that the electron density also depends on the level of solar activity which correlates well with the f10.7 cm solar flux. The location and relative values of solar induced conductance (for a winter time case) are shown in Fig. 4.1.

B. Particle Ionization

1. Morphology

The auroral ovals are basic elements of the high latitude phenomena. All sky photographs revealed annular regions of frequent auroral display (Akasofu, 1964) that are slightly offset towards the nightside (Feldstein, 1963). The "ovals" are usually less than 10° (≈ 500 km) in latitudinal extent but may expand to widths of 15° or more during substorms (Feldstein and Starkov, 1967). Geomagnetic disturbances can expand the combined polar cap-auroral zone region to 6000 km in diameter; during quiet times the total diameter is closer to 4000 km (Akasofu and Kamide, 1987). The poleward and equatorward edges of the auroral zone are located between 70 - 74° and 66 - 70° magnetic latitude, respectively, and are roughly defined by field-aligned currents.

Akasofu (1976) used DMSP imagery to examine features of the aurora in all local time sectors. He confirmed the presence of two types of aurora: diffuse and discrete. The diffuse aurora is a broad, continuous and relatively uniform belt of luminosity present in most local time sectors under all geomagnetic conditions. The particles producing the diffuse aurora are generally characterized by Maxwellian energy distributions (Liu et al., 1977). Stenbaek-Nielsen et al. (1973) showed the diffuse aurora to be conjugate and to have relatively smooth and continuous equatorward boundaries. Particles precipitating into this region are likely to originate in the central plasma sheet (Winningham et al., 1975).

In contrast the discrete aurora are highly structured with curtain and arc-like structures extending hundreds of kilometers in longitude and a few tens of kilometers in latitude. These aurora, which tend to appear in the morning hemisphere and on the high-latitude edge of the ovals, exhibit varying degrees

of conjugacy. The energetic particles responsible for the discrete aurora come from a variety of distributions but characteristically exhibit an accelerated component in addition to a Maxwellian component (Liu et al., 1977). Winningham et al. (1975) identified the boundary plasma sheet as the source of this structured precipitation.

Particles from the magnetosheath play a large role in forming the dayside auroral zone (Heikkila et al., 1972). The entry of magnetosheath plasma to ionospheric levels provides an essentially permanent dayside energy source for the ionospheric region between 120 and 300 km. The effects of the dayside cleft aurora are normally centered on local noon and 78° magnetic latitude (Shepherd, 1979).

2. Energetic particles

Unlike the relatively steady process of solar photoionization, energetic particle bombardment of the upper atmosphere exhibits a stormy variation in both time and space. By comparing results from studies such as Hardy et al. (1986) and Rees et al. (1988) it becomes evident that conductances may vary by as much as two orders of magnitude over the high-latitude regions. Rees et al. (1988) demonstrate order of magnitude variations within a matter of a few hundred kilometers in their DE-1 image analysis. Observations of discrete auroral features range from a few kilometers down to hundreds of meters (Maggs and Davis, 1968), suggesting that significant variations on these scales are also likely.

Whether the particles bombarding the upper atmosphere are primarily of solar origin or terrestrial origin remains in some dispute (Burch, 1977, and Chappell, 1988), however, their ultimate energy source is the sun. The solar surface continuously expels a supersonic flow of plasma, a tiny fraction of which

is intercepted by the earth and its magnetic field. The supersonic flow of plasma is shocked (slowed) by the earth's protective magnetosphere. Boundary interaction between the solar wind and the magnetosphere allow a small amount of the solar energy flux to "leak" into the magnetotail. Some studies suggest that .1 to .2% of the solar wind energy intercepted by the earth appears as auroral particle energy (Hargreaves, 1979).

The following discussion emphasizes the role of energetic electrons in auroral ionization production (versus production by protons and other positively charged particles). When total energy flux becomes significant (i.e. $> 1 \text{ erg cm}^{-2} \text{ s}^{-1}$) positive ions rarely contribute more than 20% of the total energy flux (Fuller-Rowell and Evans, 1987). The relatively low mass of electrons accounts for their greater mobility and allows them to play the dominant role in ionization and conductance.

There are two primary categories of particle energization: adiabatic and non-adiabatic energization. Examples of the latter include the neutral sheet acceleration in the vicinity of the magnetospheric neutral point (Speiser, 1967), heating via magnetic reconnection, (Sonnerup, 1970 and Hayashi and Sato, 1978) and acceleration in electric field structures parallel to the magnetic field (Swift, 1981, and Akasofu and Kamide, 1987).

Adiabatic energization is the most likely source of the steady auroral features often referred to as the diffuse aurora (Jones, 1974). The magnetospheric dawn-to-dusk electric field convects plasma sheet particles earthward from the nightside plasma sheet. The motion of these particles can be described by

$$\mathbf{v}_d = \frac{\mathbf{E} \times \mathbf{B}}{B^2} + \frac{\epsilon_{\perp} \mathbf{B} \times \nabla B}{qB^3} + \frac{2 \epsilon_{\parallel} \mathbf{B} \times \mathbf{R}}{qB^2 R^2} \quad 4.1a$$

$$= V_{\text{ELECTRIC}} + V_{\text{GRADIENT}} + V_{\text{CURVATURE}} \quad 4.1b$$

where V_d is the drift velocity of the particles,

E is the electric field seen by the particles as they move across the magnetic field lines,

B is the magnetic field induction,

q is the particle charge,

R is the vector radius of curvature of the field lines directed from the field line to the center of curvature,

e_{\perp} is the perpendicular energy associated with particle motion,

e_{\parallel} is the parallel energy associated with the particle motion.

The first term on the right hand side of equation 4.1a is the motion associated with the particles drifting on equipotential lines. Motions of low energy particles (<1 keV) are dominated by this term while the gradient and curvature terms strongly influence particles with energies of 1 keV or more (Jones, 1974). These latter terms represent conservation of the second adiabatic invariant and produce flow across equipotential lines thus imparting energy to the particles involved in such flows.

Energized electrons with small pitch angles have mirror points well down in the atmospheric regions where the probability of collisional loss becomes high. Particles with pitch angles of approximately less than 2° will "precipitate" into the atmosphere. But energization alone cannot account for the existence of the auroral zone. Precipitation of small pitch angle particles rapidly depopulates the atmospheric loss cone. Processes such as wave-particle interaction which scatters "new" particles into the loss cone (Burch, 1977) are also necessary to account for diffuse auroral zones.

C. Electron Energy Spectra

The characteristics of the electron energy spectra are important in determining the ultimate disposition of energy in the atmosphere. During the last thirty years numerous rocket flights and spacecraft measurements have investigated the nature of such distributions. A variety of energetic particle populations have been studied with the aid of particle spectral analysis (Mizera et al., 1981a and 1981b). The particle observations have been used in turn to infer the altitudinal extent of the acceleration regions and to predict the likely effects of particle-atmosphere interaction. Spacecraft measurements have shown the typical diffuse spectrum to be Maxwellian in shape with an average energy in the range of 1-4 keV (Liu et al., 1977) and an energy flux of of 1 erg/cm² s. The discrete aurora can also be typified with a Maxwellian distribution but quite often a Gaussian or mono-energetic spectra may be superimposed. Figure 4.2 (from Lui et al., 1977) shows typical spectra and indicates the spatial relationships between the plasma sheet and the two types of aurora.

Energetic particles (1-20 keV) are capable of ionizing atmospheric gases through a significant depth of the atmosphere. Electrons from the lower portion of the energy spectrum (0-5 keV) produce luminous aurora and contribute to ionization in the higher reaches of the ionosphere known as the F region (120-300 km) (Rees, 1963). The more energetic particles (5-10 keV) penetrate to the E region where the combination of energetic particles and greater atmospheric density produce significant contributions to ionospheric conductivity between 90 and 120 km. The most energetic particles ($E > 20$ keV) penetrate into the D region (60-90 km) where they produce significant fluxes of X-rays (Rees, 1963).

ionization occurs in this region but the number flux of particles into this altitude region is not sufficient to significantly affect ionospheric conductivity.

In a grossly simplified approach to ionization theory electrons travel through the atmospheric column producing new ion-electron pairs until their energy is spent. Each atmospheric ionization requires on the average 35 eV of energy. In reality, finite amounts of energy are lost by the primary electron in each inelastic collision and the efficiency of ionization processes depends on the energy of the incident electrons as well as their pitch angle. The "lost" energy appears in the kinetic energy of secondary electrons and the excitational energy of ions and molecules.

The quantitative description of ionization is a complicated process requiring knowledge of atmospheric pressure, density and composition, as well as ionization and excitation cross sections and the altitude profiles of energy deposition. Computationally imposing electron transport codes have been written to deal with the problem (Rees, 1963, Banks and Nagy, 1970, Rees and Jones, 1973, Strickland et al., 1976, Stamnes, 1985). Stamnes (1980) provided a summary of the development of electron transport theory. These codes are too cumbersome and time consuming to use as an adjunct to the AMIE code. Therefore, we rely on the work from a number of researchers that simplify the results from transport codes and match them to observations.

D. CONDUCTANCE

1. Recent Advances

Wallis and Budzinski (1981) were among the first to use satellite measurements to derive empirical models of height integrated conductivities. By using ionization rate profiles computed from the Rees (1963) method they were able to calculate the two-dimensional distributions of Pedersen and Hall

conductance from average particle distributions binned according to K_p . Their results showed that Maxwellian and mono-energetic spectra of the same average energy produce a factor of two difference in the calculated Pedersen conductance but the Pedersen to Hall conductance ratio is relatively insensitive to the type of spectral distribution below 20 keV.

Vickery et al. (1981) used electron density samples from Chatanika radar along with energy disposition code to estimate the temporal and spatial variation of conductance. They found that the quiet nighttime Pedersen and Hall conductances ranged from 2-6 S and 4-12 S respectively. Substorms increase these values to 25 S for the Pedersen conductance and 50 S for Hall conductance.

Robinson et al. (1987) confirmed that conductance produced by some of the more common auroral spectral distributions (exponential, mono-energetic and accelerated Maxwellian) are similar to those produced by a Maxwellian with the same average energy and energy flux. They also presented expressions that relate Hall and Pedersen conductances to the flux and average energy of a Maxwellian distribution. Figure 4.3 illustrates their results. As the average energy of energetic particles increases the particles penetrate deeper into the atmosphere, increasing the Hall conductance relative to the Pedersen conductance. The turn-over in the Pedersen curve (beyond 4 keV) accounts for this physical situation.

2. Calculations

One of the primary complicating factors in ionospheric physics is the anisotropy in ionospheric conductance. One, in general, thinks of currents as being parallel to the applied electric fields. This parallel, or Pedersen, component is present in the ionosphere. But the combined effects of electric

and magnetic fields generate a current perpendicular to both **E** and **B**. This perpendicular component is known as the Hall component. A third current and conductivity component is parallel to the magnetic field and is referred to as the direct or longitudinal component. The conductances can be most conveniently expressed in tensor form:

$$\underline{\sigma} = \begin{bmatrix} \sigma_p & \sigma_h & 0 \\ -\sigma_h & \sigma_p & 0 \\ 0 & 0 & \sigma_0 \end{bmatrix} \quad 4.2$$

where σ_p is the Pedersen conductance, σ_h is the Hall conductance and σ_0 is the longitudinal conductance. Typical height variations of the transverse components are shown in Fig. 4.4. As shown in Appendix III, force balance considerations lead to the following conductivity and height-integrated conductivity (conductance) formulas

$$\sigma_p = \left[\frac{n_e}{m_e v_e} \left(\frac{v_e^2}{v_e^2 + \Omega_e^2} \right) + \frac{n_i}{m_i v_i} \left(\frac{v_i^2}{v_i^2 + \Omega_i^2} \right) \right] |\Theta|^2 \quad 4.3$$

$$\sigma_h = \left[\frac{n_e}{m_e v_e} \left(\frac{\Omega_e v_e}{v_e^2 + \Omega_e^2} \right) - \frac{n_i}{m_i v_i} \left(\frac{\Omega_i v_i}{v_i^2 + \Omega_i^2} \right) \right] |\Theta|^2 \quad 4.4$$

$$\Sigma_p = \int \sigma_p dh \quad \text{and} \quad \Sigma_h = \int \sigma_h dh \quad 4.5$$

The conductance distributions used in the AMIE procedure consist of both solar and particle components. Robinson and Vondrak (1984) used incoherent scatter radar (ISR) observations of electron density to develop the following empirical relations between solar zenith angle θ , 10.7 cm solar flux (S_a) and Pedersen and Hall conductance produced by solar radiation:

$$\Sigma_p = .88 (S_a \cos X)^{1/2} \quad 4.6a$$

$$\Sigma_h = 1.5 (S_a \cos X)^{1/2} \quad 4.6b$$

where S_a varies between 60 (solar minimum) and 240 (solar maximum). The effect of this variation is to double the solar induced conductance between solar minimum and solar maximum.

Rasmussen and Schunk (1988) proposed the inclusion of a term proportional to the inverse of the magnetic field strength to properly account for magnetic field line convergence. The AMIE procedure was recently modified to include the f10.7 cm flux and the magnetic field strength terms (Richmond, 1989, and Emery, 1989 private communications). In order to estimate the conductivity values from the sum of the solar and particle sources the values are summed by the square root of the sum of squares of each component (Wallis and Budzinski, 1981)

$$\sigma_T^2 = \sigma_s^2 + \sigma_A^2 \quad 4.7$$

where σ_T is the total conductivity, from solar σ_s and auroral σ_A sources. We have assumed that the vertical profiles of ionization production from the two sources are similar.

E. Bremsstrahlung Processes

Ionization and dissociation are the primary and secondary energy sinks for precipitating particles. Bremsstrahlung X-ray production is a third energy loss mechanism (Rees, 1963). When an electrically charged particle is accelerated or decelerated it radiates electromagnetic energy. Bremsstrahlung (or braking radiation) is emitted when low mass particles such as electrons pass in the vicinity of a strong electric field from an atomic nucleus. Bremsstrahlung production is more significant for lighter incident particles with higher energies (Krane, 1983). In a bremsstrahlung interaction the momentum of collision is transferred to the more massive particle but the recoil kinetic energy of the atom

is small because the atom is so massive. The change in electron energy is given up as radiant photon energy.

The amount of energy lost in bremsstrahlung interactions can have a wide range of values, up to the total kinetic energy of the electron. Electrons will usually suffer a series of these collisions emitting a continuous distribution of X-rays as they pass through the atmosphere. The conversion of electron kinetic energy to bremsstrahlung is a relatively inefficient process. Only about 1×10^{-3} of the electron energy is so converted, although the conversion rate is somewhat energy dependent (Jones, 1974 and D. Gorney, private communication, 1989). While bremsstrahlung interactions are not responsible for ionization, the flux of bremsstrahlung X-rays is relatable to the electron energy spectra making bremsstrahlung X-rays a good remote sensing diagnostic.

Gorney et al. (1986) applied this diagnostic by recognizing that the bremsstrahlung production function depends on the incident electron energy and the exiting photon energy. They use observations of the X-ray flux emitted from regions of bremsstrahlung interaction to estimate the energy spectra of the incident electrons.

III. INSTRUMENTS AND ERRORS

A. Instruments

The conductance estimates used in the AMIE procedure are derived from measurements made by four classes of instruments: incoherent scatter radars (ISR), satellite energetic particle detectors, X-ray photometric imagers, and ground magnetometers. The following section describes how the conductance estimates are derived from each type of instrument and also gives a brief discussion of *a priori* conductance patterns.

There are several sources of error in the conductance estimates. Errors may arise from biases in the instruments themselves or in the methods by which energy or number counts are integrated. Simplifications and assumptions necessary to produce conductance estimates from either a sampled electron or X-ray spectra or magnetometer data may lead to large variations in the estimates. In situations where rapid geomagnetic variations are occurring measurements made as little as ten minutes either side of a specified time may not be very good indicators of the conductance values at the specified times. The following discussion provides more specifics on possible errors associated with each type of instrument.

1. Incoherent Scatter Radar

Electron density measurements made by the Sondrestrom radar in Greenland and the European Incoherent Scatter (EISCAT) radar in northern Europe have been used to determine height-integrated Hall and Pedersen conductances. Electrons in random thermal motion will incoherently scatter electromagnetic radiation impinging upon them. The radiation is scattered in all directions so that some will be backscattered toward the source. The backscattered power from a volume of space, $V(h)$, at height, h , is equal to

$$P_{bs} = P_{inc} \sigma N(h)V(h)/r^2 \quad 4.8$$

where P_{bs} is the backscattered power, P_{inc} is the incident power, r is the range, σ is the effective electron scattering cross section and N is the electron density. The effective scattering cross section depends on the relative ion and electron temperatures in the sampled region. Buneman (1962) showed that

$$\sigma \approx \frac{\sigma_e}{(1 + \alpha^2) \left(1 + \frac{T_e}{T_i} + \alpha^2\right)} \quad \alpha \leq 1.0, \quad \frac{T_e}{T_i} \leq 3.0 \quad 4.9$$

where T_e is the electron temperature, T_i is the ion temperature and a describes the ratio between the electron Debye length and radar wavelength (Evans, 1974).

By measuring the returned power it is possible to determine the electron density in a volume of the ionosphere assuming a reasonable estimate of electron/ion temperature ratio can be made. The electron density measurements are combined with information from neutral atmosphere models on collision frequency, ν , and gyrofrequency, Ω , to give estimates of the Pedersen and Hall conductivity as indicated in equations 4.3 and 4.4.

Incoherent scatter radars have a long history of providing conductance estimates. Possible error sources are documented in a number of publications (Folkstead et al., 1983, Evans et al., 1979, Foster et al., 1986, Kelly, 1983 and Wickwar et al., 1984). The most significant ISR limitations are (1) loss of signal at very low electron densities (de la Beaujardiere, 1989), (2) insufficient radar calibration and (3) inadequate temperature correction in the cross section estimation.

A further problem associated with ISR conductance estimation, but not due to the radars themselves, is an inexact knowledge of the ion-neutral collision frequency used in the conductance formulas. Brekke and Hall (1988) have addressed this problem. Their results indicate that the choice of ion-neutral collision frequency may cause a two-fold variation in the estimated solar component of the Pedersen conductances.

2. Satellite energetic particle detectors

Satellite energetic particle detectors have provided the preponderance of conductance information for this study. These instruments sense the flux and energy of particles downwelling into the ionosphere from various regions of the

magnetosphere. Satellite-borne particle detectors have the advantage of quickly sensing large stretches of the near-Earth environment, but their frequency of coverage is limited (orbital period is approximately 100 minutes). Their relative speed (approximately 8 km s^{-1}) may also degrade the spatial resolution of such measurements. Further, they only sense energetic particles along the satellite track. The disadvantages can be at least partially mitigated by making use of simultaneous measurements from several satellites and by using conjugate measurements. This study has made use of such observations from NOAA-6, NOAA-7, NOAA-8 and DMSP F7 satellites.

a. NOAA Satellites

The NOAA series satellites carry instrumentation for measuring directional energy flux of electrons and positive ions impinging on the atmosphere. The energy sweep for the instruments is divided into eleven logarithmically spaced energy bands between 300 eV and 20,000 eV. After accumulating counts in each of the eleven bands the band containing the maximum number of counts is identified and the band number and associated count are telemetered to earth. This energy band defines a "characteristic" energy. Fuller-Rowell and Evans (1987) have done extensive simulations on the ionization profiles and conductance produced by downwelling energetic particles. They provide a "look-up" table (graph) for converting telemetered energy and flux information to height-integrated conductances. The graphed values from this look up table are shown in Fig. 4.5. Fuller-Rowell and Evans estimate 30% error in the estimates in the height range 100-120 km. We average the data into 2° latitude intervals and use computerized "look up" tables to produce input conductance estimates for the AMIE program.

The observations taken by these instruments are usually fitted to single Maxwellian electron spectral distribution. During stormy times when a variety of mechanisms may lead to localized acceleration of particles, such fits may be inappropriate to the real situations. Another possible error contribution arises from ignoring the positive ion contribution and the contribution from electrons whose energies fall outside the range of the detectors. Fuller-Rowell and Evans (1987) and Brekke and Hall (1988) argued that ions contribute less than 20% of the energy input to the conductance formation and can be safely ignored. Rich et al. (1987) asserted that significantly accelerated (>20 keV) distributions represent a small fraction of the total observations of precipitating particles.

b. DMSP F/7 Satellite

The Air Force Geophysics Laboratory provides similar energetic particle flux data for the DMSP F/7 satellite. This satellite follows a sun-synchronous, 101 minute orbit near the 10:30-22:30 local time meridian. Ion and electron energy spectra are measured each second and binned into twenty logarithmically spaced channels between 30 eV and 30,000 eV. Rich et al. (1987) assumed that the flux of electrons is isotropic and Maxwellian. They used the portion of the electron spectrum between 460 eV and 30 keV to calculate several parameters needed in the conductance estimates:

Total flux of electrons, JTOT [electrons/cm² s sr]

Energy flux of the electrons, JETOT [keV/cm² s sr]

Average energy, EAVG=JETOT/JTOT [keV]

The energy flux is given by an integration of energy flux over the downwelling hemisphere

$$\Phi_E [\text{erg} / \text{cm}^2 / \text{s}] = \pi \cdot 1.602 \times 10^{-9} [\text{erg} / \text{keV}] \text{JETOT} \quad 4.10$$

These calculated values are used in the semi-empirical relations provided by Robinson et al, (1987) for estimating conductance:

$$\Sigma_p [\text{mho}] = 40 E_{\text{AVG}} \Phi_E^{1/2} / (16 + E_{\text{AVG}}^2) \quad 4.11$$

and

$$\Sigma_H [\text{mho}] = .45 (E_{\text{AVG}})^{.85} \Sigma_p \quad 4.12$$

where the average energy in keV is computed from measurements of fluxes of precipitating electrons according to

$$E_{\text{AVG}} = \left(\int_{E_{\text{MIN}}}^{E_{\text{MAX}}} E R(E) dE \right) / \left(\int_{E_{\text{MIN}}}^{E_{\text{MAX}}} R(E) dE \right) \quad 4.13$$

A graph of the Robinson et al. (1987) formulation is shown in Fig. 4.3. Their relations are based on analyses of a variety of energy spectra measurements made by the HILAT satellite.

Before assimilating these data into the AMIE procedure we average the DMSP estimates of conductance and energy values over 40 s periods to eliminate some apparent instrumental biases and to provide a minimum 2 1/2° data spacing that AMIE can accept without introducing correlated truncation errors into the procedure. Errors associated with these conductance estimates are similar to those for the NOAA satellites.

3. DMSP F/6 X-ray Measurements

The DMSP F/6 spacecraft carries a raster scanning X-ray spectrometer which acquires a complete X-ray spectrum (2-70 keV in 24 channels) once per second while scanning limb to limb across its ground track every 20 s. Gorney et al. (1986) used a maximum entropy formalism to determine electron spectral shapes which most closely reproduce the observed X-ray spectrum. This formalism yields an optimal estimator of the incident electron spectra from

discrete values of the observed X-ray spectrum. The deconvolution provides the smoothest (most cautious) estimate of the distribution function among a set of distribution functions which meet the constraints imposed upon the spectrum estimation procedure.

In order to arrive at this estimator it is necessary to determine an appropriate bremsstrahlung production function Φ which approximately satisfies the following expression for the observed X-ray spectrum:

$$f_x(X, \eta) = \int_x^{T_{\max}} dT f_e(E) \phi(X, E, \eta) + e(X) \quad 4.14$$

In this equation f_x is the observed X-ray flux which is a function of photon energy, X , and aspect angle, η . The X-ray flux is equal to the integral product of the electron flux, f_e , and the bremsstrahlung production function, ϕ , which is itself a function of incident electron energy, E , and aspect angle. The term $e(X)$ accounts for variations which arise from processes not described by the production function. It is assumed to have an expected value of zero (Gorney et al., 1986). The electron spectra may be deconvolved from equation 4.14 by assuming a form of the bremsstrahlung production function.

A knowledge or estimate of how the electron energy is degraded with each interaction and of what fraction of the produced X-rays are absorbed by the atmosphere before they can be detected by a sensor located outside the absorbing regions is required to obtain the form of the bremsstrahlung production function. The mathematics of this latter function are complex (as shown by Gorney et al., 1986 and Luhmann, 1977) but a good feel for the physics can be obtained by considering that a beam of electrons of energy E_i interact with atoms in an atmospheric range of depths from 0 (at the top of the atmosphere) to z_c (the emission range of the electron). The interaction

produces X-rays throughout that depth. The measured bremsstrahlung intensity at the top of the atmosphere is a function of (1) the incident electron energy spectra degraded by the interaction producing the X-rays (2) the probability of interaction between the electron and the atmospheric target (cross section) and (3) an exponential attenuation factor to account for absorption of produced X-rays. Gorney et al. (1986) discussed the mathematics and the simplifications necessary to arrive at a reasonable approximation to the production function. They gave

$$\phi_{ij} = 4.86 \times 10^{-6} \frac{(E_i - K_j)E_i}{K_j^{1.5}} \quad 4.15$$

as their result. This approximation ignores aspect angle effects which can be significant for η greater than 70° . In this equation the K_j 's are the discrete levels of observed X-ray energy and the T_i 's are the electron energies. Figure 4.6 illustrates the relationship between bremsstrahlung production at a given energy and the incident electron energy. The curves show that increasing the incident electron energy not only increases the energy level at which X-rays are produced, but causes significant enhancement of the X-ray production at all lower energy levels. The turn over in the curves at low energy values is caused by absorption of X-rays produced deep in the atmosphere.

The deconvolved electron spectra can in turn be manipulated to produce basic flux information such as the integral energy flux, JETOT, the integral number flux, JTOT, and the average energy, EAVG (Gorney et al., 1986 and Gorney, private communications, 1989). These values can then be used in empirical formulas such as those from Spiro et al. (1982) or Robinson et al. (1987) to produce conductance "observations."

A polar cap X-ray scan takes about twenty minutes and can be acquired only once every 100 minutes (fifty minutes if conjugate measurements are used). Therefore, there are large gaps in the sets of conductance observations made by the scanner. Besides this obvious timing limitation there are instrumental limitations. As the X-ray instrument scans it may integrate signals from very large spatial regions especially when the scanner is looking at the limb of its scan (Rosenburg et al., 1987). Discrete and diffuse aurora are likely to be smeared together in these situations. Therefore the deconvolved electron spectra from such limb regions are likely to contain significant errors.

Examples of the deconvolution for three electron spectra are shown in Fig. 4.7. These plots show the input spectra, the X-ray spectra corresponding to the input and the deconvolved (inferred) spectra. The figures for the higher energy electron spectra illustrate the difficulty in inferring the details of the lower energy portion of the deconvolved electron spectra. This problem arises from the propensity of very energetic electrons to produce much higher fluxes of lower energy X-rays than do low energy electrons. As a consequence the low energy portion of the inferred electron spectra are very uncertain and are not used in estimating the conductance for the AMIE procedure. Additionally the X-ray instrument frequently "sees" a low signal to noise ratio. Results from Gorney et al. (1986) suggest that errors on the order of 50% are likely in the derived conductance "observations."

Although these shortcomings are troublesome, the X-ray measurements offer the advantage of quickly surveying large sections of the auroral oval. Except in the most dynamic cases one can gain a good sense of the near-instantaneous activity in the auroral oval and polar caps zone from an X-ray pass.

4. Magnetometer Data

Ahn et al. (1983) showed that ground magnetic perturbation measurements from the auroral latitudes can be used to estimate overhead conductances. They did extensive comparisons of the ground horizontal magnetic perturbations at College, Alaska with the ionospheric conductances determined from Chatanika radar located near 65° magnetic latitude. Ahn et al. arrived at the following least squares expression for the Hall and Pedersen conductance estimates:

$$\Sigma_p = 2.432 (\Delta H)^{0.255} \quad \text{and} \quad \Sigma_H = 4.355 (\Delta H)^{0.340} \quad \Delta H < 0 \quad 4.16$$

$$\Sigma_p = 0.699 (\Delta H)^{0.432} \quad \text{and} \quad \Sigma_H = 2.096 (\Delta H)^{0.357} \quad \Delta H > 0 \quad 4.17$$

where ΔH is the observed ground horizontal magnetic deviation.

These conductance estimates are incorporated in the AMIE estimation with the following modification: the Hall formula is divided by 2 to bring the Hall/Pedersen ratio into accord with that from the statistical patterns of Fuller-Rowell and Evans (see next section). The conductance estimates from the magnetometer data are quite indirect and the associated errors, v_j 's, in the logarithms of the conductance estimates are large. Richmond and Kamide (1988) suggested that errors on the order of a factor of two are likely at the latitude of Chatanika radar (65° magnetic latitude) based on the information provided by Ahn et al. The errors go to infinity as the conductance formulas go to zero. At latitudes away from 65° the empirical conductance formulas become less valid and the errors are increased accordingly. We use only the magnetometers at latitudes between 60° and 75° for the estimation.

5. *A priori* Patterns

The AMIE procedure uses *a priori* average conductance patterns in regions where data are sparse or where the data are believed to contain large errors.

Fuller-Rowell and Evans (1987) used eight years of particle flux measurements from the NOAA satellites to construct statistical global patterns of Pedersen and Hall conductance. These statistical patterns are organized with respect to a ten level auroral activity index developed by Foster et al. (1986). This index, hereafter referred to as the Hemispheric Power Index (HPI), is an estimate of the energy deposited into a single hemisphere by incident particles. The characteristic annular pattern of conductance corresponds to patterns of energetic particle influx. As previously mentioned the AMIE procedure adds a solar ultraviolet component to the dayside Fuller-Rowell and Evans model (see Fig. 4.1). The resulting statistical patterns are then averaged into rectangles of 2° magnetic latitude by 48 minutes of magnetic local time. Gaps are filled by interpolation (Richmond et al., 1988).

5. Examples

The panels in Fig. 4.8 show the variations in the number of conductance "observations" assimilated into the AMIE procedure. Figure 4.8a shows the observations from auroral magnetometers and from NOAA-6 and NOAA-7 satellites. Figure 4.8b shows the addition of DMSP F/7 particle measurements as well as observations from the DMSP F/6 X-ray imagery. Over 235 conductance observations were available at 1940 UT on 18 January 1984.

Figure 4.9 shows the evolution of the conductance patterns for 1940 UT on 18 January as new data are assimilated. The model pattern is shown in the top left position. The right column shows the evolution of the estimated pattern as new data sources are added. We illustrate the role of the observations in reducing the estimated error in Fig. 4.10. The observations reduce the estimated error by 50-70% compared to regions where data are unavailable.

As a final illustration of AMIE conductance estimation capabilities we present a time series of geophysical parameters (Fig. 4.11) and two sets of conductance and electric potential estimates from the 18-19 January 1984 (Figs 4.12 and 4.13) . Vertical lines on Fig. 4.11 correspond to 1810, 1950, 2130 UT on 18 January and 2320 UT on 18 January, 0100 and 0240 UT on 19 January. These times are chosen to demonstrate the types of auroral variations and disturbances that may be discerned with close to "full coverage" from the instruments we've discussed.

Figure 4.12 shows the enhancement and decay of the auroral oval during a moderate increase in magnetic activity late on 18 January. The oval transitions in character from patchy (top panel) to continuous and structured (middle panel) and back to patchy (bottom panel). The conductance enhancement at 1950 UT suggests some kind of energy transfer event between the magnetosphere and ionosphere, yet the electric potential at 1950 UT decreases relative to that at 1810 UT. This decrease is apparently accounted for by the increase in conductance since AE index for that time (see Fig. 4.11) does not show a decrease in magnetic activity. Figure 4.13 shows a more typical scenario with a significant enhancement of conductance associated with an increase in cross cap potential at 0100 UT in 19 January. All three conductance maps show peak conductance in the vicinity of the dawn meridian. The peak values are 9.48 S, 18.9 S, 9.43 S for 2320, 0100, and 0240 UT respectively.

B. ERROR LIMITATION

We require weightings of observations temporally distant from the time of interest to decrease as the inverse of time. Observations more than twenty minutes beyond the time of interest are not used.

An important question to ask is "How reliable and accurate are the results?" The method of determining the uncertainty was addressed in the previous chapter and examples are given in chapter 6. One of the important elements of the uncertainty calculation is the error covariance matrix, C_v , whose elements are composed of the expected square value of the individual error contributions (i.e., $(\text{temporal error})^2 + (\text{data error})^2 + (\text{truncation error})^2 + \dots$). The larger the error elements, the smaller the weighting given to the individual datum and the less constrained are the estimated patterns by that datum. Upon adding new data sources to the AMIE procedure we usually lack detailed knowledge of the data errors. In those cases we make adjustments to the weighting by modifying the data error term. Our modifications are semi-empirical in that we make an AMIE run with the new data included and compute the root-mean-square of the difference between the computed conductance and the observed values over the entire high-latitude region. On average we expect this difference to be comparable to the expected error in which case the ratio:

$$\text{rms} [(\text{computed difference})/(\text{expected value error values})] \quad 4.18$$

should be close to unity. If the ratio is significantly different from unity for the entire period of study (say 24 hours) then this signifies that an overall increase or decrease in the weighting of the data is necessary and we modify the data error accordingly. Increasing the weighting constrains the estimated patterns to fit the data, while decreasing the weighting allows the estimated patterns to approach statistical values.

FIGURE CAPTIONS FOR CHAPTER 4

Figure 4.1. AMIE Pedersen conductance model. The shaded portion shows the influence of solar ionization. Solar induced conductance ranges from approximately 3 to 9 S. Particle induced conductance for this level of activity (HPI=7) shows a similar average range on the nightside but are temporally and spatially more variable.

Figure 4.2. Schematic diagram illustrating the spatial relationship between the plasma sheet and the two types of aurora. Characteristics of electron differential energy spectra in both types of aurora for quiet and substorm times are also illustrated. These discrete aurora shows a high energy component associated with a variety of acceleration mechanisms (from Lui et al., 1977).

Figure 4.3. Graphical depiction of the Robinson et al. (1987) empirical formula's for Hall and Pedersen conductance. The ordinate is average electron energy. When average energies exceed approximately 4 keV electrons penetrate deeper into the atmosphere increasing Hall conductance relative to Pedersen conductance.

Figure 4.4. Altitude profiles for the electron density N_e , the Pedersen conductivity Σ_p , and the Hall conductivity Σ_h for a quiet evening time (0646 UT), a disturbed nighttime (1039 UT), a disturbed daytime (2311 UT), and a quiet daytime (0010 UT) on October 13-14, 1972. Local time is universal time minus 10 hours. (Brekke et al., 1974). The graph illustrates the point that more

energetic particles penetrate to greater depths increasing the amount of Hall conductance during disturbed periods.

Figure 4.5. Graph of the Fuller-Rowell and Evans (1987) look-up table for converting energy flux and "characteristic" energy to Hall and Pedersen conductance. The curves are fit to data acquired by the NOAA series satellite particle detectors. The ordinate is Fuller-Rowell and Evans "characteristic" energy which corresponds to the average energy if the distribution is Maxwellian.

Figure 4.6. Plot of the Bremsstrahlung production at energy E of unit incident electron flux and energy T for a geometric progression of energy channels. Higher energy electrons produce larger fluxes of X-rays at all energy levels than do lower energy electrons. The turn over of the curve at low energies corresponds to atmospheric absorption of X-ray energy. (From Gorney et al., 1986).

Figure 4.7. Example (from Gorney et al., 1986) of the deconvolution of electron spectra from 2 levels of idealized X-ray energy. The deconvolution produces better results for lower energy spectra. Higher energy spectra produce copious quantities of low energy X-rays that are not well modelled by the deconvolution.

Figure 4.8. Example of extremes in coverage of conductance estimates. (a) low coverage (b) more extensive coverage. The magnitude of the conductance estimate is proportional to the length of the arrow. The arrow direction is chosen to be arbitrarily westward.

Figure 4.9. (Top, left) Model conductance for 1940 UT, 18 January, 1984. Plots in the right column illustrate the evolution of the conductance estimate as data are added to the estimation and a more complete observational coverage is attained. Remaining plots in the left column show satellite conductance observations corresponding to patterns in the right column.

Figure 4.10. Conductance uncertainty given by the square root of equation 3.24 that is:

$$\sqrt{\sum_{i=1}^I \sum_{k=1}^I \langle (\hat{s}_i - s_i) (\hat{s}_k - s_k) \rangle L_i L_k}$$

Figure 4.11. Time series of geophysical variations for 18-19 January 1984.

Figure 4.12. Plots of Pedersen conductance and electric potential for 1810, 1950 and 2130 UT on 18 January, 1984.

Figure 4.13. Plots of Pedersen conductance and electric potential for 2320 UT on 18 January, 1984 and 0100 and 0240 UT on 18 January, 1984.

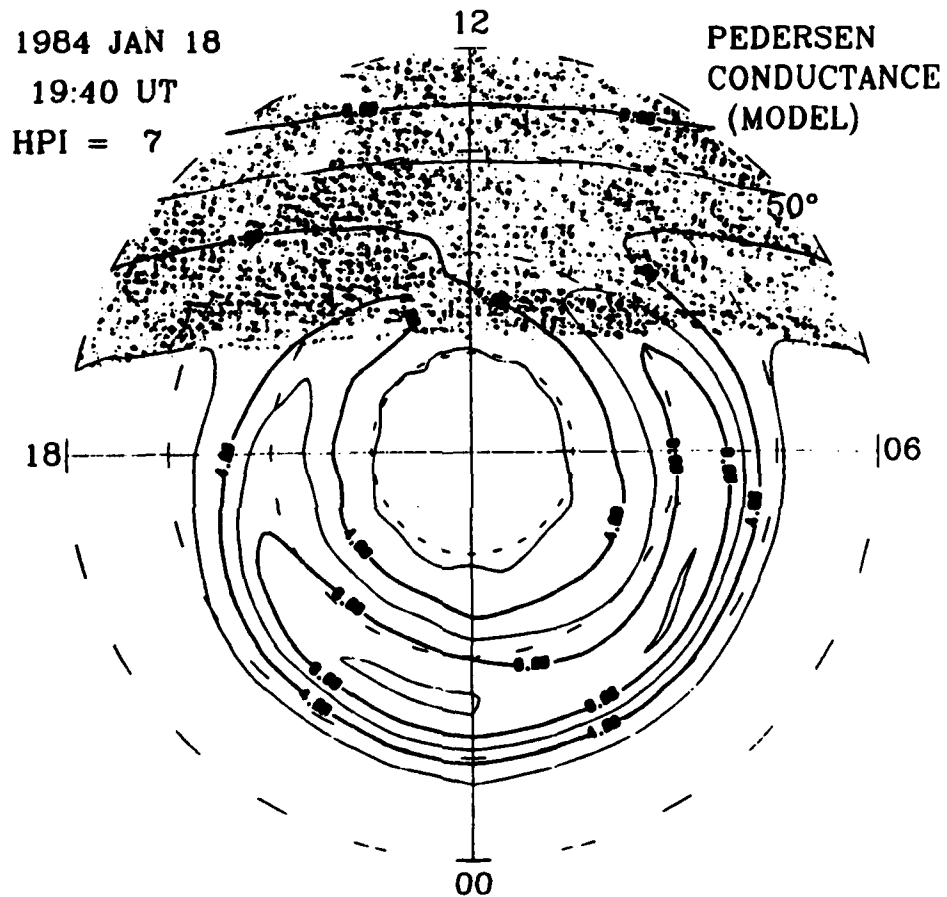


Figure 4.1

SPATIAL RELATIONSHIPS BETWEEN PLASMA SHEET AND AURORA

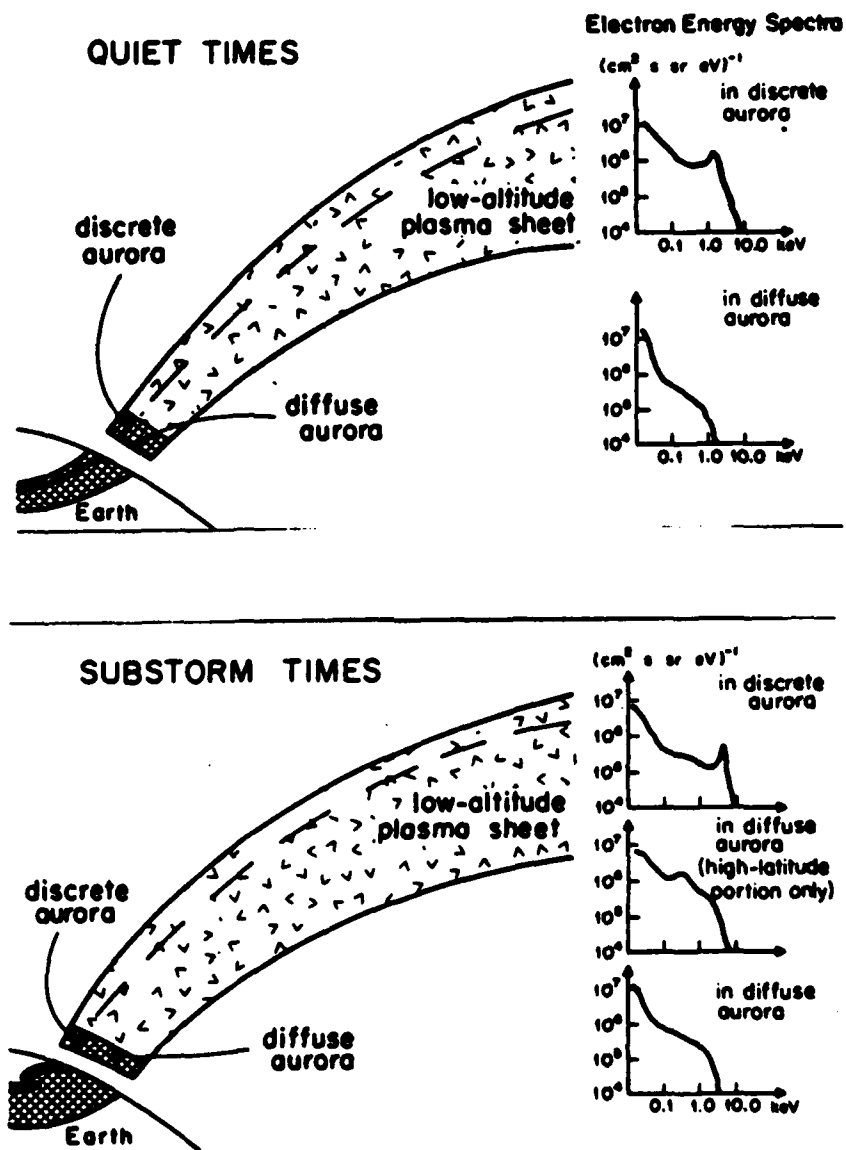


Figure 4.2

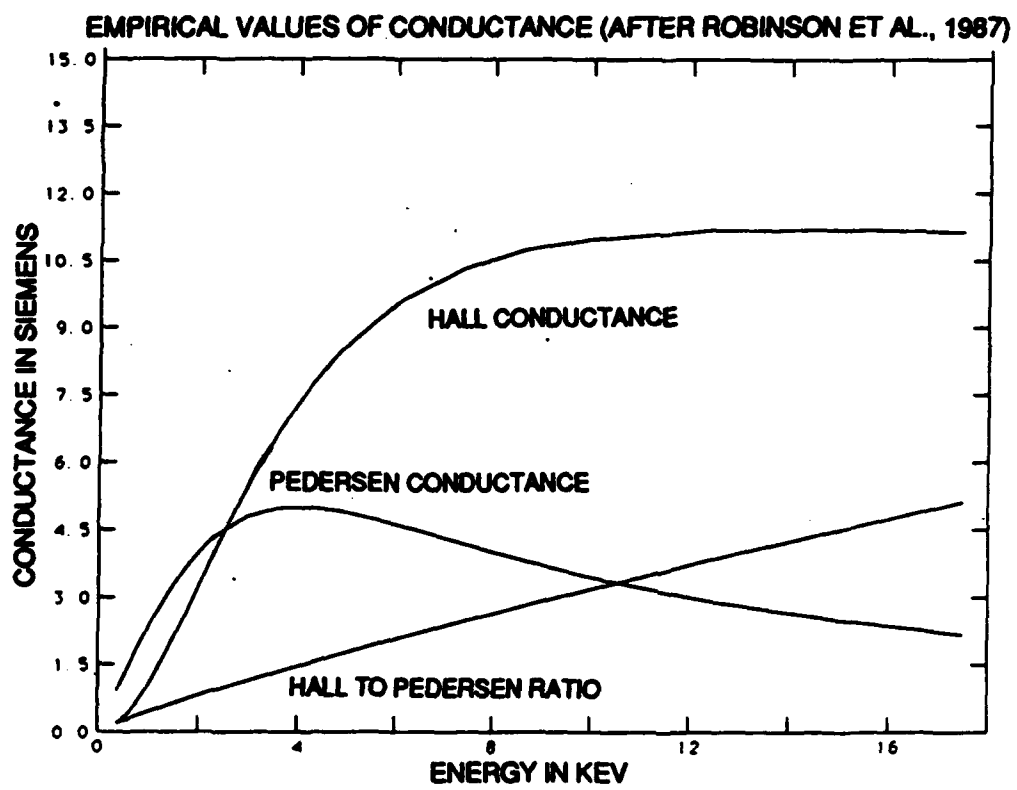


Figure 4.3

ALTITUDE PROFILES OF ELECTRON DENSITY, PEDERSEN AND HALL CONDUCTANCE

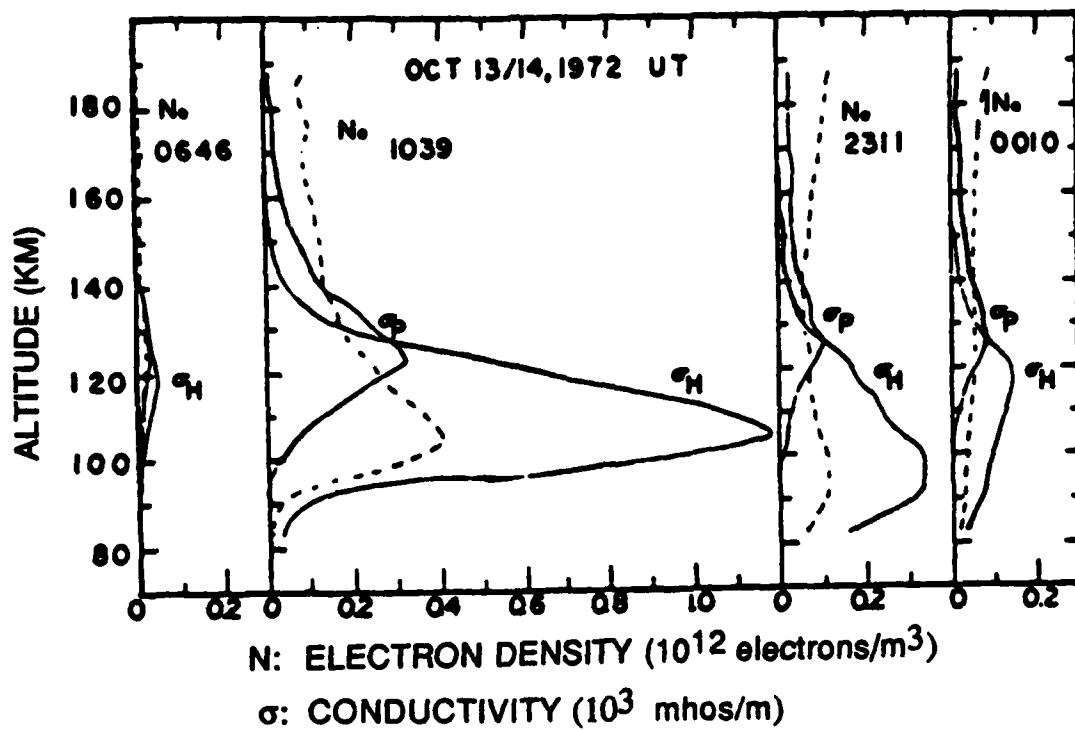


Figure 4.4

FULLER-ROWELL AND EVANS CONDUCTANCE LOOK-UP VALUES

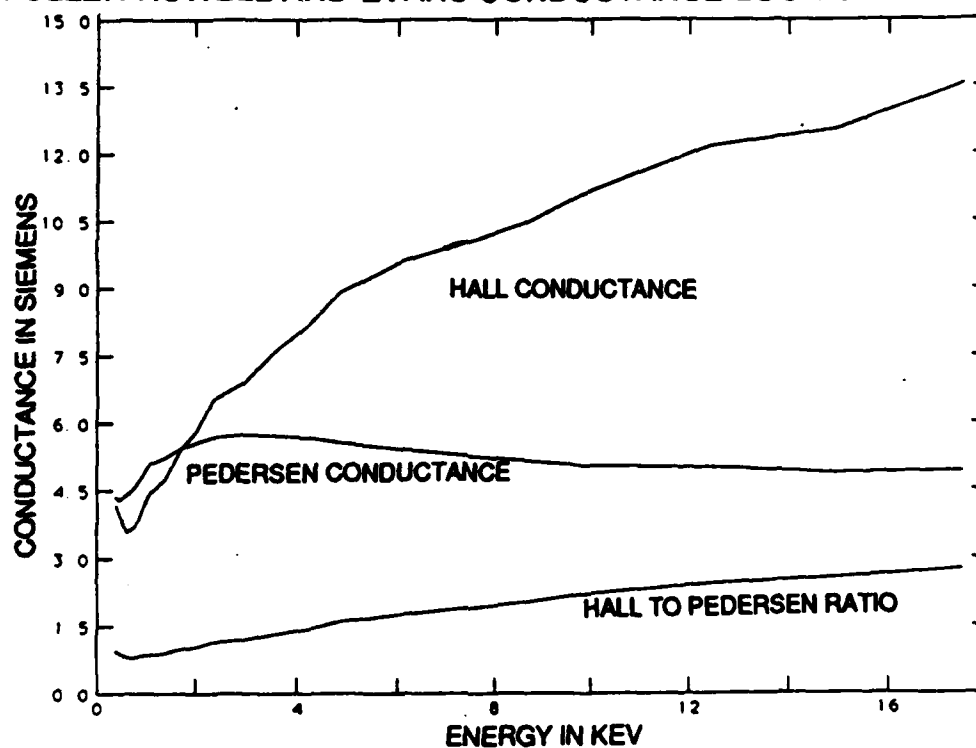


Figure 4.5

BREMSSTRAHLUNG PRODUCTION FUNCTIONS

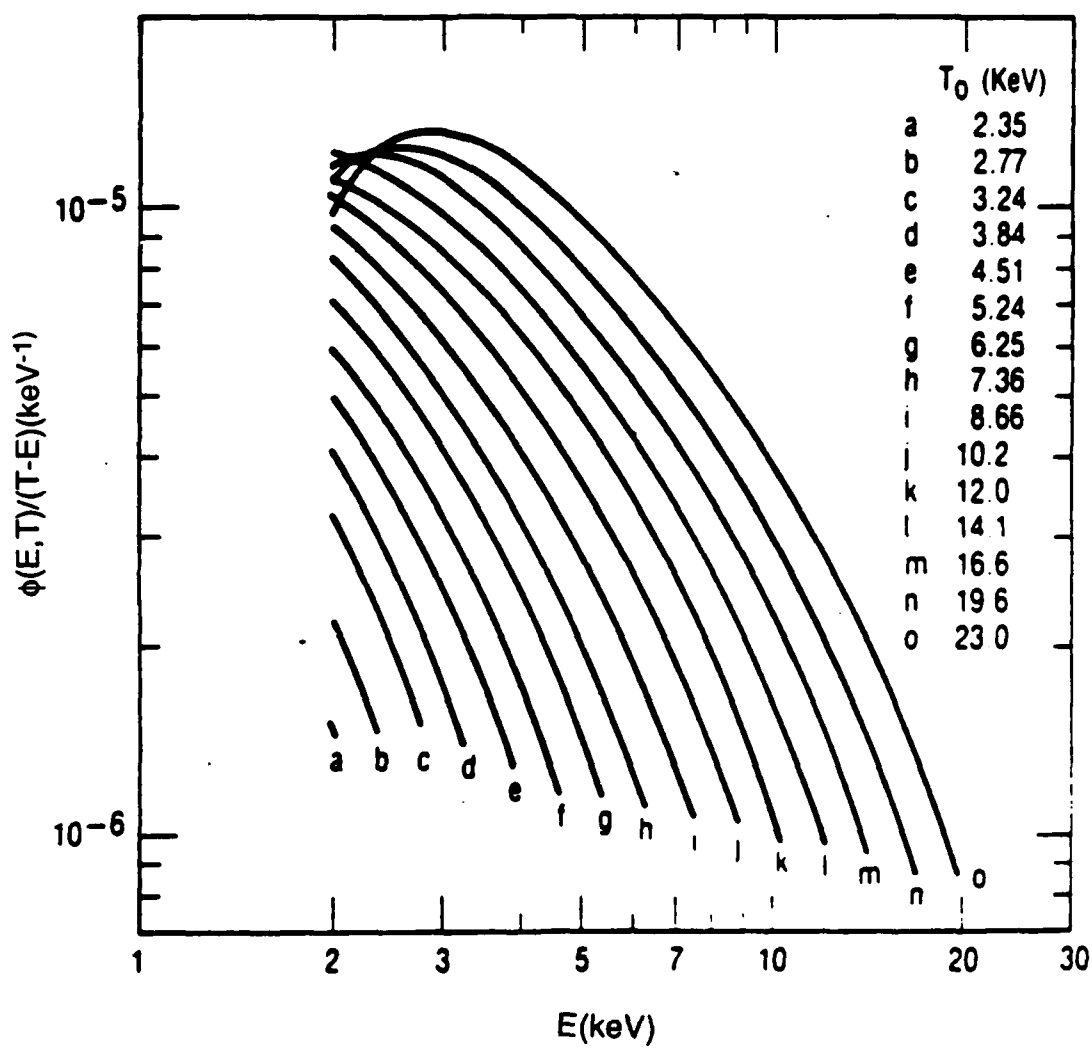
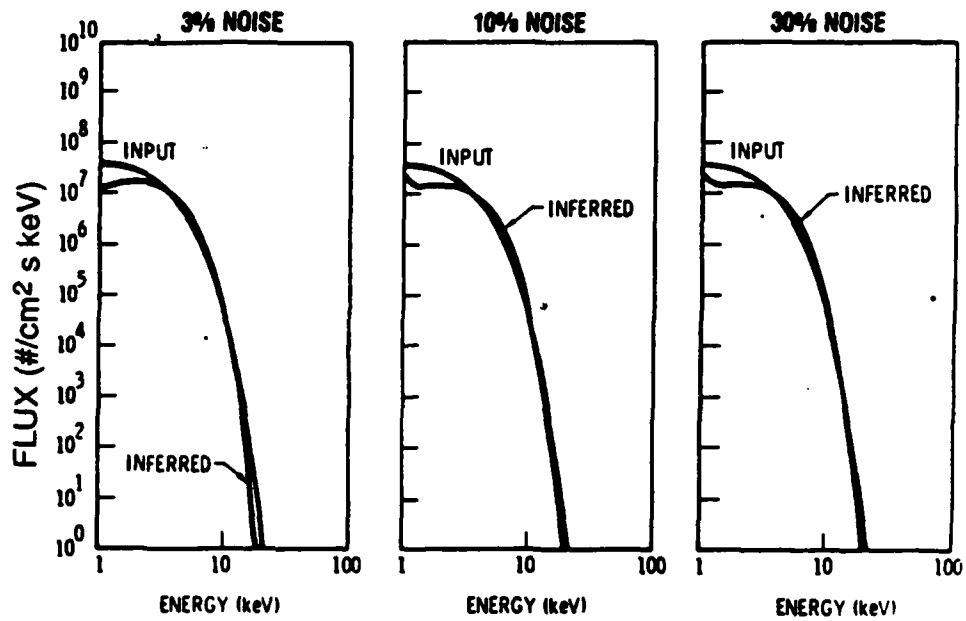


Figure 4.6

DECONVOLUTION FROM MODEL INPUT

1 keV Maxwellian



10 keV Maxwellian

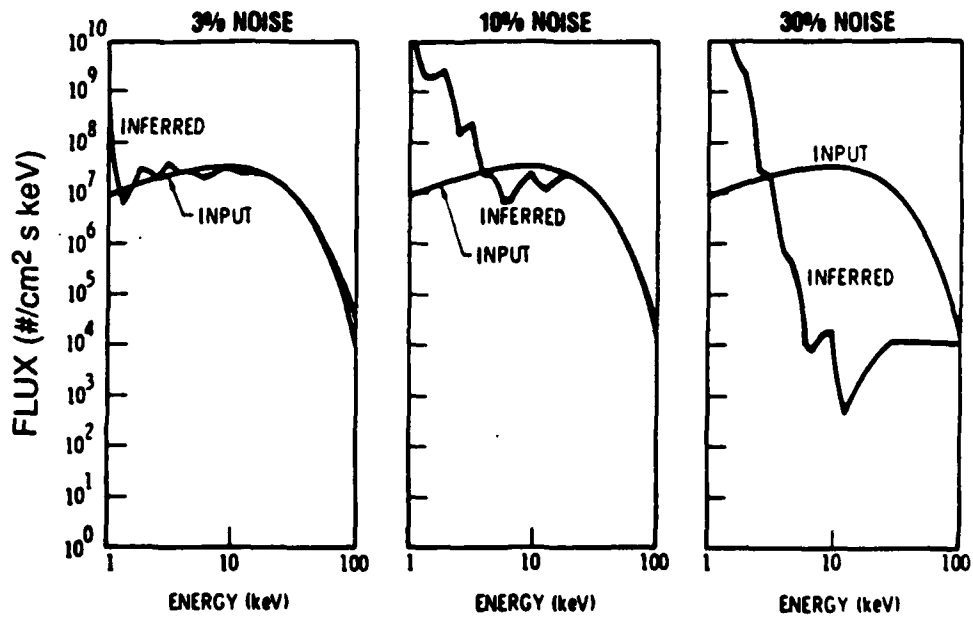


Figure 4.7

EXAMPLES OF DATA COVERAGE

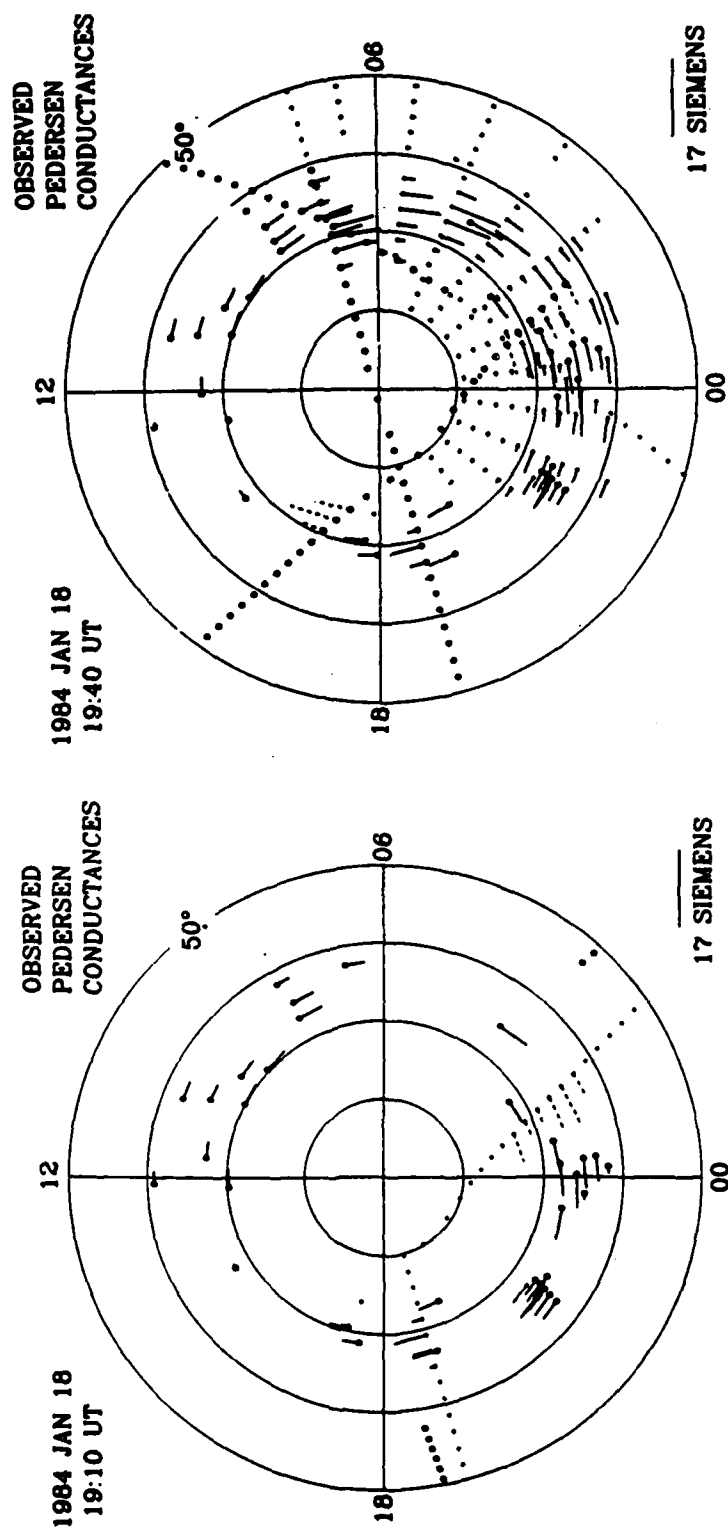


Figure 4.8

EVOLUTION OF CONDUCTANCE ESTIMATES

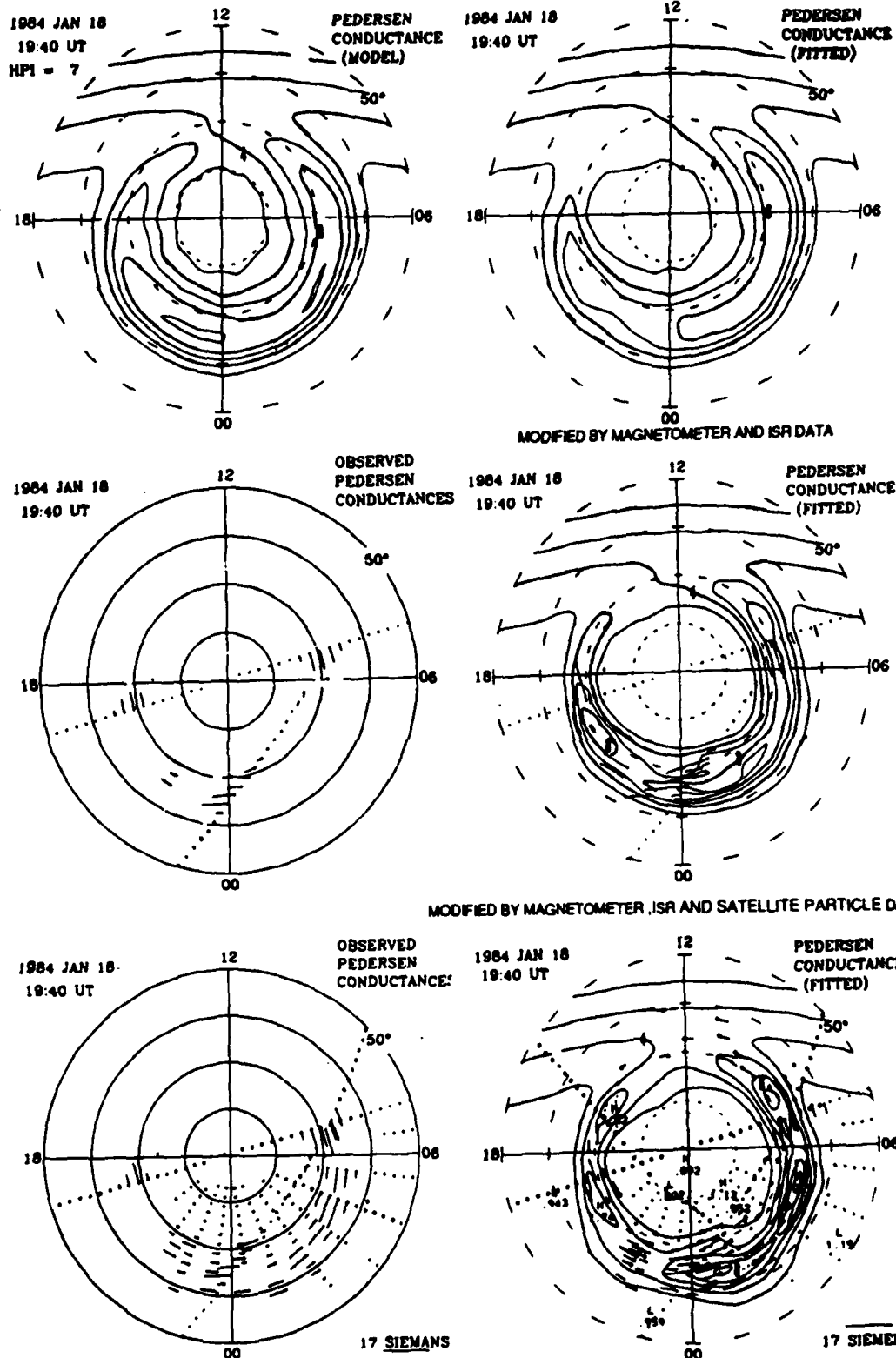


Figure 4.9

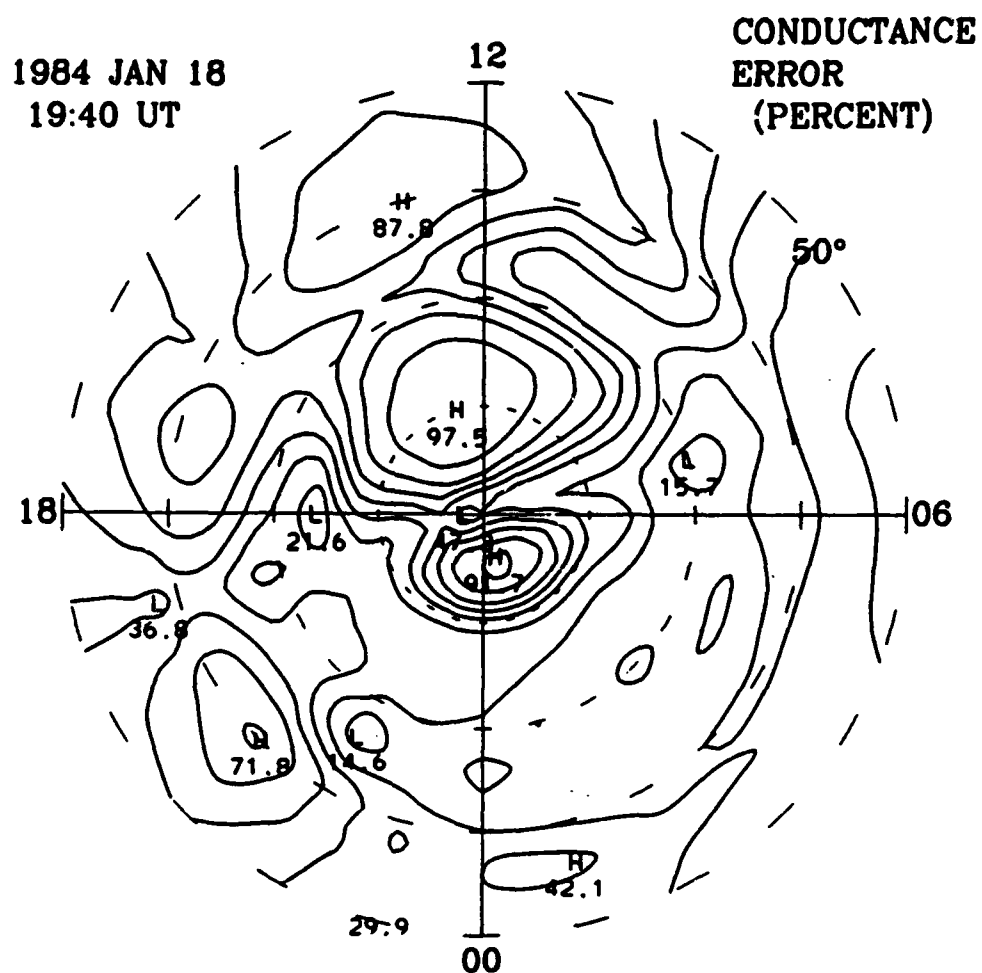


Figure 4.10

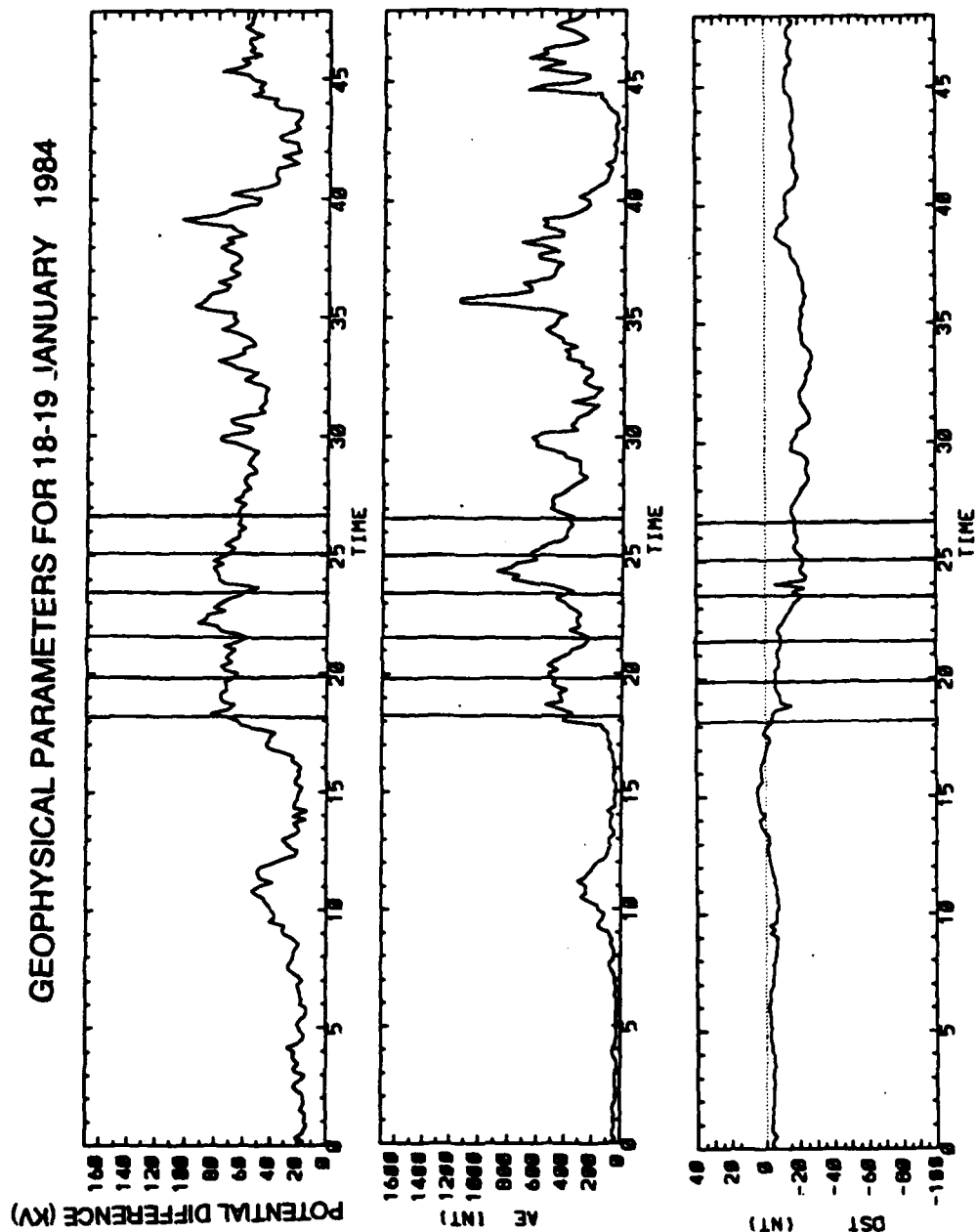


Figure 4.11

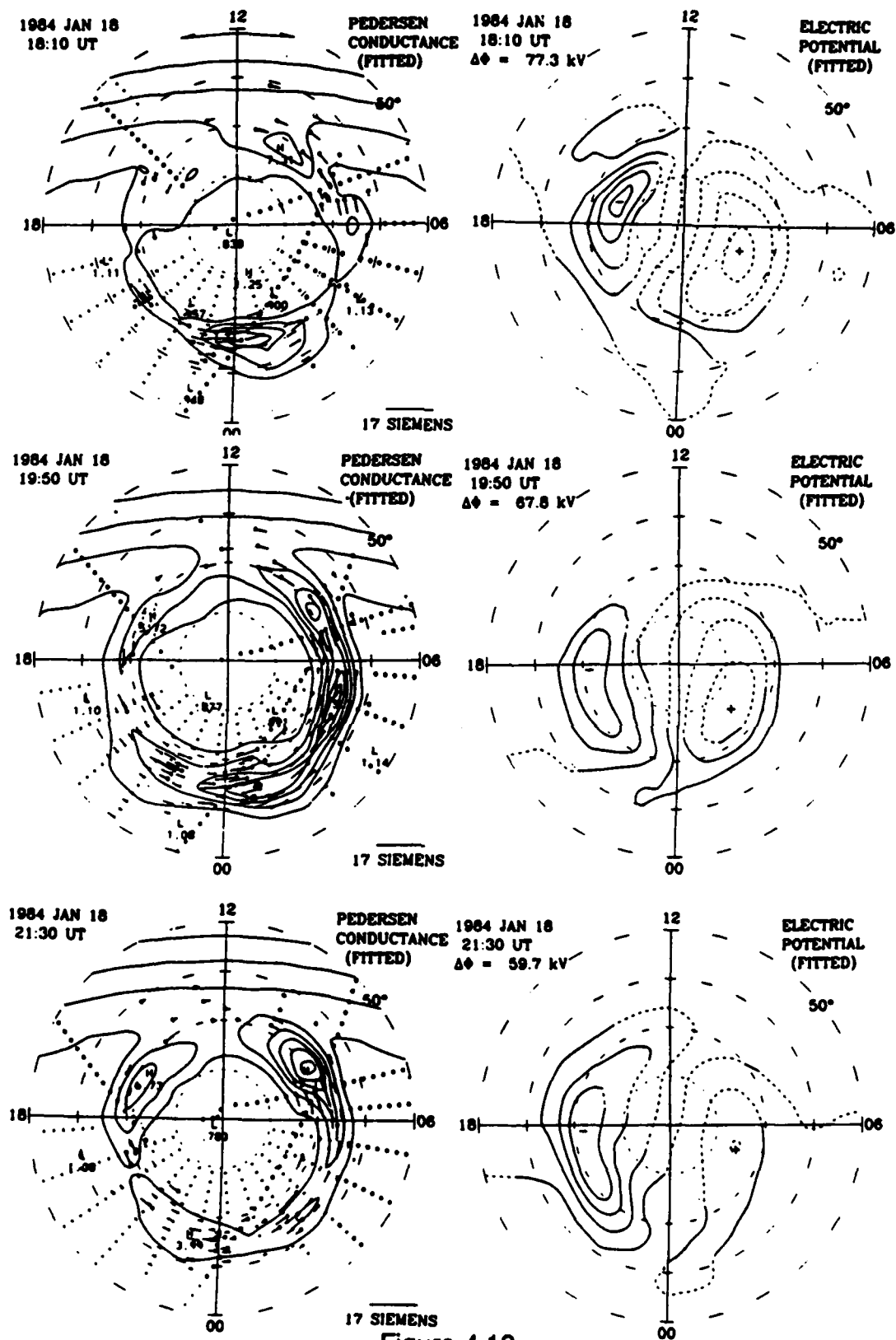


Figure 4.12

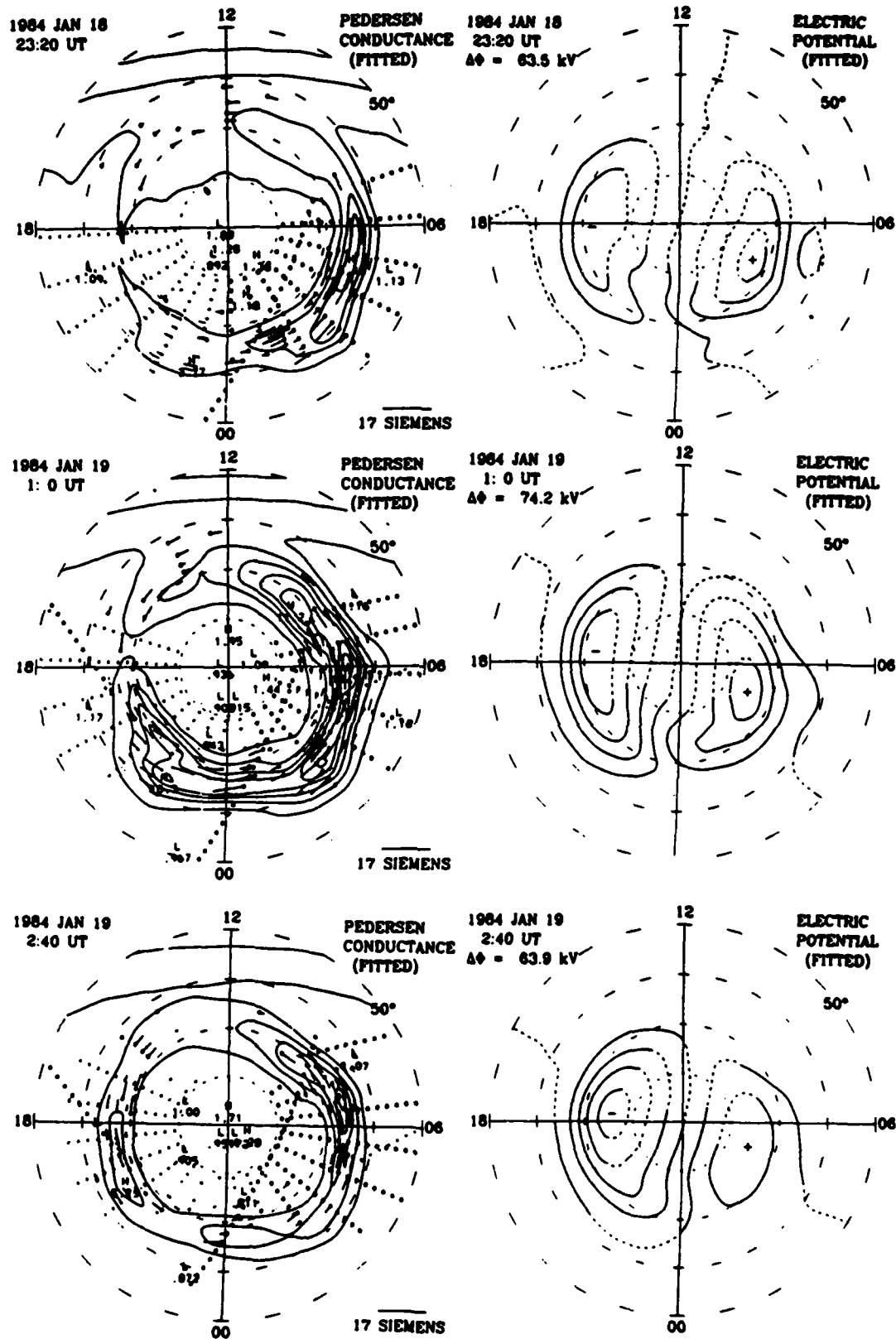


Figure 4.13

CHAPTER 5

MAGNETIC PERTURBATIONS AND CURRENTS

I. INTRODUCTION

Nearly 250 years ago A. Celsius discovered a connection between auroral events and disturbances in the earth's magnetic field. The connection remained largely a matter of curiosity until the beginning of this century when advances in radio technology and polar exploration provided new avenue of geophysical exploration. In 1908 the Norwegian scientist, K. Birkeland, hypothesized that charge carriers traveling along geomagnetic field lines were part of a three dimensional current system linking the upper atmosphere to the region we now call the magnetosphere. In the ensuing eighty years we have learned much about the phenomena of auroral disturbances and currents. We know that the three dimensional current system is actually a compound system consisting of a toroidal current originating in the ionosphere and a poloidal current system originating in the magnetosphere. We now understand that the auroral ovals, because of their high conductivity, channel the currents into narrow electrojets whose magnetic effects can be sensed at the ground. We have also learned that these currents are one mechanism among several for dissipating solar wind energy input to the magnetosphere. Although we understand, in an average sense, how these currents and energies are distributed, our knowledge of instantaneous variations is far more limited. The ALMEX procedure has been designed to address such shortcomings.

II. PHENOMONOLOGY

A. ELECTROJETS

It is prudent to ask "What accounts for the electrojets and field-aligned currents and their variations?" The evening and morning electrojets flow

respectively in the eastward and westward direction. Large scale electric fields imposed by the magnetosphere drive the ionospheric electrojets through the conducting auroral ovals. The dominant direction of the electric field in the evening auroral regions is poleward, while in the morning sector it is equatorward. Although both ions and electrons drift westward (eastward) in the evening (morning) regions under the influence of the electric field the greater mobility of the electrons generates a current in a direction opposite that of the particle motion. Thus, there is a westward current in the morning and an eastward current in the evening sectors. The ionospheric current is given by

$$\mathbf{J} = \sigma_0 \mathbf{E}_{\parallel} + \sigma_p \mathbf{E}_{\perp} + \sigma_h \left(\frac{\mathbf{B} \times \mathbf{E}_{\perp}}{B} \right) \quad 5.1$$

where \mathbf{E}_{\parallel} and \mathbf{E}_{\perp} are the electric field components parallel and perpendicular to the magnetic field respectively.

Because the earth's magnetic field lines are nearly equipotentials and are nearly vertical at high latitudes, it is conventional to assume that the electric field, \mathbf{E} , is approximately constant with height. The perpendicular component of equation 5.1, when integrated in height then gives

$$\mathbf{I}_{\perp} = \Sigma_p \mathbf{E}_{\perp} + \frac{\Sigma_h}{B} \mathbf{E}_{\perp} \times \mathbf{B} \quad 5.2$$

where Σ_p and Σ_h are the conductivity integrals over the transversely conducting ionospheric layer (usually 90-200 km) and \mathbf{I}_{\perp} is the height-integrated horizontal current. Typical horizontal current flows in the electrojets are on the order of 10^6 A and typical densities are on the order of 10^{-2} A/m² (Kamide, 1988). Closure of these currents may be through the polar cap or along geomagnetic field lines into the three-dimensional ionosphere-magnetosphere current system. The electrojets are channeled through rather narrow auroral ovals where the Hall conductance is sufficient to allow significant current flow. Hall

conductance values range from 5-50 Siemens (S) depending on geomagnetic conditions (Vickery et al., 1981).

Studies of ground magnetic perturbations show an asymmetric development of the westward electrojet during substorm expansion (Clauer and Kamide, 1985). The average location of the maximum westward electrojet is 0300 Magnetic Local Time (MLT) and 67° invariant latitude (Akasofu et al., 1980). However, during the maximum epoch of substorms there is a westward expansion of the maximum electrojet into the midnight region. The westward electrojet maximum returns to the 0300 MLT sector during recovery phase. Some of this asymmetry can be accounted for by the fact that the eastward electrojet is primarily controlled by variations in the northward electric field while both southward electric field variations and conductance enhancements control the westward electrojet. Near midnight it is primarily Hall conductivity that controls the westward electrojet (Kamide, 1988).

B. SUBSTORM CURRENT SYSTEMS

The rather marked variations in the H or X component of ground magnetic observations during substorm expansion has led to some investigations of the possibility of two types of contributions to the westward electrojet (Obayashi and Nishida, 1968). Equivalent current systems derived from stormtime magnetic perturbations frequently show a strong intensification of the westward electrojet in latitudinally limited regions on the nightside. The sequence of events, in this regard, can be summarized in the following manner. Shortly after a southward turning of the IMF a two cell current system, called DP 2 by Nishida (1968), develops at high-latitudes. A clockwise current dominates the morning sector and a counter-clockwise current flows in the evening sector. A sudden enhancement and longitudinal extension of the westward electrojet

signals a period when only a strong, single clockwise current system (DP 1) is evident. During recovery phase both an intensified DP 2 and a de-intensified DP 1 current system may be present.

Clauer and Kamide (1985) have investigated the relative dominance of DP 1 and DP 2 currents during periods of substorm activity. They comment on the resemblance of the DP 2 current system to the patterns of ionospheric Hall currents associated with the so-called convection electric field. The magnitude of the DP 2 current system is well-correlated with the IMF B_z indicating a correspondence between the two cell current pattern and the solar wind energy transfer to the magnetosphere (Kamide, 1988).

It appears likely that processes internal to the magnetosphere dictate DP 1 current system behavior. Clauer and McPherron (1974) and Baumjohann (1983) have proposed substorm current wedge systems that may explain the tendency for DP 1 presence near midnight. Significant conductivity enhancements produced by accelerated electrons during auroral breakup are likely to provide the conduit for the intensified current (Kamide, 1988).

C. FIELD-ALIGNED CURRENTS.

Field-aligned currents have been the center of much speculation. Birkeland (1908) proposed them as part of the closure for horizontal current system. However, competing closure theories challenged this notion and offered alternative closure paths. Chapman (1935) asserted that a unique determination of current density and configuration was not possible from surface magnetic observations. At that time such observations were the sole source of information on external currents. Fukushima (1969), using assumptions of steady currents, vertical field lines and uniform conductances, proposed that no effects from these currents could be sensed at the ground.

Hence, ground magnetic perturbations have often been treated as if they were completely attributable to overhead toroidal currents.

The speculation about the existence of field-aligned currents ended in 1972 with the launch of the TRIAD satellite. Well-documented satellite studies by Armstrong and Zmuda (1973), Sugiura and Potemra (1976), Iijima and Potemra (1976a, 1976b and 1978) and Zanetti and Potemra (1986) provided much information on average and extreme conditions of the field-aligned current sheets. Iijima and Potemra (1978) have provided the now classic diagrams of these current flows shown in Fig. 5.1. Satellite measurements show current flow into the ionosphere in the equatorward portion of the evening auroral oval and the poleward portion of the morning auroral oval. Outflowing currents are found in the high-latitude evening sector and the low-latitude section of the morning oval. Regions near noon and midnight exhibit rather complicated current patterns shown in Fig. 5.1. The high-latitude currents, referred to as "Region 1" currents by Iijima and Potemra (1978) are statistically larger and more persistent than the lower latitude "Region 2" currents. Indicating that (1) there is a net current flow in the poleward regions of the auroral oval and (2) the effects of this net current should produce a signal at the ground. The total current fed into and out of the ionosphere is on the order of several times 10^6 A during substorms and an order of magnitude less during quiet times (Potemra et al., 1978). Typical field-aligned current densities are on the order of $1\text{-}2 \mu\text{A/m}^2$ (Iijima and Potemra, 1976a).

The question of which particles actually carry the current has also been answered with the aid of satellite instrumentation. Although energetic electrons are accelerated into most of the morning auroral oval (constituting an upward current), the Region 1 current in the poleward portion of the oval is downward.

Such currents could be carried by a large population of magnetospheric ions but studies indicate such a population does not exist (Rostoker, 1987). Therefore, the upwelling of cold ionospheric electrons is left as the only possible source of this inbound current (Kaufmann and Kintner, 1984). Upwelling ionospheric electrons also appear to carry the inbound current in the evening sector (Rostoker, 1987). Energized precipitating electrons are responsible for most of the upward field-aligned current (Klumpar, 1976).

How do these field-aligned currents interact with the ionosphere? The answer is that these currents diverge into the auroral electrojets. One rather simplistic view of this interaction suggests that the field-aligned current flows horizontally from the inbound regions along a meridian and then exits the ionosphere along another field line as indicated in Fig. 5.2. This would imply perfectly matched sets of current sheets. However, some investigations have shown that the current sheets are not meridionally matched (Yasuhara et al., 1975). Therefore, some portion of the current appears to travel longitudinally or perhaps across the polar cap before exiting the ionosphere. Rostoker and Hughes (1977) and Clauer and McPherron (1974) offered an additional field-aligned current circuit to explain the strong substorm currents in the vicinity of midnight: the substorm current wedge. In this model the current is diverted from the midnight portion of the magnetotail, it then flows across the midnight auroral oval and exits in the vicinity of the Harang discontinuity.

D. JOULE HEAT

A second important facet of the field-aligned current-ionosphere interaction is the production of Joule heat. Field-aligned currents entering the resistive ionosphere deposit a portion of their energy as ohmic or Joule heat. For quiet levels of activity the power dissipated through Joule heating is on the

order of 4×10^9 W (Rostoker, 1987). Substorm power levels may reach 10^{11} - 10^{12} W (Burch, 1977). Both the spatial variations and the globally integrated value of joule heating are important for learning more about magnetospheric-ionospheric interaction. Instantaneous values of Joule heating are crucial to understanding the transfer and subsequent deposition of solar wind energy into the polar ionosphere. A number of investigators have studied the different aspects of this problem. Richmond (1979) and Roble (1982) have studied large scale effects of Joule heating on atmospheric dynamics. Ahn et al. (1983b) compared magnetogram estimates of Joule heating with estimates of Joule heating made by Chatanika radar and theoretical studies, while Kamide et al. (1982) used the KRM magnetogram inversion techniques and model conductances to generate Joule heating maps. Kamide et al. (1986) have modified that technique by including conductance derived from DE-1 auroral images. Recently, Rich et al. (1987) demonstrated the use of simultaneous particle and field observations in estimating Joule heating at high latitudes. In the AMIE procedure we are basically combining elements of all these techniques to generate instantaneous maps of global Joule heating.

III. ESTIMATING CURRENTS ELECTRIC FIELDS AND JOULE HEATING

A. BACKGROUND

Within the geophysics community there has been a long standing need for (1) a means of examining the response of the ionosphere-magnetosphere current system to the changes in IMF and to magnetospheric substorms and (2) relating the ionospheric current system response to the electric field. Investigating the behavior of the current system has been difficult because the location of the current carrying regions makes *in situ* observations difficult.

Additionally, while the signal produced by this joint system is recorded in ground magnetic perturbations, the contributions from the horizontal and field-aligned currents cannot be uniquely decomposed from those surface magnetic data alone.

In the last decade numerical procedures have been developed to invert a combination of ground magnetic data and model conductance information into estimates of other electrodynamic distributions such as field-aligned currents and electric fields (Nisbet et al., 1979, Kisabeth, 1979, Mishin et al., 1979 and Kamide et al., 1981). The AMIE procedure embodies much of the physics and numerics associated with the KRM procedure (Kamide et al., 1981), but now it adds the ability to estimate the conductance distribution as well and to incorporate other sources of information about the current systems such as the global distribution of the vertical component of ground magnetic perturbations, satellite magnetic perturbations and *a priori* information about the electric potential distribution. This section reviews the physical relations between the ionospheric and the field-aligned currents and the associated electric fields.

B. ASSUMPTIONS AND BASIC RELATIONS

As pointed out by Richmond and Kamide (1988) we can derive the ionospheric electric field, the field-aligned currents and the horizontal current from a variety of data under the following assumptions:

- 1) The electric field is electrostatic,
- 2) Geomagnetic field lines are equipotentials,
- 3) Electric fields and currents are related by Ohm's Law in the ionosphere, with known conductivities,
- 4) Dynamics effects of ionospheric winds can be neglected,
- 5) Geomagnetic field lines are radial,

- 6) Magnetic contributions for the magnetospheric ring current, the magnetopause currents and the magnetotail currents can be neglected.

These assumptions are combined with the following physical relationships to facilitate the data assimilation and estimation of electrodynamic patterns:

$$\mathbf{E} = -\nabla \phi \quad 5.3$$

$$\mathbf{I} = \Sigma \cdot \mathbf{E} \quad 5.4$$

$$J_{\parallel} = \nabla \cdot \mathbf{I} = \nabla(I_{\tau} + I_p) \quad 5.5$$

$$\Delta \mathbf{B}_{\text{sic}} = -\nabla V \quad 5.6$$

$$\Delta \mathbf{B}_{\text{sat}} = \mu_0 \hat{\mathbf{r}} \times \mathbf{I}_p \quad 5.7$$

where \mathbf{E} is the electric field, ϕ is the electric potential, \mathbf{I} is the horizontal ionospheric current, I_{τ} is the toroidal current, I_p is the horizontal component of poloidal current, $\Delta \mathbf{B}_{\text{sic}}$ are the surface magnetic perturbations, $\Delta \mathbf{B}_{\text{sat}}$ are the satellite magnetic perturbations, V is the scalar magnetic potential and $\hat{\mathbf{r}}$ is a unit radial vector.

C. DECOMPOSITION

1. Current Relations

Relating the magnetic deviations to the three dimensional current patterns is conceptually and computationally simplified if the height-integrated horizontal ionospheric current is considered as two parts: a toroidal current I_{τ} which circulates without divergence in the ionosphere, and a poloidal current I_p which is the ionospheric horizontal closure of field-aligned currents generated in the distant magnetosphere. Both of these components make a contribution to the height-integrated horizontal current, \mathbf{I}

$$\mathbf{I} = \hat{\mathbf{r}} \times \nabla \Psi - \nabla \tau \quad 5.8$$

$$\mathbf{I} = \mathbf{I}_{\tau} + \mathbf{I}_p \quad 5.9$$

where \hat{r} is a unit radial vector. The field-aligned portion of the current system is related to the gradient of the current potential, τ , while the toroidal current contribution is conveniently expressed in terms of the scalar equivalent current function, Ψ , which can be related to the horizontal equivalent sheet current, I_{equiv} , by

$$I_{equiv} = \hat{r} \times \nabla \Psi \quad 5.10$$

This fictitious current would produce the same ground magnetic effects as the actual three dimensional overhead current including the field-aligned current.

2. Surface Magnetic Perturbations Due to Poloidal Currents

a. Horizontal component

(1) External Contributions

The original KRM inversion procedure, on which AMIE is based, used ground magnetic measurements as its sole source of observations (Kamide et al., 1981). Measurements of magnetic perturbations still provide a sizeable portion of the electromagnetic information supplied to the AMIE procedure. Appendix IV shows how the magnetic perturbations are related to the magnetic potential and the current function and how Ampere's Law allows us to extract basic information on ionospheric currents from the perturbations. From spherical harmonic expansion of the magnetic perturbations the basic results are:

above the current shell

$$\Delta \mathbf{B}^+ = \sum_{n=0}^{\infty} \frac{\mu_0 n}{2n+1} \left(\frac{a}{r}\right)^{n+1} \nabla \psi_n - \frac{\mu_0 n(n+1)}{2n+1} \left(\frac{a}{r}\right)^{n+2} \frac{\psi_n}{a} \hat{r} \quad 5.11$$

and below the current shell

$$\Delta \mathbf{B}^- = \sum_{n=0}^{\infty} \frac{-\mu_0(n+1)}{2n+1} \left(\frac{r}{a}\right)^n \nabla \psi_n - \frac{\mu_0 n(n+1)}{2n+1} \left(\frac{r}{a}\right)^{n-1} \frac{\psi_n}{a} \hat{r} \quad 5.12$$

where a is the radius of the current shell.

Based on the observed ground magnetic data AMIE calculates an equivalent current function. Figure 5.3 shows observed magnetic perturbations, the fitted magnetic potential at ground level and equivalent current function for these data. The Laplacian of the equivalent current can be related to the electric potential through Ohm's Law. That is

$$\nabla_h^2 \Psi = \nabla \cdot (I_{\text{equiv}} \times \hat{r}) = \nabla \cdot (I \times \hat{r}) = \nabla \cdot (\hat{r} \times \Sigma \cdot \nabla \phi) \quad 5.13$$

Thus, we can relate the electric potential to the ground magnetic perturbations via the equivalent current. In this equation the conductance acts as a filter between the electric potential and the currents. A poor knowledge of the conductance implies a high uncertainty in the estimates of the electric potential from the current information.

(2) Subsurface current contributions

It is important to recognize that the contributions to the magnetic perturbations do not come solely from current systems flowing above the earth's surface. There can be a significant contribution from induced internal currents. Overhead ionospheric currents produce a "primary field." The variations in the primary field generate an electric field which in turn produces eddy currents in the conducting regions below the earth's surface. The secondary field, and hence the surface magnetic perturbations produced by the eddy currents, depends on the earth's conductivity structure as well as the history and period of external current variations (Parkinson and Jones, 1979). A complete treatment of these effects is not possible within the AMIE framework. Rather, these currents are treated as if they were induced on a perfectly conducting sphere located at a depth of 250 km below the earth's surface. This depth has been chosen based on the mean effective depth for the space and time scale of

magnetic perturbations under consideration (e.g., Richmond and Baumjohann, 1983).

As shown in Appendix IV currents flowing on such a conductor produce magnetic perturbations above the conducting shell given by

$$\Delta \mathbf{B} = - \left(\frac{c}{a} \right)^{n-1} \left[\frac{\mu_0 n}{2n+1} \left(\frac{c}{r} \right)^{n+1} \nabla \Psi_n + \frac{\mu_0 n(n+1)}{2n+1} \left(\frac{c}{r} \right)^{n+2} \frac{\Psi_n}{c} \hat{\mathbf{r}} \right] \quad 5.14$$

where c is the radius of the conducting shell. The effect of these currents is to increase the surface strength of the surface horizontal component of the external perturbations and reduce the external vertical component. The strength of the vertical reduction increases with depth since the sum of the external and internal vertical components vanish at the conductor surface.

b External Vertical Component

The AMIE procedure previously used only the horizontal component of magnetic perturbations as data input. We show that it is possible to assimilate the vertical component as well. The most direct use of this information is in determining the location and intensity of the electrojets as indicated in Fig. 5.4 but the mapping procedure also gains collateral information on the field-aligned currents and the electric field distributions from this data.

Other studies have used the vertical component of the ground magnetic perturbations to: (1) infer the location of the electrojets relative to magnetic observatories (Pytte et al., 1978), (2) aid in timing the onset of magnetic substorms (McPherron, 1978 and McPherron, 1979), (3) define the electrojet borders (Rostoker et al., 1978) and (4) infer field-aligned current contributions of the auroral electrojets (Wallis, 1976 and Kisabeth and Rostoker, 1977). Akasofu et al. (1981) and Friis-Christensen et al. (1985) used the vertical data for spatially limited data inversion for the Alaskan Meridian Chain and the

Greenland Magnetometer Chain, respectively, but instantaneous (~10 minute) vertical data have not been used in previous global inversion procedures. We modified the AMIE procedure to accept the vertical component information. It is assimilated via the formulation

$$\Delta B_z = - \frac{\partial V}{\partial r} \quad 5.15$$

as shown in equations 5.11 and 5.12 and Appendix IV. Figure 5.5 illustrates the impact of the vertical data on the equivalent current estimation.

There are at least two important effects that must be considered in incorporating this data: the geomagnetic coastal effect and a high frequency response effect. Both may introduce undesirable signals into the data. Parkinson and Jones (1979) and Jones (1981) discussed the impact of coastal variations and seawater conductivity on the vertical component data. They noted a high correlation between the vertical field and the direction of the local horizontal field near coastlines. The vertical component also exhibits a high frequency response to changes in the primary field. As a result geomagnetic pulsations and magnetic disturbances associated with the break-up phase of a substorm may produce anomalies in the vertical component which can be amplified by the coast effect (Küppers et al., 1979). We have dealt with this latter problem by averaging the vertical component data over thirty minute periods. The thirty minute filter may not be sufficient to eliminate the anomalies in all cases, but longer period filters may smooth out substorm effects which we are trying to map.

The coast effect (as well as other conductance anomalies) are more difficult to handle. A partial solution involves giving a low weight to those data from observatories known to have anomalies. Parkinson and Jones (1979) discussed, in rather general terms, the regions of anomalous behavior. They

identified Mould Bay, Alert and St John's in Canada as having suspect vertical measurements. The AMIE procedure will itself identify stations whose observations are different from the fitted values by some specified amount. Thus, we can check for observatories with consistent biases. Additionally, for the vertical component data set as a whole we calculate the ratio

$$\text{rms}(\text{computed difference/expected value of error})$$

As explained in chapter 4, if this ratio is not close to unity we can adjust the weight given to the entire data set. Weighting adjustments allow us to vary the fit of the estimated pattern to the data depending on our semi-objective determination of data validity.

3. Magnetic Perturbations Due to Poloidal Currents

The poloidal contribution to the height-integrated horizontal current comes from the closing of the field-aligned currents across the ionosphere and is assumed to produce *no magnetic effect* at the ground. Since these closing currents are curl-free they can be expressed in terms of a current potential function, τ . The local divergence of the height-integrated horizontal current arises from the entry and exit of vertical field-aligned currents. We express the field-aligned current density as

$$J_{\parallel} = \nabla \cdot \mathbf{I} = -\nabla^2 \tau \quad 5.16$$

Information about the field-aligned currents is derived from the divergence of the height-integrated current and from measurements of current flow above the ionosphere (i.e. satellite magnetic perturbations). Satellite magnetic perturbations measured above the ionosphere can be expressed as:

$$\Delta \mathbf{B}_{\text{SAT } (r=a)} = -\mu_0 \hat{\mathbf{r}} \times \mathbf{I}_p \quad 5.17$$

As shown in Appendix IV, Ampere's Law relates the magnetic perturbations to the field-aligned current at the satellite in the following way:

$$\hat{\mathbf{r}} \cdot \nabla \times \Delta \mathbf{B} = -\mu_0 J_{\parallel} = \mu_0 \nabla^2 \tau \quad 5.18$$

where J_{\parallel} is defined to be anti-parallel to \mathbf{r} (positive downward). We can combine this information with

$$J_{\parallel} = \nabla^2 \tau = \nabla \cdot \mathbf{I} = \nabla \cdot (\Sigma \cdot \nabla \phi) \quad 5.19$$

which affords us the means of relating the field-aligned current to the electric potential.

Fig. 5.6 shows one example of the impact of assimilating satellite magnetometer data on the field-aligned current estimation. The field-aligned current is intensified in the mid-morning sector where the gradients in the magnetic observations a broad region of downward flowing current. The satellite coordinate system is also shown with the observations and will be discussed in the Data Handling Section below.

Unfortunately satellite magnetometer measurements provide rather limited coverage, with at most two cuts through the field-aligned current sheets per polar pass. Satellite determination of the instantaneous global behavior of the field-aligned currents is therefore, not technically feasible and we must rely on assimilation of less direct measurements (notably ground magnetic data and conductance estimates) to provide estimates of field-aligned behavior. In this study we gain the bulk of the field-aligned current information from the divergence of horizontal currents: $-\nabla \cdot (\Sigma \cdot \nabla \phi)$. Therefore, our ability to estimate the field-aligned current distribution depends on both the conductance and its gradient.

D. JOULE HEATING

Ohmic or Joule heating results from magnetospheric energy input to the ionosphere. Maintaining a current in a conductor (the ionosphere) is possible only if energy is constantly supplied to the system. In a steady state situation

electrical energy cannot accumulate in a conductor. Consequently the supplied energy must be converted to another form. If we assume (as we do in AMIE) that neutral wind effects are negligible this energy will appear as Joule heating of the ionosphere. The rate at which work is done on the ionospheric system by the magnetosphere and therefore the rate at which Joule heating appears in the ionosphere is

$$\begin{aligned} Q &= -\mathbf{I} \cdot \nabla \phi \\ &= \mathbf{I} \cdot \mathbf{E} \\ Q &= \sum_p \mathbf{E}^2 = Q_J \end{aligned} \quad 5.20$$

The electric field used in this calculation can be represented as

$$\mathbf{E} = \mathbf{E}_0 + \hat{\mathbf{e}} + \delta \mathbf{e} \quad 5.21$$

where \mathbf{E}_0 is the statistical model value, $\hat{\mathbf{e}}$ is the estimated deviation of the true electric field from the model value and $\delta \mathbf{e}$ is the estimated error. Although the expected value of $\delta \mathbf{e}$ is zero, the statistically expected mean square value of $\delta \mathbf{e}$ is not zero (Richmond et al., 1989). This term must be accounted for in the squared electric field of equation 5.22. Richmond et al. (1989) treated the statistically expected value of \mathbf{E}^2 as

$$\langle \mathbf{E}^2 \rangle = \langle (\mathbf{E}_0 + \hat{\mathbf{e}})^2 \rangle + \langle \delta \mathbf{e}^2 \rangle \approx (\mathbf{E}_0 + \hat{\mathbf{e}})^2 + \langle (\delta \mathbf{e})^2 \rangle. \quad 5.22$$

The inclusion of the squared estimated deviation in effect corrects for the uncertainty in the electric field.

E. DATA HANDLING

The surface magnetic perturbations used as input for the AMIE procedure are the differences between disturbed day values and the average values for quiet days. A ring current contribution equal to the DST index multiplied by the cosine of magnetic latitude is subtracted from each north-south magnetic

component. As of yet no DST correction is made in the vertical component of the ground magnetometer data.

Satellite magnetic data have been provided by Dr. F. J. Rich of the Air Force Geophysics Laboratory. The magnetic perturbations sensed by the satellite magnetometer contain both a poloidal component associated with toroidal ionospheric currents (with the magnetic potential given by equation IV.16 of Appendix IV) and the toroidal component (given by equation IV.31 of Appendix IV) associated with the field-aligned current above the ionosphere. Since the small-scale poloidal field features associated with the high-order Legendre polynomials decay with altitude as a large power of $1/r$, at the height of the satellite, they will be weak, and the dominant small-scale magnetic features will be those of the toroidal component associated with the field-aligned currents. Larger-scale poloidal field components do not decay with altitude so rapidly, however, and may still be significant at the satellite.

In addition to the magnetic perturbations caused by the ionosphere and field-aligned currents, the satellite magnetometer also senses the much larger main geomagnetic field. Although most of the main field can be subtracted from the measurements by use of an empirical model, the residuals (due to minor inaccuracies of the empirical model) are comparable in size to the magnetic perturbations of the upper atmospheric currents. The residual main field contributions tend to vary relatively smoothly along the satellite track, because their sources lie at or below the earth's surface, so that the smallest scale features do not extend up to the altitude of the satellite. In order to minimize the influence of these unwanted magnetic perturbations, AMIE used the gradient of the magnetic perturbations along the satellite track. This enhances the relative importance of magnetic perturbations associated with field-aligned currents. It

also minimizes the relative importance of the perturbations associated with the toroidal ionospheric currents which are of large scale. A model main geomagnetic field has been subtracted from the data. Data from this study were processed by the Air Force Geophysics Laboratory (AFGL). Rich et al. (1987) described the processing necessary to remove the main field and noise. Even after the processing, high-frequency periodicities of likely spacecraft origin were still evident in the data. To eliminate possible ill-effects from these periodicities we averaged over 40 s intervals before taking the gradients of $\Delta \mathbf{B}$ along the satellite track. Figure 5.6 shows a representative data set of observed magnetic gradients and indicates the satellite orientation and the direction of field-aligned current flow.

FIGURE CAPTIONS FOR CHAPTER 5

Figure 5.1. (a). The "average" disturbed field-aligned current pattern from Iijima and Potemra (1976a). Black is current into the ionosphere and gray is current out. (b) An AMIE "instantaneous" disturbed pattern showing more structure but the same basic features as the average pattern. Solid contours represent downward current, dashed contours represent upward currents.

Figure 5.2. Illustration of two possible field-aligned current interactions with the ionosphere. The top panel shows a current wedge system corresponding to an ionospheric DP-1 current signal. The bottom panel illustrates the more frequently observed DP-2 convection signal. (From Clauer and Kamide, 1985).

Figure 5.3. Observed magnetic perturbations and corresponding fitted magnetic potential and equivalent current functions.

Figure 5.4. Idealized pattern of horizontal and vertical ground magnetic perturbations due to an overhead electrojet.

Figure 5.5. The impact of the vertical component magnetometer data. The top panel is an equivalent current pattern derived without vertical data. The middle panel shows the data overlying the fitted vertical pattern and bottom panel shows the estimated equivalent current pattern with the vertical component included.

Figure 5.6. (Left) mapped field aligned currents derived without satellite data, (Middle) The DMSP satellite magnetometer gradients across the northern polar region for the thirty minute period centered on 1940 UT 18 January 1984. The vectors represent the perturbations in the satellite measured magnetic field averaged over a 40 second period. The perturbations are mostly due to field-aligned currents flowing into and out of the high-latitude auroral region. A scale vector in the lower right shows the magnitude of a deflection of one pico-Tesla per meter. The satellite coordinate system; Down is into the page, forward is along the satellite track and cross track is perpendicular to the down and forward directions. Vectors lying on the dawn dusk side of the track are associated with upward field-aligned currents and vice versa. (Right) mapped field aligned currents derived after the inclusion of satellite magnetometer data. The data increase the magnitude of the currents in the mid-morning region.

AVERAGE AND INSTANTANEOUS FIELD-ALIGNED CURRENT PATTERNS

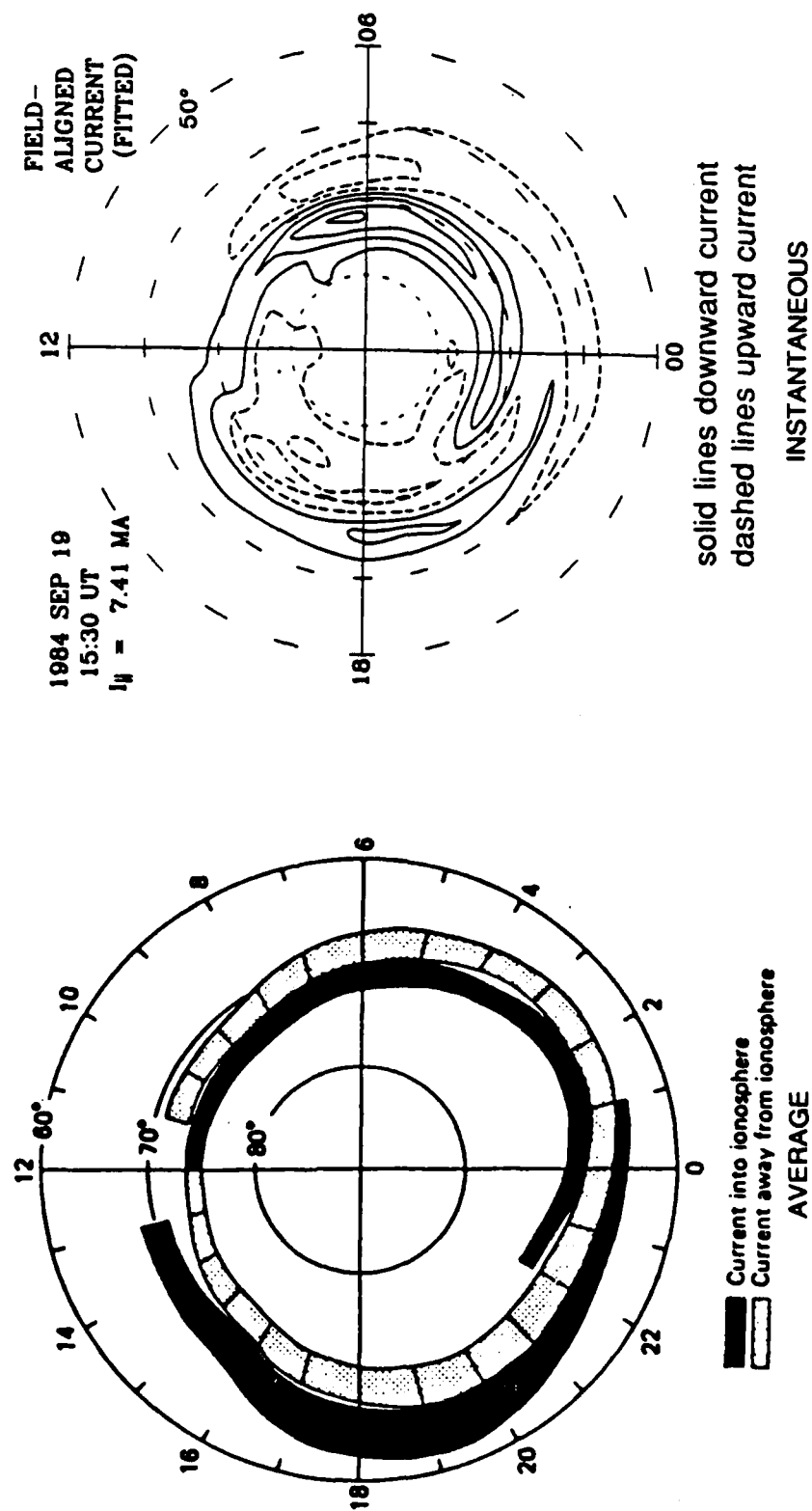


Figure 5.1

DP1 AND DP2 CURRENT SYSTEMS

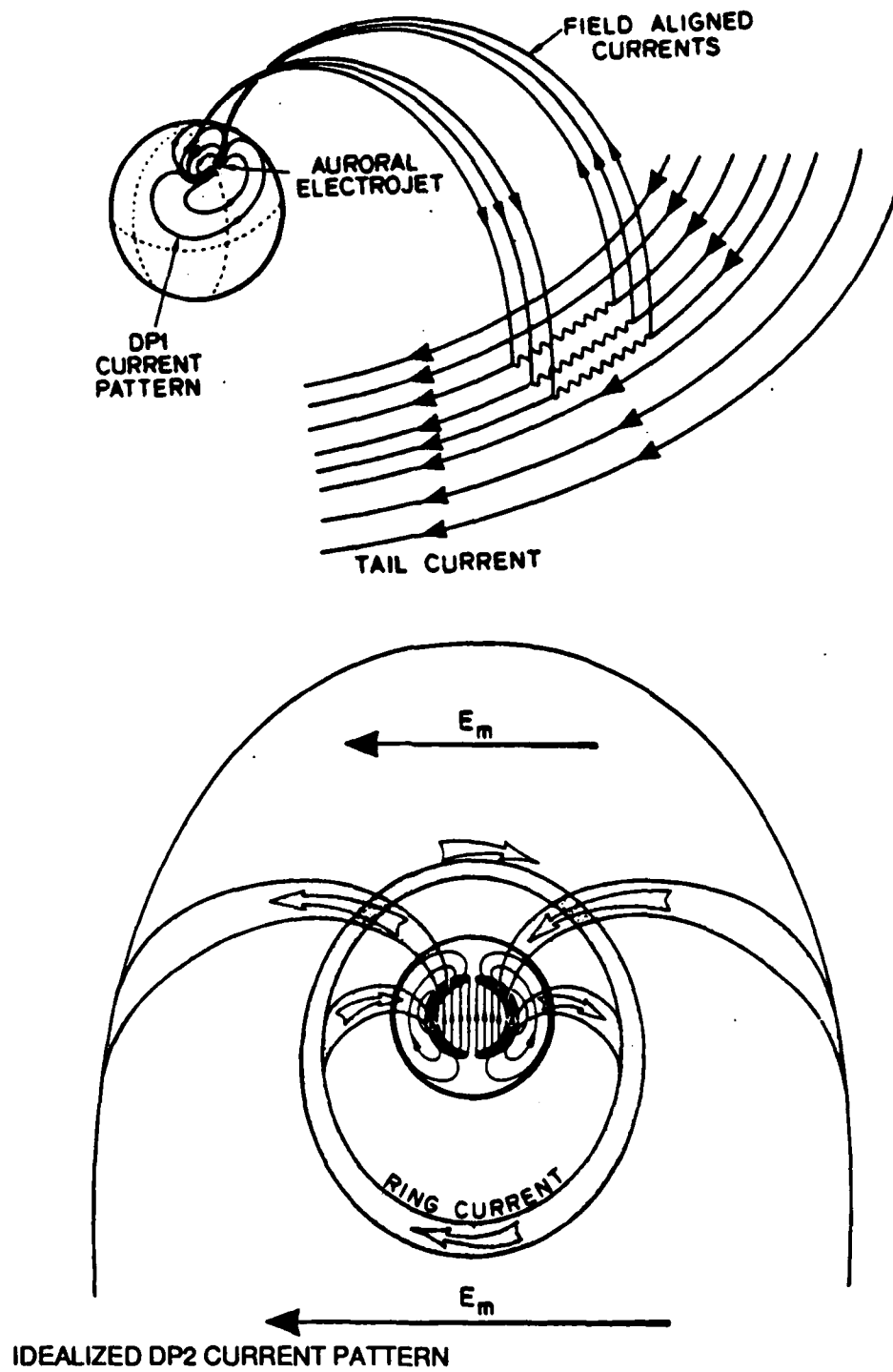


Figure 5.2

CURRENT POTENTIAL AND EQUIVALENT CURRENT ASSOCIATED WITH GIVEN MAGNETIC PERTURBATIONS

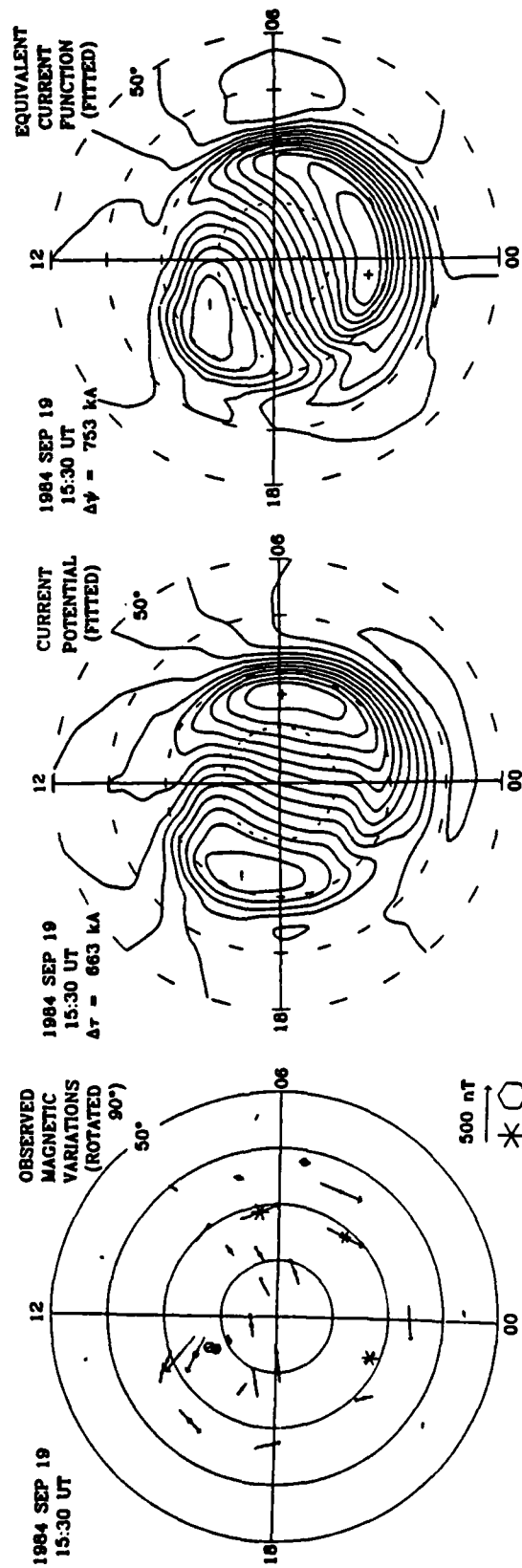


Figure 5.3

IDEALIZED MAGNETIC PERTURBATIONS DUE TO OVERHEAD CURRENT

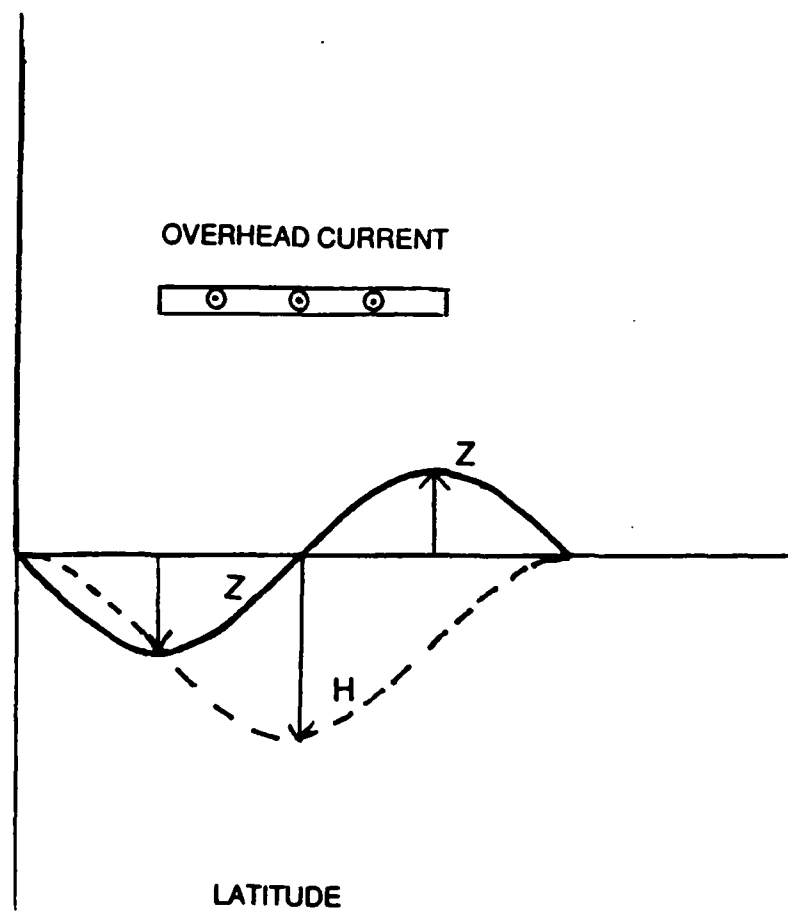


Figure 5.4

IMPACT OF ADDING VERTICAL COMPONENT OF GROUND MAGNETIC DATA ON EQUIVALENT CURRENT

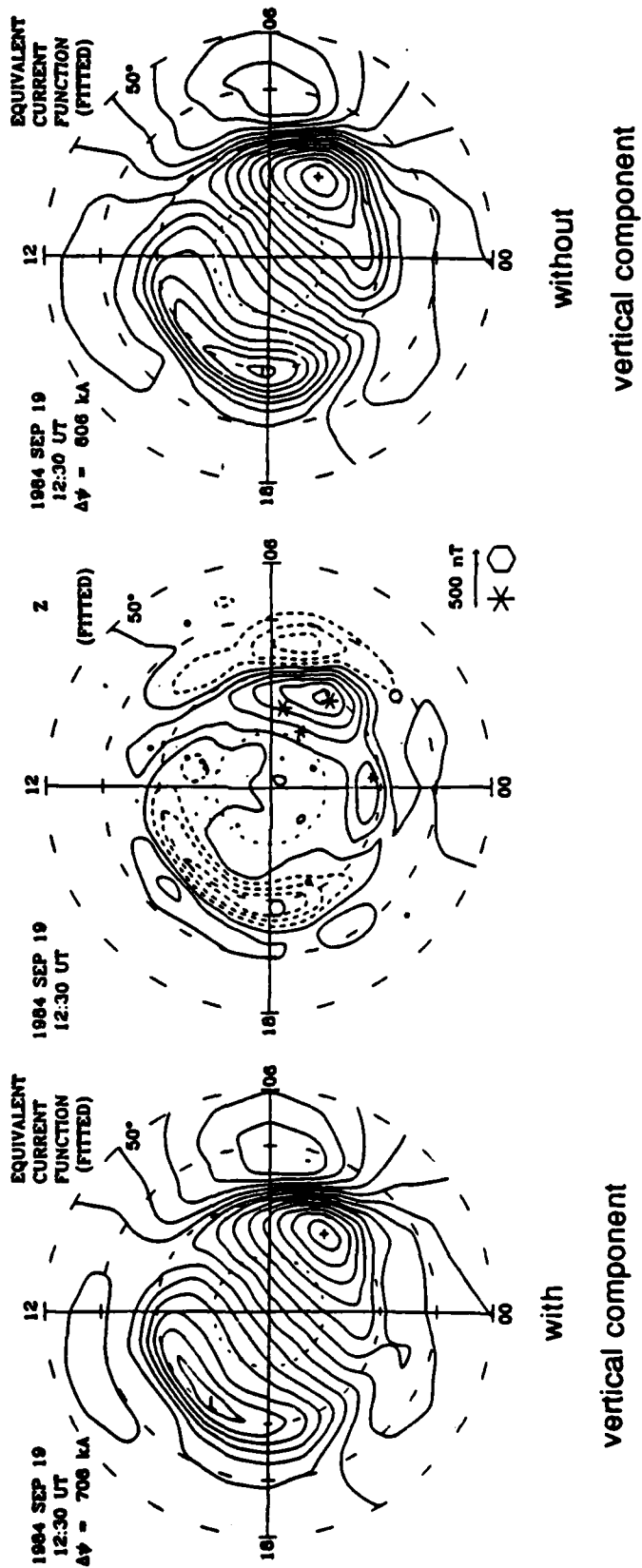


Figure 5.5

IMPACT OF ADDING SATELLITE MAGNETOMETER DATA

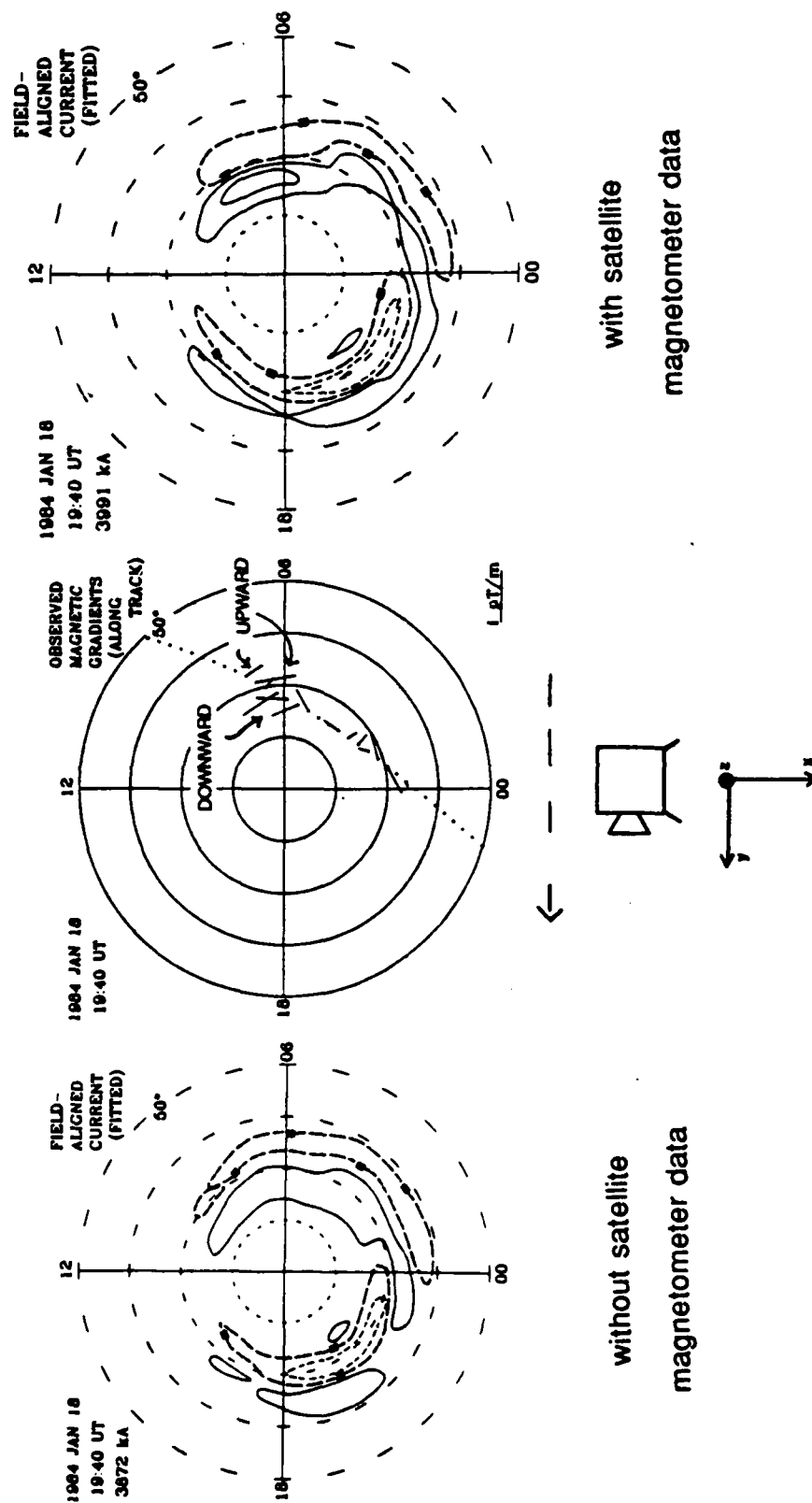


Figure 5.6

CHAPTER 6

SENSITIVITY

I. WEIGHTINGS

One of the first tasks in investigating the sensitivity of the AMIE procedure is to properly weight the input data. As mentioned in chapters 4 and 5 we make initial estimates of the proper weightings based on input from principal investigators. We then use AMIE output statistics to fine-tune the weightings. An example of this tuning is shown in Fig. 6.1 which shows the weighting ratio

$$\frac{\text{(rms of the computed differences between estimated patterns and data)}}{\text{(expected error)}}$$

for the 18-19 January 1984 conductance data. When the data are properly weighted this ratio is close to unity. The top panel shows the results with a "first guess" on the weighting. Increasing the weighting by a factor of three produces an overall ratio closer to one and is shown in the bottom panel. This procedure is used for all new data sets in this study.

II. GOODNESS OF FIT TESTS

We require some measure(s) of determining how sensitive the AMIE results are to different input data. Richmond et al. (1988) calculate a measure of the goodness of fit to the data from the ratio

$$\frac{\text{(weighted root mean square value of the fit errors)}}{\text{(weighted root mean square value of the data)}}$$

where the fit errors are the difference between the computed and observed data values and the weights are the inverse square of the expected statistical errors. We use this as one test for our new input data sets. We will refer to it as the fit ratio. The fit ratio approaches zero when the estimated patterns are in good agreement with the observations.

Figure 6.2 shows how the fit ratio (calculated every ten minutes) varies throughout the two day period 23-24 July 1983. The average value of the fit ratio when all data sources are included and appropriately weighted is 0.3402. Eliminating the X-ray conductance data (which should help link the magnetometer data to the electric fields) increases the fit ratio to 0.3420. We conclude that, on average, using the X-ray data improves the fit of the patterns to the data.

Increasing the number of estimated coefficients is another possibility for improving the fit of the patterns to the data. We tested estimates of 196 versus 121 coefficients and found a decrease (improvement) in the fit ratio when extra coefficients are estimated. The relative values are 0.329 (196 coefficients) versus 0.342 (121 coefficients). The comparative results for 23-24 July 1983 are:

FIT RATIOS 23-24 JULY 1983	
CONDUCTANCE	
WITH X-RAY DATA	.3402
WITHOUT X-RAY DATA	.3420
COEFFICIENTS	
121	.3402
196	.3291

The best fit ratio is obtained by assimilating the X-ray conductance data and estimating 121 coefficients.

To determine if the vertical component of the ground magnetometer data or the satellite magnetometer improve the reliability of the AMIE estimates we can compare the uncertainty in the estimated electric field with and without

these data sources. Figure 6.3 shows electric field estimates made with and without the vertical component of the ground magnetic data. In the region near dawn the estimate becomes more certain (as indicated by the appearance of more solid contours) with the inclusion of the vertical data.

Similarly, we may ask what happens to the uncertainty in the electric field when satellite data are included. Figure 6.4 shows two estimates of the electric potential pattern for 1150 UT on 19 September 1984. Figure 6.5 shows the magnetometer data contributing to the electric field estimate. The uncertainty in the estimated patterns is reduced when the satellite data are included and intensity of the electric field is markedly decreased.

We conclude that introducing satellite conductance estimates improves the AMIE fitting procedure, as does increasing the number of estimated coefficients. Assimilating the vertical component of ground magnetometer data and satellite magnetometer data improve the reliability of the electric field estimates in the vicinity of the new data. We have yet to include some factors such as DST correction for the vertical component which may provide further improvements in the reliability.

FIGURE CAPTIONS FOR CHAPTER 6

Figure 6.1. Graphs of the ratio

$$\frac{\text{(rms of the computed differences between estimated patterns and data)}}{\text{(expected error)}}$$

(a) The ratio consistently falls below unity indicating insufficient weighting of the data. (b) Increasing the weighting by a factor of three brings the ratio close to unity.

Figure 6.2. The fit ratio

$$\frac{\text{(weighted root mean square value of the fit errors)}}{\text{(weighted root mean square value of the data)}}$$

for the 48 hour period 0000 UT 23 July-2400 UT 24 July 1983.

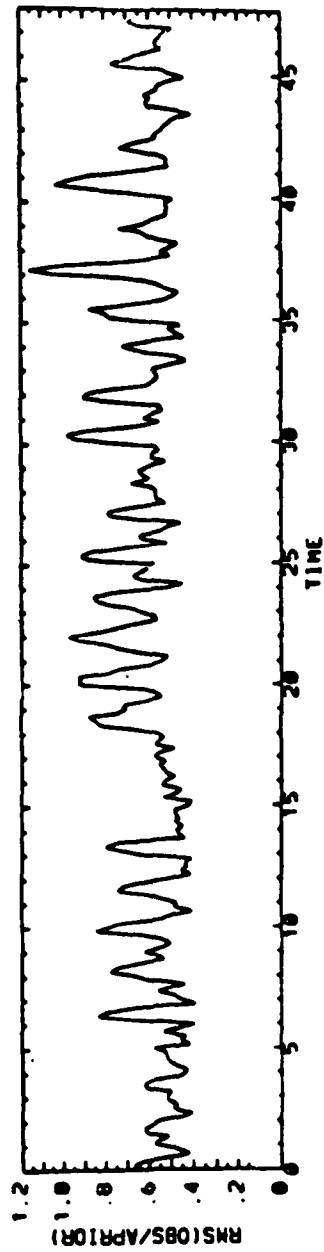
Figure 6.3. Electric potential patterns derived (a) with and (b) without the vertical component of the ground magnetometer data. The solid lines indicate the uncertainty is 50% or less. Introduction of the vertical data lowers the uncertainty of the patterns in the vicinity of dawn. Contours are every 10 kV.

Figure 6.4. Electric potential patterns derived (a) with and (b) without satellite magnetometer data. The solid lines indicate the uncertainty is 50% or less. Introduction of the satellite magnetometer data lowers the uncertainty of the patterns in the vicinity of the satellite track. Contours are every 10 kV.

Figure 6.5. The magnetometer data contributing to the estimates in Figure 6.4.

WEIGHTING RATIO FOR 18-19 JANUARY 1984

WEIGHTING RATIO FROM INITIAL TRIAL (FALLS BELOW ONE ON AVERAGE)



WEIGHTING RATIO AFTER FIRST ITERATION (APPROXIMATELY ONE ON AVERAGE)

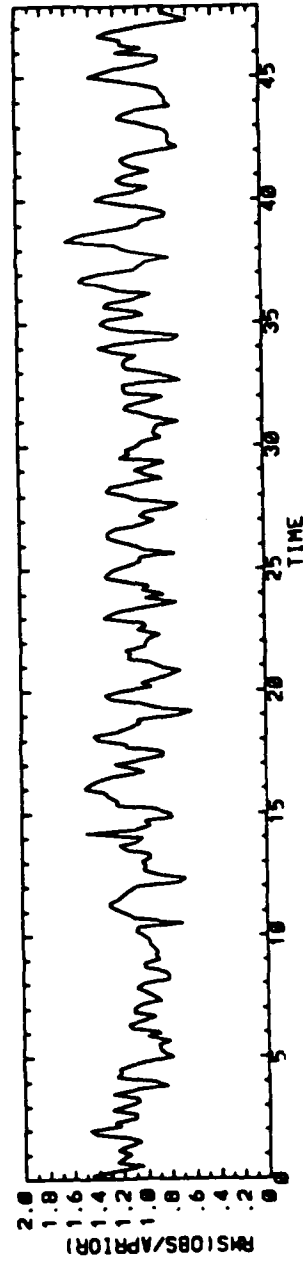


Figure 6.1

FIT RATIO FOR 18-19 JANUARY 1984

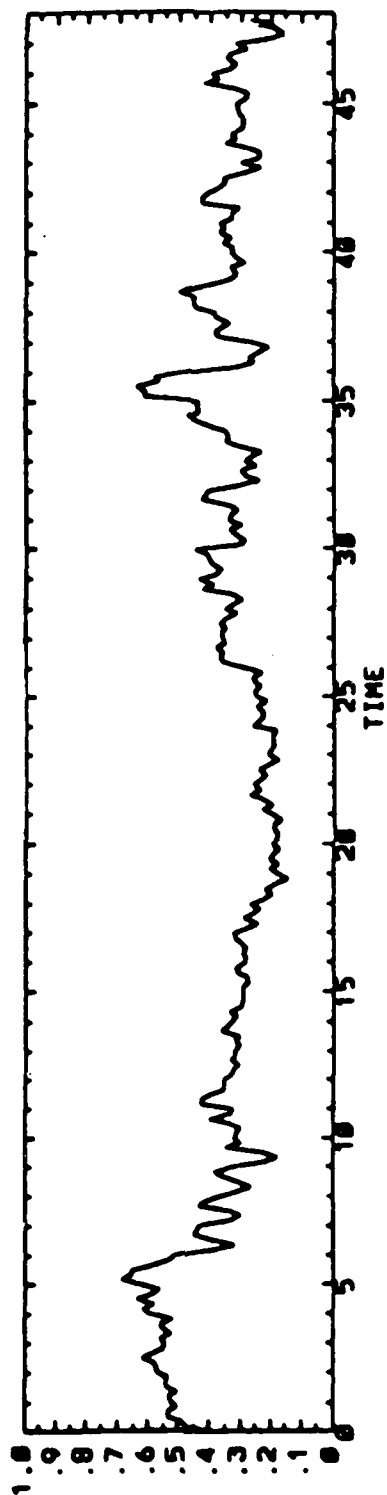


Figure 6.2

IMPACT OF VERTICAL COMPONENT OF GROUND MAGNETIC DATA ON ELECTRIC FIELD RELIABILITY

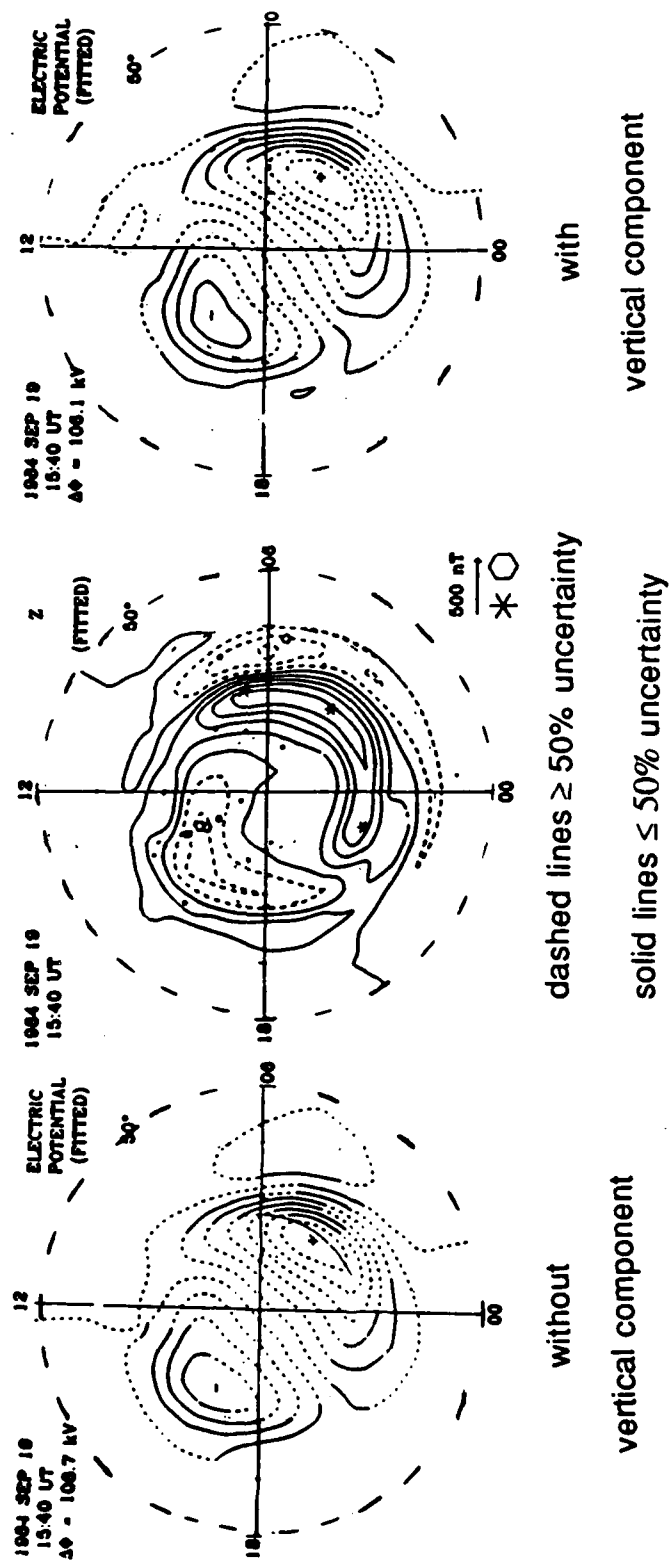


Figure 6.3

IMPACT OF SATELLITE MAGNETOMETER DATA ON ELECTRIC FIELD RELIABILITY

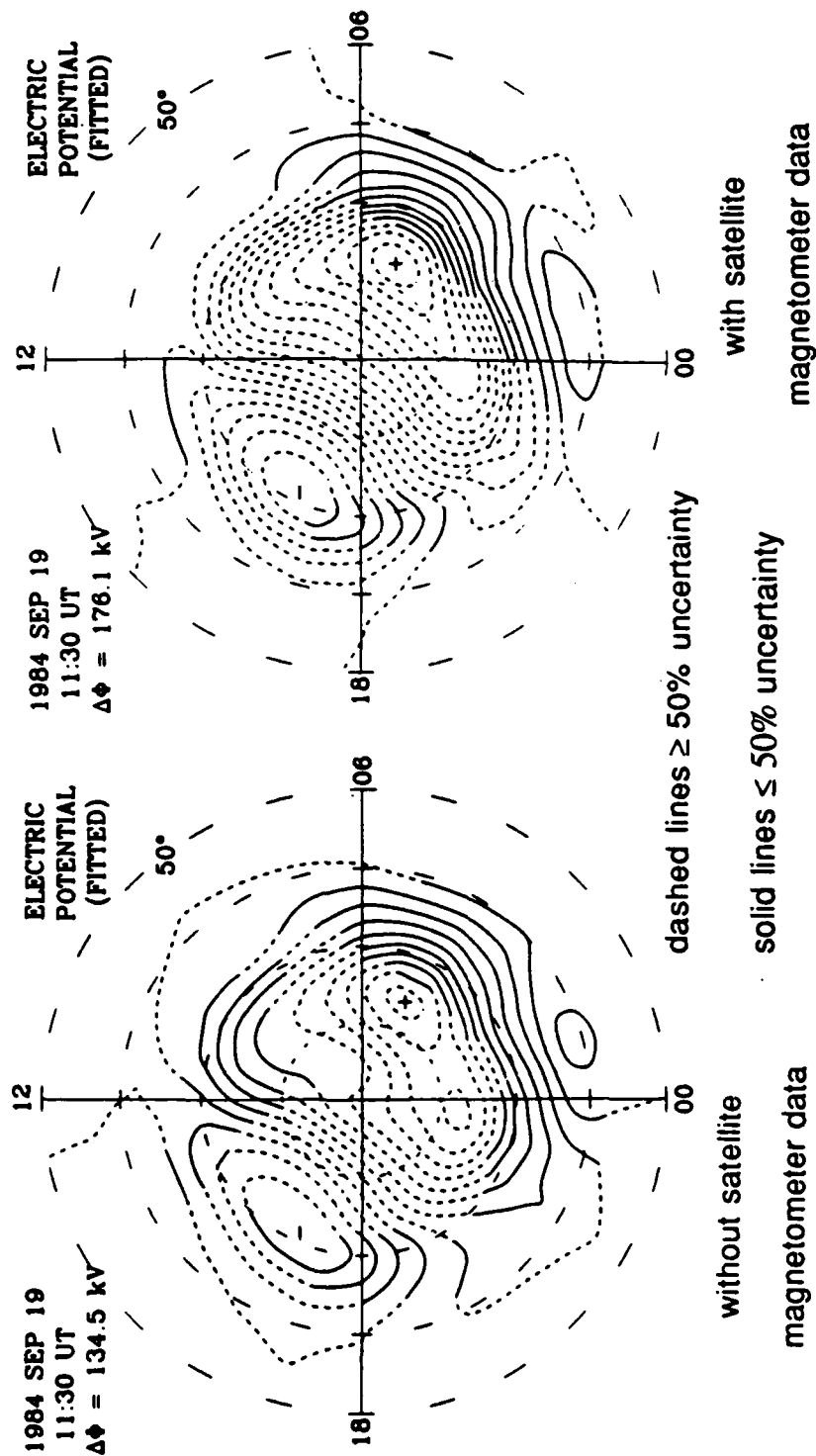


Figure 6.4

MAGNETOMETER DATA CONTRIBUTING TO ESTIMATES IN FIGURE 6.4

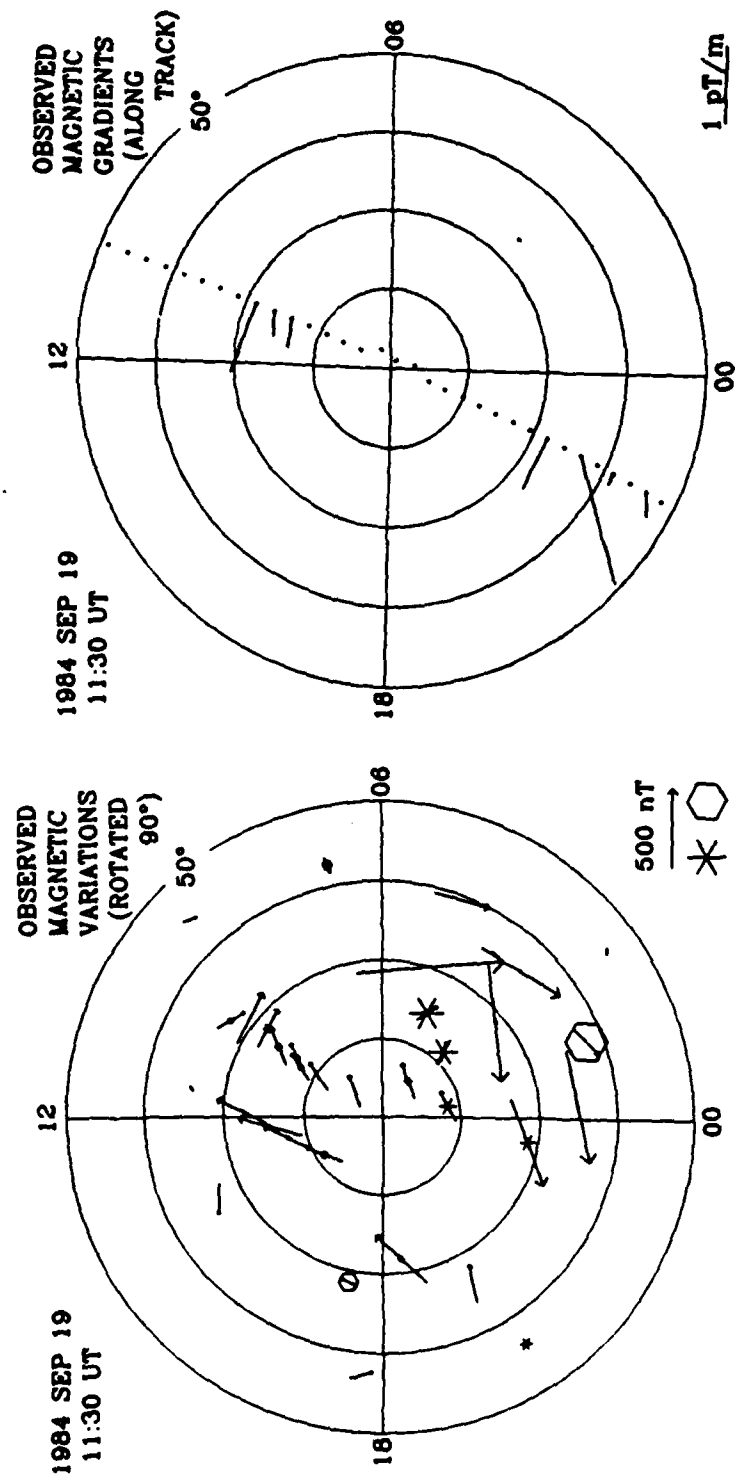


Figure 6.5

CHAPTER 7

GEOFYSICAL RESULTS

I. INTRODUCTION

In this chapter we present selected results from two periods: 23-24 July 1983 and 19 September 1984. We focus on four significant sets of results: (1) the development of DP1 and DP2 current systems, (2) IMF B_y effects, (3) IMF B_z northward effects and (4) Joule heating variations.

II. DP1 AND DP2 CURRENT SYSTEM VARIATIONS

Figure 7.1 shows the IMF data, geomagnetic indices and derived parameters for 19 September 1984 from Knipp et al. (1989). Figure 7.2 shows the AU and AL indices for the same period. The interplanetary magnetic field (IMF) B_y and B_z components are from the ISEE-2 spacecraft before 0400 UT and after 2100 UT and from the IMP-8 spacecraft between 1400 UT and 2100 UT. The AE index, obtained from the World Data Center C, is the standard 12 station measure of auroral activity. The Dst index is more a measure of ring current activity, and hence, a rather indirect indicator of ionospheric disturbance. NOAA satellite particle precipitation measurements are used to derive the Hemispheric Power Index (HPI). This index is primarily a measure of particle energy transfer between the magnetosphere and the ionosphere. The remaining curves in Fig. 7.1 are deduced from the output of the AMIE fitting procedure. Their definitions have been provided by Richmond et al. (1989). The total equivalent current is the difference between the maximum and minimum values of the equivalent current function. The total Joule heat is the areal integral, above 50° magnetic latitude, of the height-integrated Joule heating including the correction discussed by Richmond et al. (1989). The total field-aligned current is one-half the area integral above 50° magnetic latitude, of

the absolute value of the large scale field-aligned current obtained by the AMIE procedure. The electric potential difference is also extracted from the AMIE output northward of 50° magnetic latitude.

The IMF B_y and B_z components were close to zero before 0400 UT. Both the ISEE and IMP spacecraft were in the magnetosheath between 0400 UT and 1400 UT, so IMF data are unavailable during this period. After 1400 UT the B_y component was generally positive and the B_z component generally negative for several hours before tending towards values fluctuating about zero towards the end of the day. The negative B_z values are associated with the disturbed features evident in the traces below.

The auroral zone was experiencing moderate particle precipitation and only modest magnetic perturbations until approximately 0920 UT. At that time a small pulse of activity initiated the transition from a quiet epoch to a highly disturbed period within which the AE value exceeded 1000 nT for about two hours, reaching peak values of 1332 nT at about 1100 and 1200 UT. Although some recovery occurred after 1200 UT, the AE index remained above 400 nT indicating that the ionosphere probably did not return to a quiet state before the beginning of subsequent substorms. The Dst trace also reflects the sharp transition from quiet to disturbed conditions beginning at approximately 0920 UT. Smaller effects from the later disturbances are less distinct but still evident in the record. The AE and Dst indices appear reasonably well correlated.

We do not see the same degree of correlation between the three disturbances and the HPI trace. The rise in HPI at approximately 1000 UT appears to be associated with the general disturbance of the first substorm. But, unlike the other indices the HPI does not decline after substorm 1, rather the HPI remains elevated for nearly the entire day. The equivalent current, total

Joule heating, total field-aligned current and potential difference derived from the AMIE procedure are found to correlate well with the AE index. For instance the correlation between the potential difference and AE is .91. A fairly high level of correlation between AE and the derived parameters is not surprising since most of the information in the estimates come from the magnetometer data.

All of the derived global parameters show at least three disturbances occurring after 0920 UT. Of these the first disturbance was the most intense and of the longest duration. A peak of 153 kV was calculated for the potential difference at 1050 UT. Although each parameter shows a slightly different decay rate after the peak of the substorm there is a definite plateau of activity after 1300 UT. Two later substorms beginning around 1430 UT and 1800 UT, respectively, are also evident in the parameter traces. They are both less intense than the first substorm and they appear to be disturbances superimposed on an already disturbed ionosphere. Some level of disturbance continues throughout the day. None of the geophysical indices or parameters decreases to the low levels recorded earlier in the day.

Figure 7.3 shows a comparison of the AMIE derived potential difference with the potential difference arising from the statistical model provided by Foster et al. (1986). During the first nine hours of the day the two potentials usually differ by less than 20 kV. More substantial differences develop shortly after onset of the first substorm. At the peak of the first substorm (1050 UT) the AMIE derived potential difference of 153 kV is nearly double the statistical value of 80.5 kV. In general the AMIE procedure produces enhanced potential differences during all the significant disturbances in AE. The statistical potential differences, while showing a definite elevation between 1000 and 2000 UT, do

not suggest the variations in the electrodynamic state indicated by the AE index during that period.

Figures 7.4 through 7.6 present mapped electrodynamic parameters from 0950, 1050, and 1150 UT. These times correspond to the beginning, maximum, and recovery of the first substorm. In comparing the conductance maps we observe an equatorward expansion of the oval between 0950 and 1050 UT. Between 1050 and 1150 UT the oval remains expanded and the conductance is significantly augmented on the morning side. (One note of caution is necessary for the 1050 UT conductance plots--at that time all satellite data are from the south pole. The NOAA satellite providing data in the evening sector experienced a data loss which may be associated with very energetic precipitation. We note that particle precipitation is observed as far equatorward as 52° magnetic latitude). The late night conductance may be significantly under estimated.

Perhaps the most notable pattern variation is in the equivalent current maps. Within the course of one hour the total current more than quadruples. For a short period of time between (1030 and 1050 UT) the equivalent current pattern is dominated by a one cell which corresponds to the single vortex system of Akasofu et al. (1965). The concentration of current in the midnight region is a signature of the DP 1 current system proposed by Obayashi and Nishida (1968) and may represent the diversion of magnetotail current via a field-aligned current into the ionosphere as proposed by McPherron et al. (1973) and Clauer and McPherron (1974). The two vortex pattern reappears by 1100 UT and is quite evident in the 1150 UT equivalent current plot. The retreat of the auroral electrojet to the early morning hours is consistent with the decay of DP 1 current described by Kamide (1988).

In comparing the AMIE results of Figs. 7.4-7.6 with the AU index of Fig. 7.2, we see an interesting coincidence of the derived westward electrojet intrusion into the evening sector and a decline in the AU index. In general, increases in magnetic activity increases the magnitude of AU but if the westward electrojet penetrates far enough into the nightside the resulting magnetic deviation at the ground may appear as an inverted magnetic bay (decrease in AU). McPherron (Private communication, 1989) suggests such a scenario between 1020 and 1100 UT. The AMIE equivalent current maps show an electrojet penetrating westward as far as 2200 MLT during that period.

We also note the westward rotation of the electric potential pattern at 1050 UT with an extreme concentration of the electric field in the pre-midnight region. Such a rotation has been associated with space charge build-up due to a conductivity discontinuity at the boundary between the discrete and diffuse aurora by Yasuhara and Akasofu (1977). Although, in this case the limited conductance observations may play a role in the rotation, the rotation is consistent with the nightside intrusion of the current system. The expanding/contracting polar cap model employed by Moses et al. (1989) also produces the pre-midnight electric field concentration. They relate the electric field concentration to strong plasma flow through a nightside convection gap that maps to the magnetotail reconnection region. The pre-midnight field concentration and the intruding electrojet disappear by 1150 UT.

Comparison of the Joule heating plots for the three times shows more than an order of magnitude increase in Joule heating between 0950 and 1050 UT. The magnitude of Joule heating declines only slightly between 1050 and 1150 UT but the change in the distribution is quite marked. The bulk of the Joule heating is associated with the westward electrojet at 1150 UT but occurs

predominantly in the morning sector compared to the midnight heating at 1050 UT.

The indices and the derived parameters indicate the ionosphere did not return to a quiet state after the first disturbance. Figures 7.7 through 7.9 present mapped results from 1430, 1530, and 1630 UT. At 1430 UT a relative lull in activity is shown. The polar-cap potential difference begins to increase at 1440 UT. This increase is followed by two hours of almost steady enhanced convection. As indicated in the various maps of Figs. 7.7 and 7.8 (and other plots not shown) minor variations occur but the overall characteristics of the patterns are remarkably steady through 1700 UT.

The series of events shown in Figs. 7.4-7.9 are consistent with the electrodynamic consequences of a plasmoid ejection as suggested by Russell and McPherron, (1973) and Hones, (1977). The events of the first disturbance may correspond to a plasmoid ejection, and the formation of a near earth X-type neutral line with an associated current diversion. Subsequent disturbances are less energetic and may correspond to a relatively steady reconnection of magnetotail field lines perhaps generated by slight southward turnings in the IMF and the slow addition of magnetic flux to the foreshortened magnetotail (McPherron, private communications, 1989).

III. RESPONSE TO IMF VARIATIONS FOR 23-24 JULY 1983

Figure 7.10 shows IMF data, geomagnetic indices and AMIE derived parameters for 23-24 July 1983. The first five hours of 23 July 1983 were characterized by relatively low IMF field-strength. After 0500 UT the IMF was moderately strong with southward and eastward components. Two periods of southward IMF precede a sharp, strong northward turning at 1010 UT. The IMF

remained northward for several hours as a slow shift from B_y eastward to B_y westward developed. We estimate a return to southward IMF conditions around 1850 UT, which results in nearly continuous substorm-like activity until 0800 UT on 24 July. After 0800 UT on 24 July sporadic but occasionally more intense disturbances occur. With the exception of the first five hours of the 48 hour period is almost continually disturbed. We note that the AE (12) index does not convey the true level of disturbance because high-latitude stations affected by northward IMF disturbances are not included in the index. We have recalculated AE using all stations and find better agreement between the revised AE index and the AMIE parameter estimates.

The variations in IMF B_y and B_z generate dramatic differences in the individual maps. To illustrate these variations we present a series of electric potential patterns in Figs. 7.11-7.14. The IMF B_z and B_y components are listed in the lower left of each pattern, but it should be kept in mind that the ionospheric response lags the IMF by approximately thirty minutes.

The pattern at 0830 UT on 23 July is consistent with a southward, eastward IMF ($B_z < 0$, $B_y > 0$) as shown by Potemra et al. (1979), Reiff and Burch (1985), Friis-Christensen et al. (1985) and Heppner and Maynard (1987). The positive B_y component stretches the morning cell across noon forcing plasma to transit from afternoon to morning through the convection from the dayside to the nightside.

Shortly after 1000 UT the IMF turns sharply northward but maintains a slight eastward orientation. The strong northward IMF component is sufficient to produce a complete convection reversal as proposed by Dungey (1961), and Russell (1972) and as illustrated by Maezawa (1976). In Fig. 7.14 we follow the development of this reversal at 10 minute intervals. Between 1030 and 1040

UT the character of the dayside ionosphere changes in response to the northward IMF. Keeping in mind that the away sector IMF influence is still evident, a negative potential cell associated with "dawnside" upward field-aligned current is initially more evident than the positive potential. The positive cell is most likely present but superimposed on a region of previously strong negative potential in the vicinity of 80° magnetic latitude and 1700 MLT. Between 1050 and 1100 UT the convection reversal is completed and a strong dusk-to-dawn electric field is evident. At lower latitudes on the nightside the remnants of the dawn-to-dusk IMF southward electric field (and hence convection) are still evident. Elements of that convection existed through at least 1230 UT.

Ahn et al. (1988) have also studied the 23-24 July 1983 interval. They applied the KRM procedure and provided electrodynamic maps averaged over 15 minute intervals. Their averaged electric potential map for 1055-1110 UT (shown in Fig. 7.15) portrays the same electrodynamics structures apparent in the AMIE results.

Crooker (1979) and Reiff and Burch, (1985) predicted that under some circumstances ($|B_y| \geq |B_z|$) the IMF could merge with both closed dayside magnetic field lines and open tail lines simultaneously. This condition is apparently met throughout the bulk of the afternoon hours on 23 July. The IMF B_y condition leads to an inflation of the evening (positive) potential cell and the deflation and displacement of the morning (negative) potential cell. Crooker (1979) predicted that the combination of northward IMF and a strong B_y would produce nearly circular flow (called a lobe cell by Burch and Reiff, 1985) in the polar cap. The sense of flow should be counter clockwise for strongly negative

IMF B_y . The polar cap flow begins a transition to that flow regime at approximately 1300 UT.

Crooker (1988) proposed a new set of model convection patterns to account for slow variation in the B_y and B_z components of the solar wind. Two convection cells driven by merging with closed geomagnetic field lines distend and inflate depending on the relative magnitudes of B_y and B_z . AMIE electric potential patterns derived for the period 1300-1900 UT show basic features consistent with the Crooker model. In Fig. 7.16 we present a comparison of the Crooker model and our results. A slow turning from positive to negative B_z while B_y becomes more negative inflates the positive potential cell and draws out the negative potential across the noon sector. A slow steady growth and rotation of the negative cell eventually produces nearly symmetric convection in the sense normally associated with southward IMF. The electric potential pattern at 1900 UT is an example of such convection. Although IMF data are not available at 1900 UT we believe the ionosphere is still under the influence of slightly positive B_z at that time. Apparently the IMF B_y component dominates the convection regime. This situation exists until approximately 1920 UT when the nightside electric field strength increases signalling a return to southward IMF conditions. As pointed out by Crooker (1988) the model convection patterns are consistent with the recently published empirical models of Heppner and Maynard (1987). Our patterns for the period 1300-1900 UT seem to agree with the Heppner and Maynard distorted two cell convection, although in this case we do not observe the intensity of convection suggested by their results.

IV. JOULE HEATING

As a final comment on this analysis we present a comparison of the time series of Joule heating for 19 September 1984 and 23-24 July 1983. The

values of globally integrated Joule heating shown in Fig. 7.17 are similar for periods of northward IMF (with large B_y component) on 23 July 1983 and periods of southward IMF during the latter half of 19 September 1984. Joule heating rates during these periods is on the order of a few times 10^{11} Watts.

Maps of Joule heating for a single time during each of these periods is shown in Fig. 7.18. Although the globally integrated Joule heating values are similar, the locations of Joule heating are quite different. High-latitude dayside heating corresponds to northward IMF while southward IMF tends to produce extended regions of Joule heating in the lower latitude nightside. The focus of Joule heating has important implications for thermospheric dynamics. High resolution mapping procedures such as AMIE offer new methods of properly accounting for the location and magnitude of Joule heating (Crowley et al., 1989).

V. SUMMARY

We have selected a few significant results from our investigation of high-latitude electrodynamics for 19 September 1984 and 23-24 July 1983. We demonstrate that the AMIE procedure has the temporal and spatial resolution for investigating a wide variety of ionosphere-magnetosphere-solar wind linkages. To our knowledge no previous investigations have shown the temporal development of the large scale convection reversals demonstrated in the 23-24 July northward IMF cases.

FIGURE CAPTIONS FOR CHAPTER 7

Figure 7.1. Geophysical and Derived parameters for 19 September 1984. The top five curves, IMF B_y , IMF B_z , (GSM coordinates) HPI, DST and AE are independent indicators of the electrodynamic state of the high-latitude ionosphere. The bottom four curves are AMIE derived values. (From Knipp et al., 1989).

Figure 7.2. The AU and AL indices for 19 September 1984.

Figure 7.3. Comparison of the AMIE derived potential difference time series with the statistical values derived from the empirical model of Foster et al. (1986).

Figure 7.4. Fitted electrodynamic patterns for 0950 UT on 19 September 1984. Each plot maps a region from the pole to 50° magnetic north in 10° latitude increments. Top panel (left) Pedersen conductance with contour intervals of 2 S. Top panel (right) electric potential with contour intervals of 10 kV. The total potential difference is written in the upper left corner of the plot. Middle panel (left) Equivalent current with contour intervals of 50 kA. Middle panel (right) Field-aligned current. The contours begin at $\pm 0.5 \mu\text{A}/\text{m}^2$ and are incremented thereafter by $\pm .25 \mu\text{A}/\text{m}^2$. Solid contours represent downward current; dashed contours represent upward current. Bottom panel (left) Horizontal current vectors; the length of the line in the lower right corner of the plot represents 1 A/m. Bottom panel (right) Height-Integrated Joule heating taking into account the effect of electric field uncertainties. The contour interval is $5 \text{ m W}/\text{m}^2$ and the areal integrals poleward of 50° magnetic latitude are given at the upper left.

Figure 7.5. Same as for Fig. 7.4 except time is 1050 UT.

Figure 7.6. Same as for Fig. 7.4 except time is 1150 UT.

Figure 7.7. Same as for Fig. 7.4 except time is 1430 UT.

Figure 7.8. Same as for Fig. 7.4 except time is 1530 UT.

Figure 7.9. Same as for Fig. 7.4 except time is 1630 UT.

Figure 7.10. Geomagnetic indices and AMIE derived parameters for 23-24 July 1983.

Figure 7.11. AMIE electric potential plots for 0830-1100 UT on 23 July 1983 in half hour increments.

Figure 7.12. AMIE electric potential plots for 1130-1400 UT on 23 July 1983 in half hour increments.

Figure 7.13. AMIE electric potential plots for 1430-1700 UT on 23 July 1983 in half hour increments.

Figure 7.14. AMIE electric potential plots for 1730-2000 UT on 23 July 1983 in half hour increments.

Figure 7.15. KRM results (from Ahn et al., 1988) using data averaged over the fifteen minute period 1055-1110 UT.

Figure 7.16. AMIE electric potential plots for 1030-1100 UT in ten minute increments.

Figure 7.17. Comparison of the convection reversal model from Crooker (1988) with AMIE results for times between 1230 and 1900 UT on 23 July 1988.

Figure 7.18. Comparison of time series globally integrated Joule heating rates for 19 September 1984 and 23-24 July 1983.

Figure 7.19. Comparison of Joule heating patterns produced under the influence of varying IMF conditions.

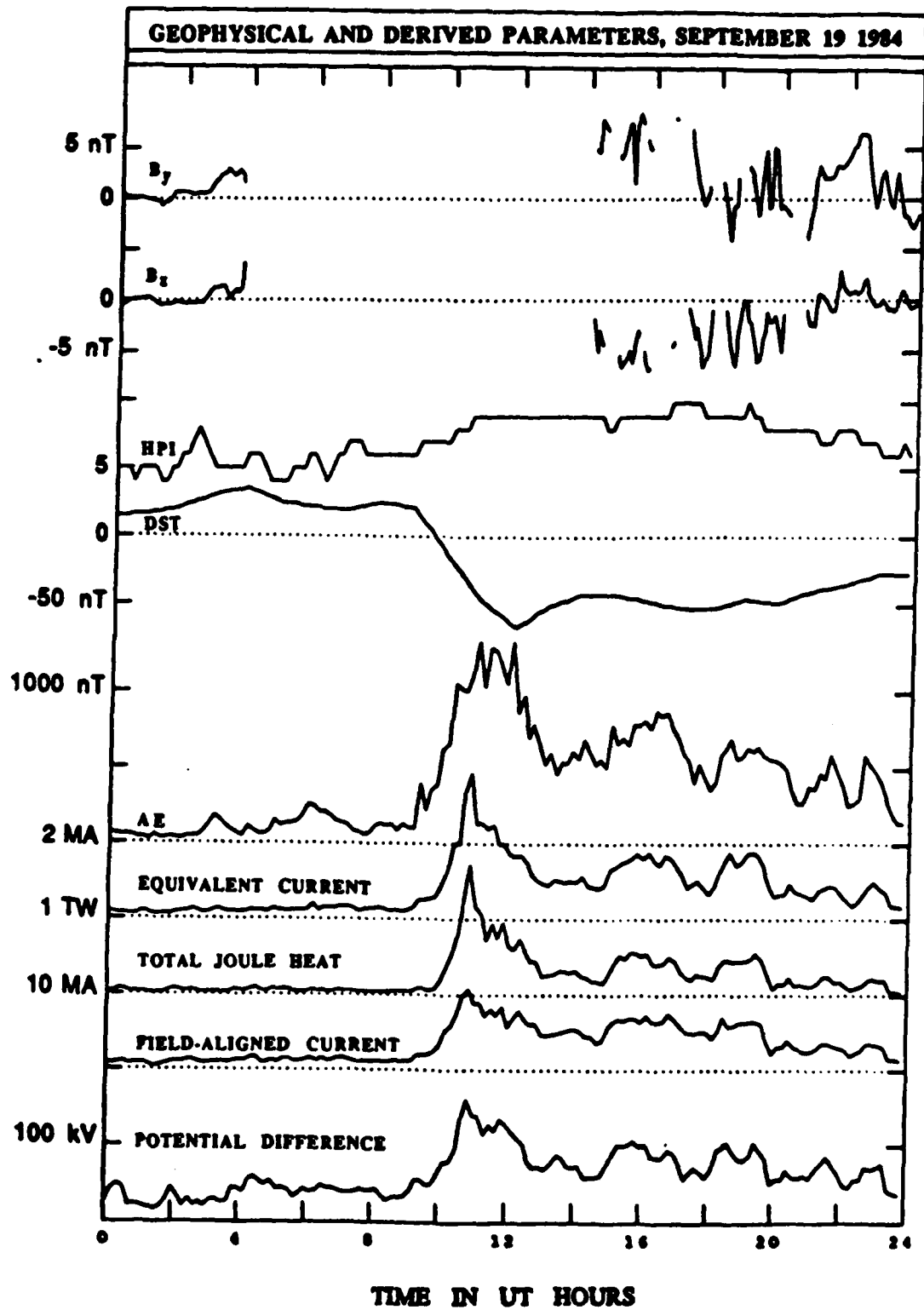


Figure 7.1

AL/AU FOR SEPTEMBER 19 1984

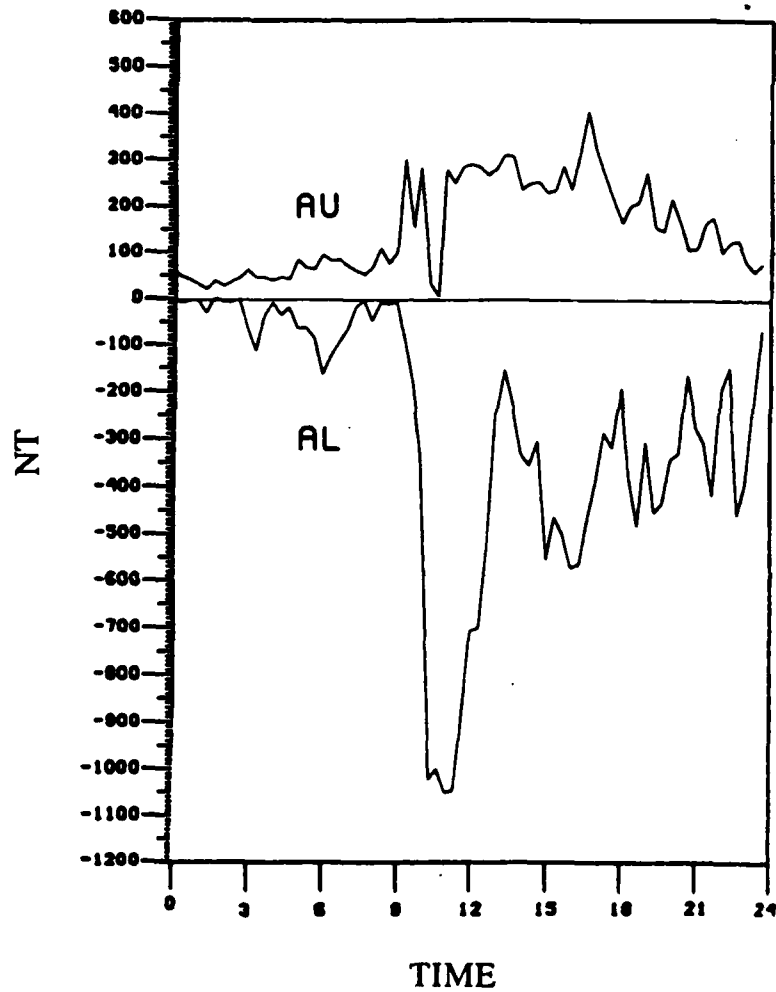


Figure 7.2

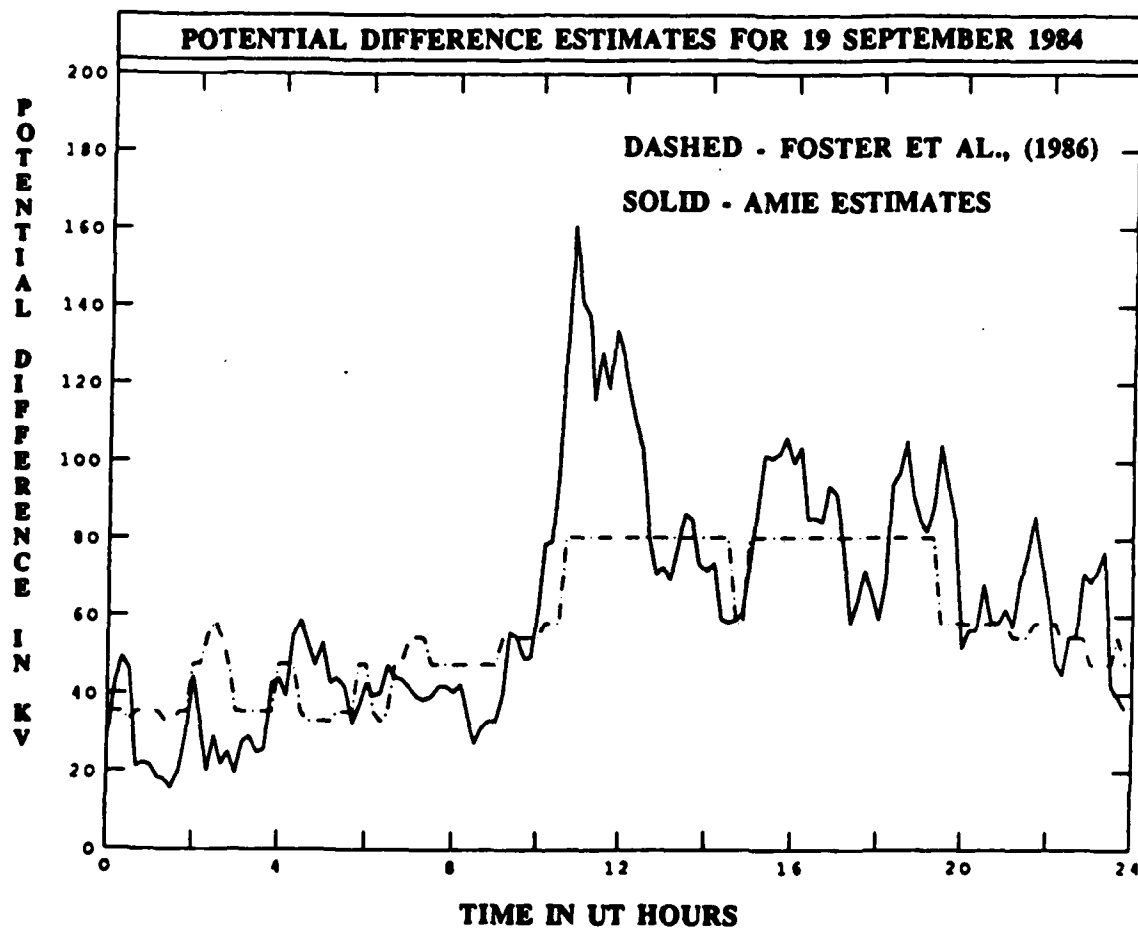


Figure 7.3

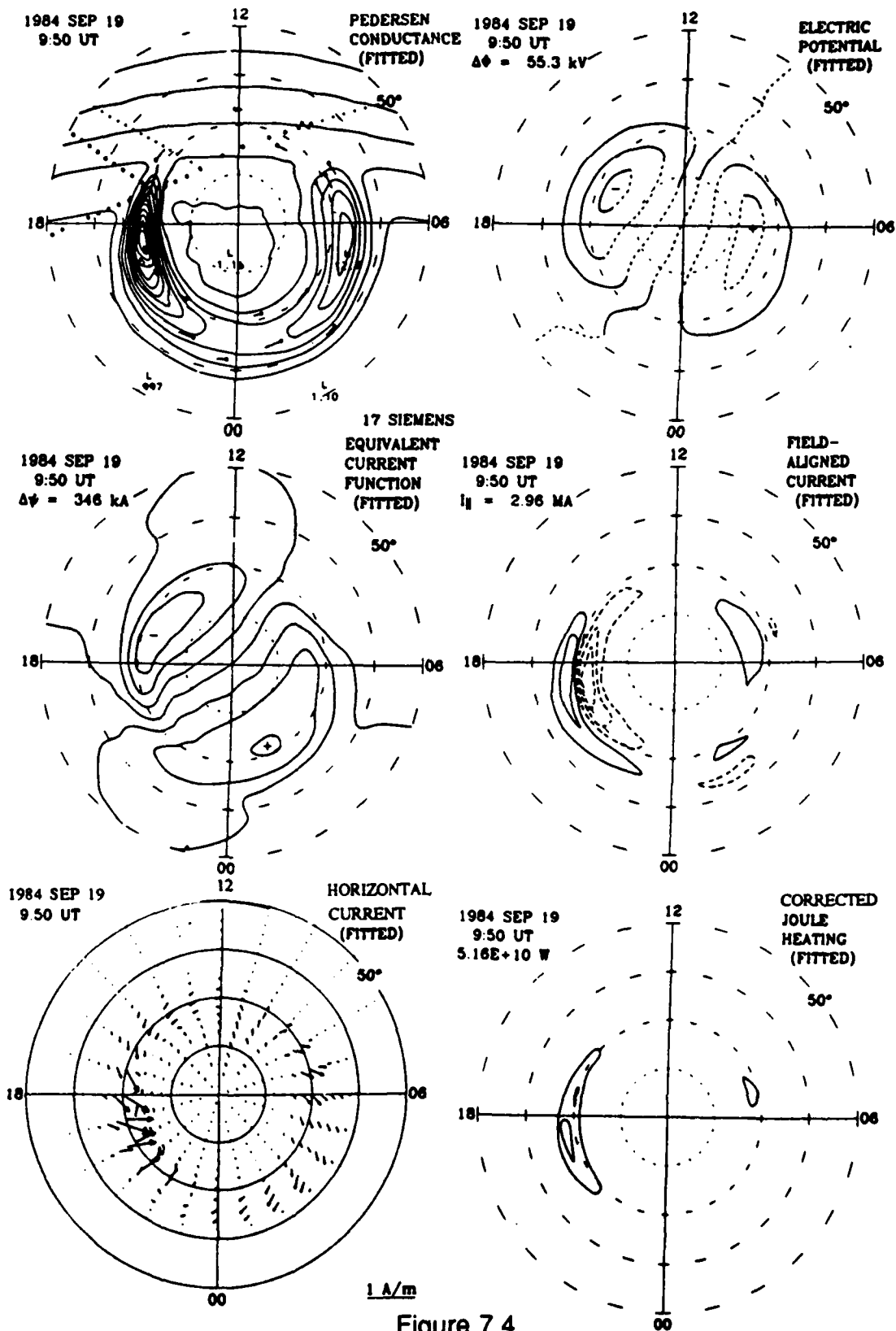


Figure 7.4

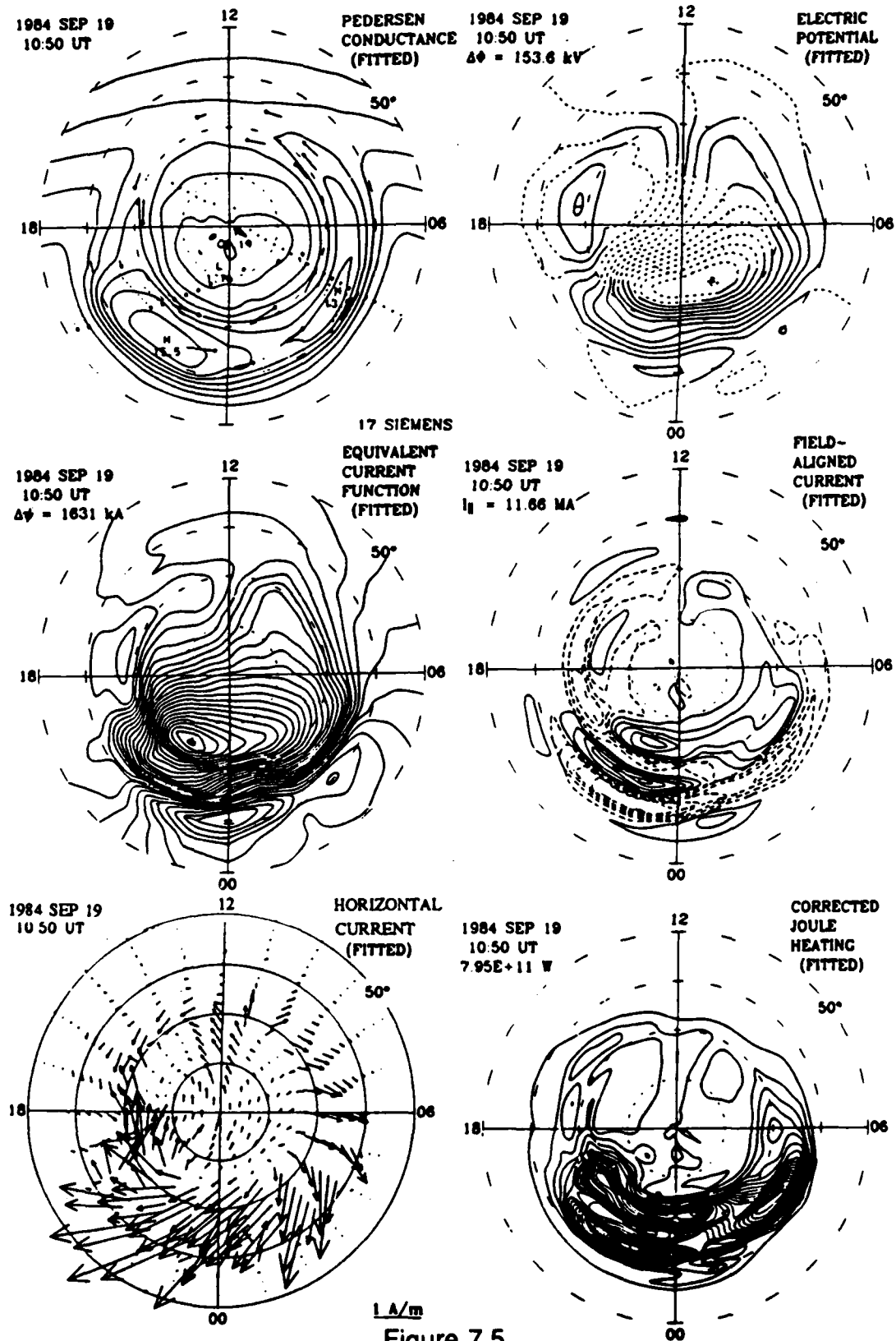


Figure 7.5

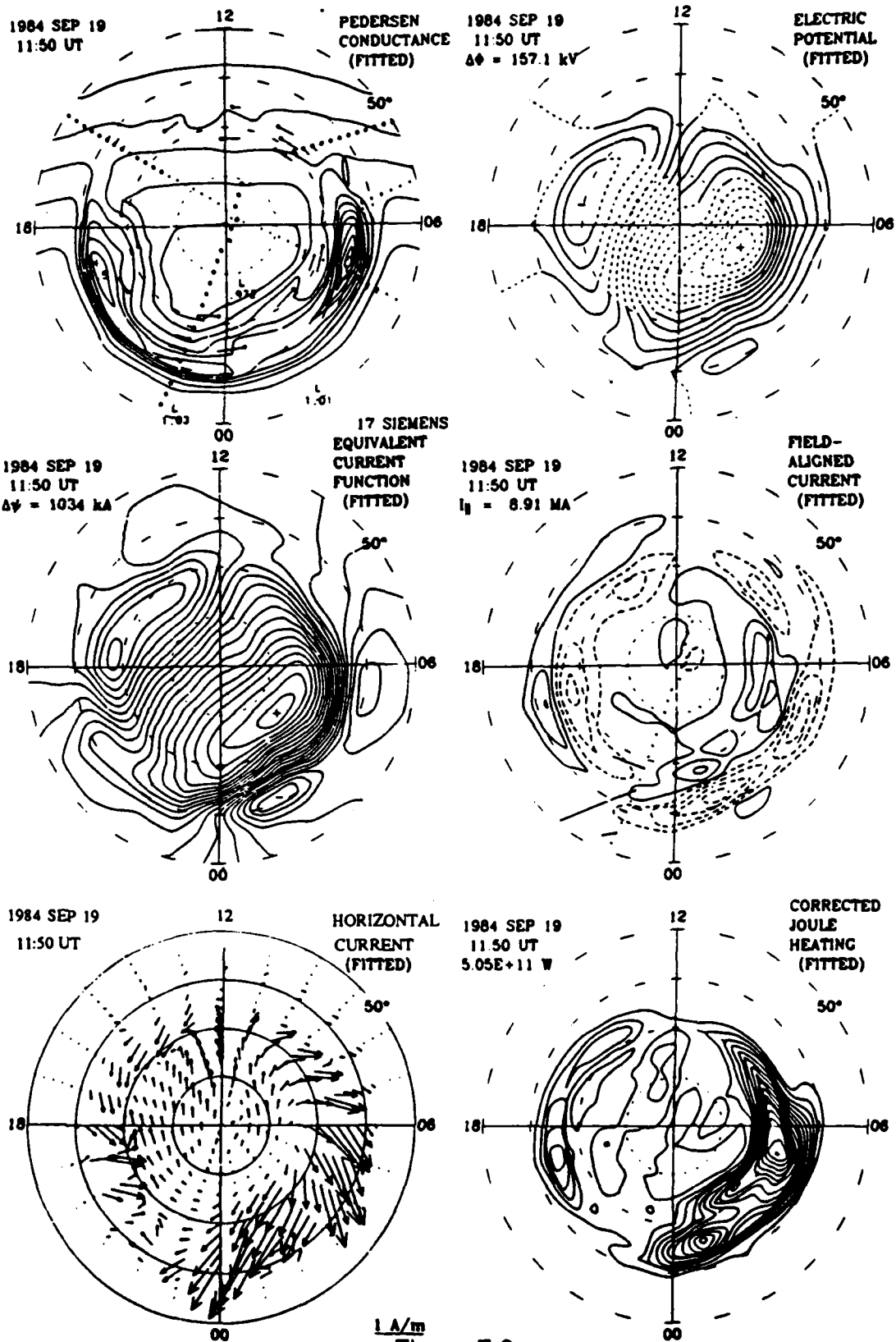


Figure 7.6

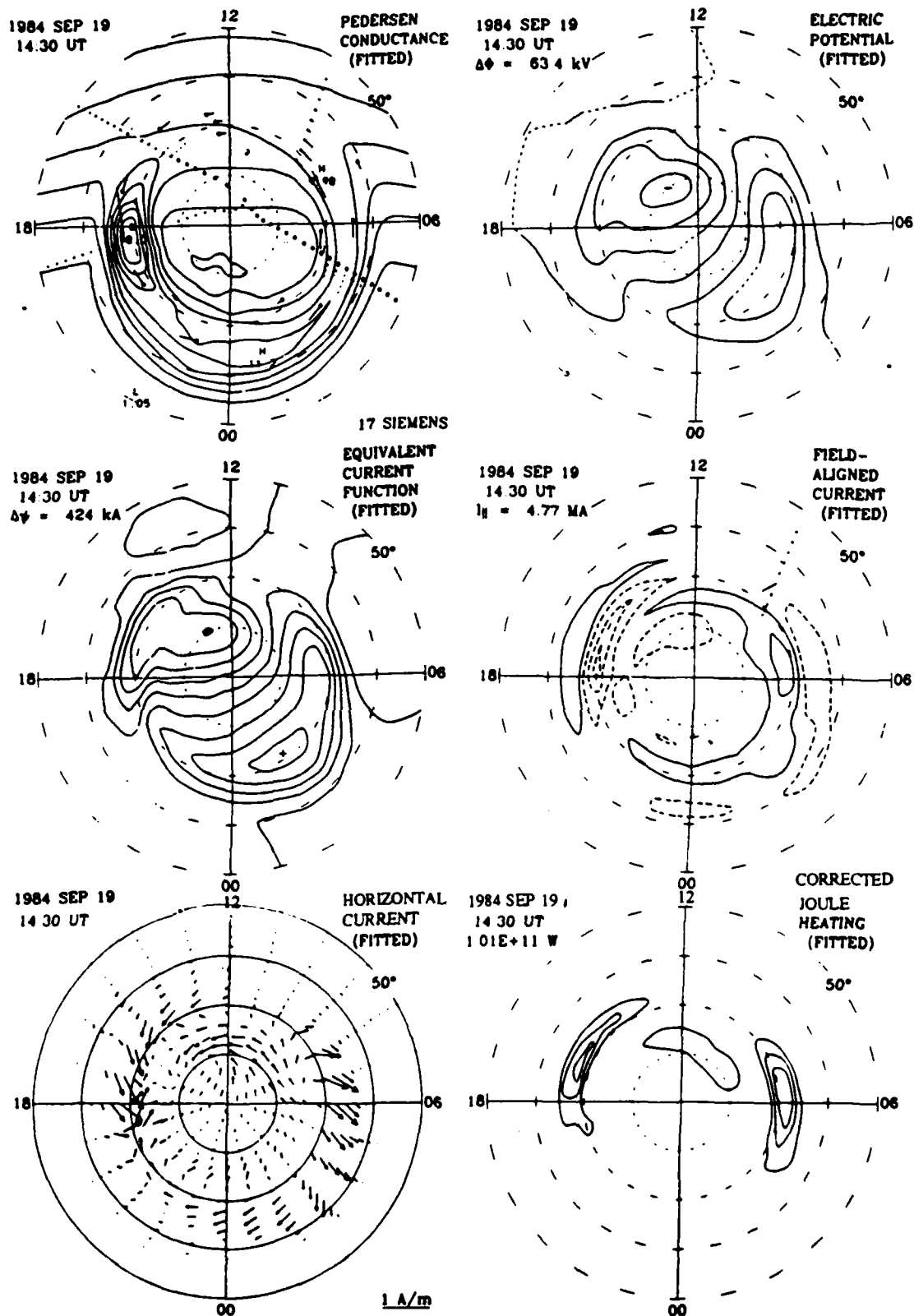


Figure 7.7

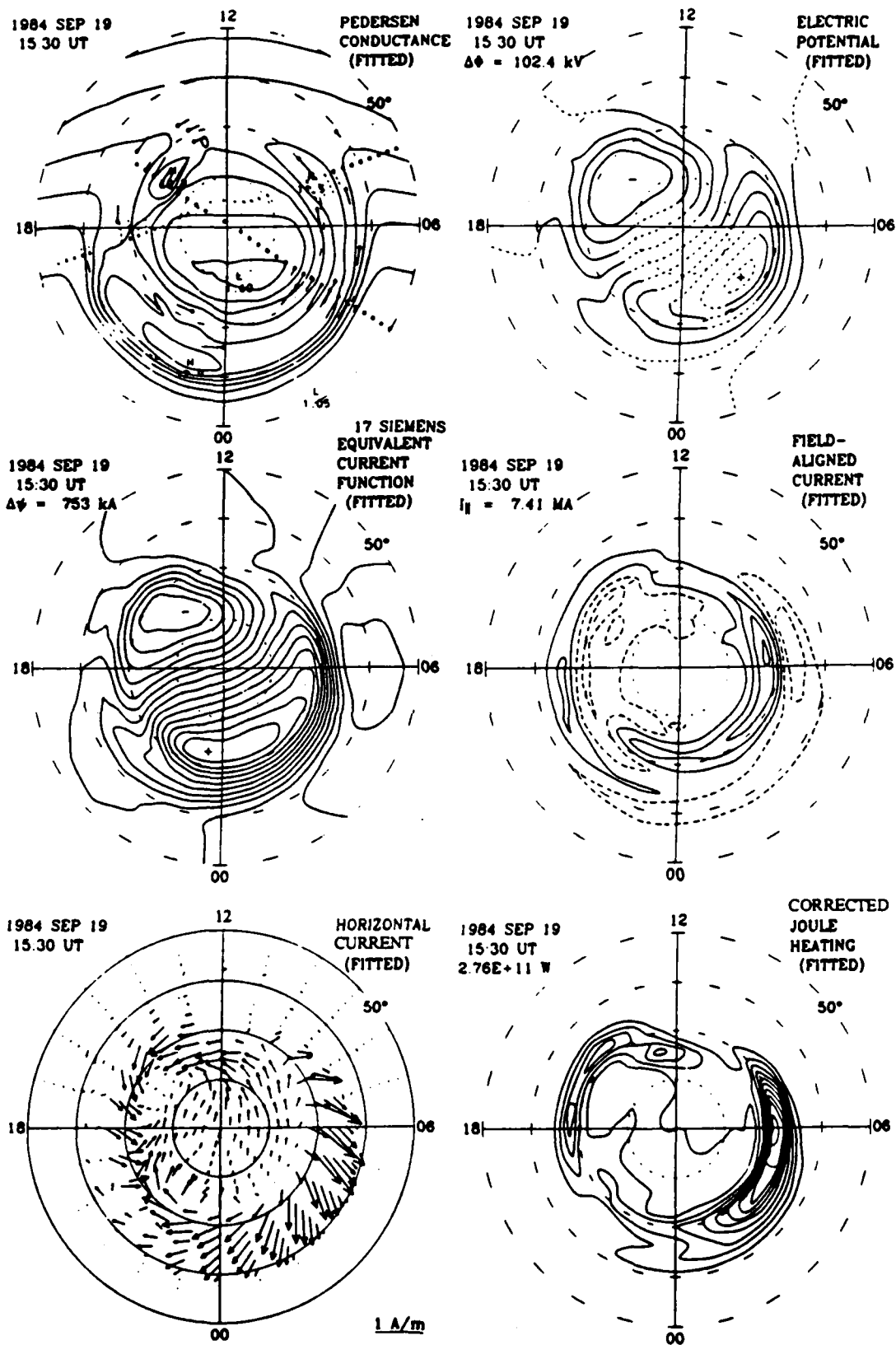


Figure 7.8

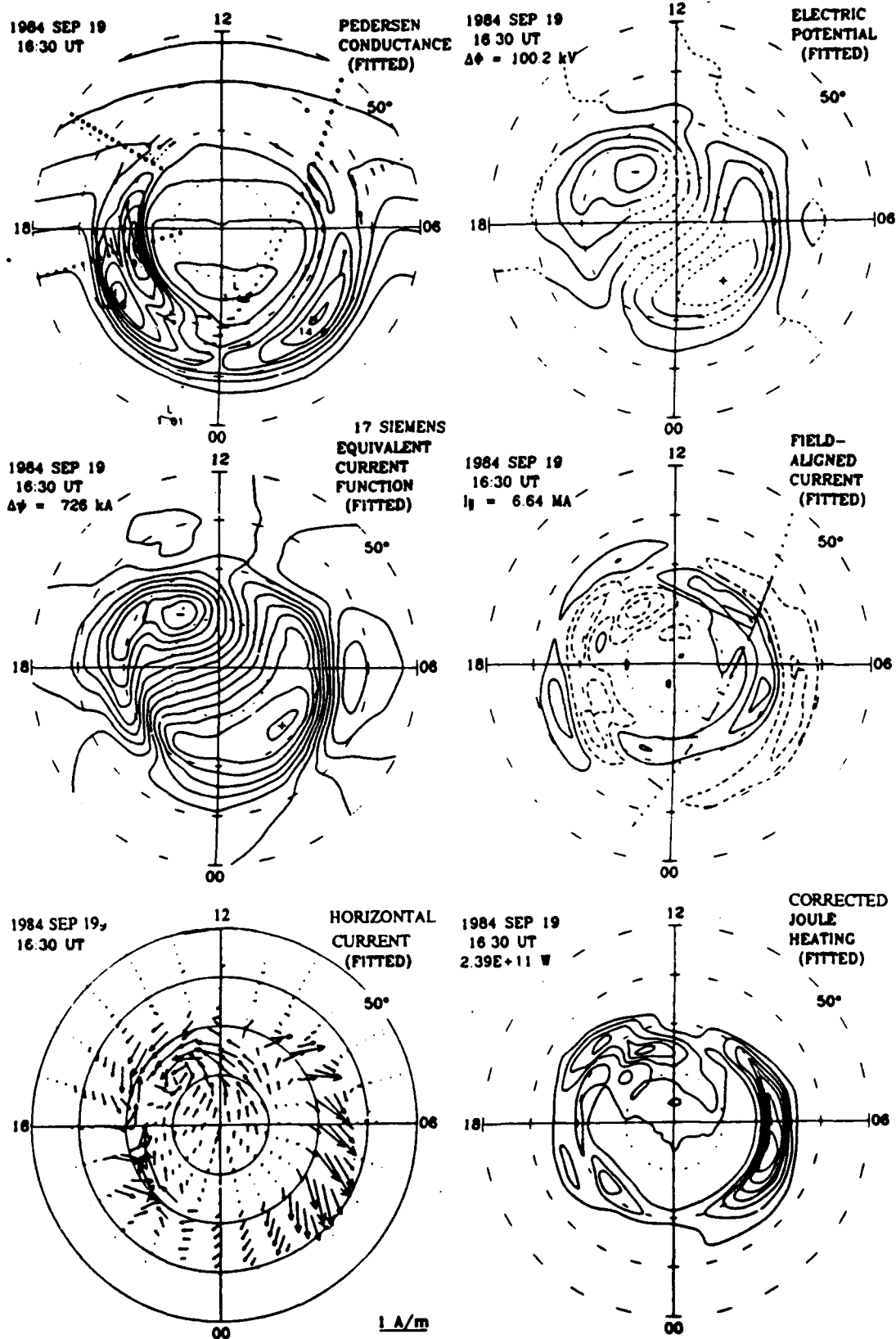


Figure 7.9

23-24 JULY 1983

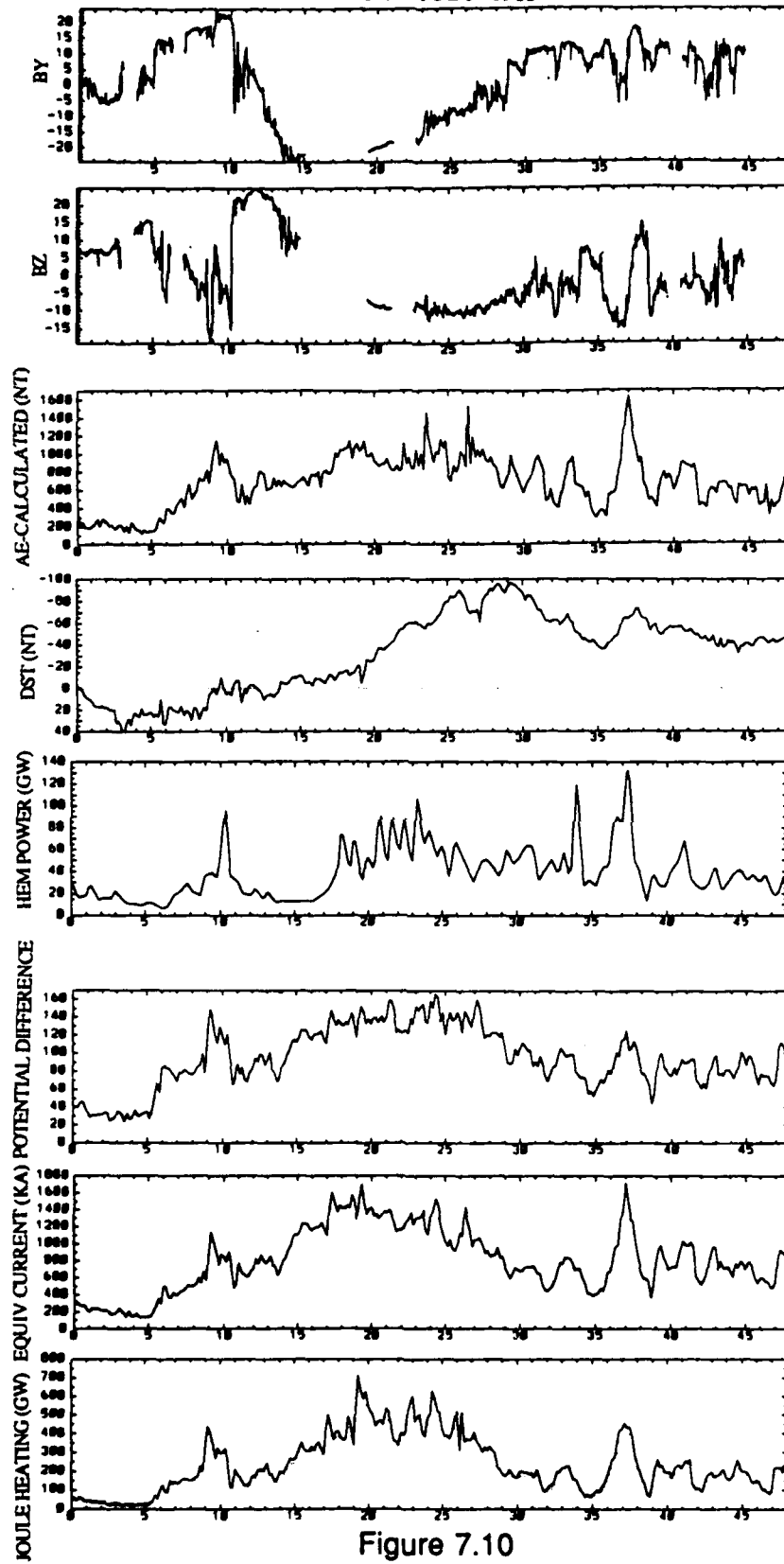


Figure 7.10

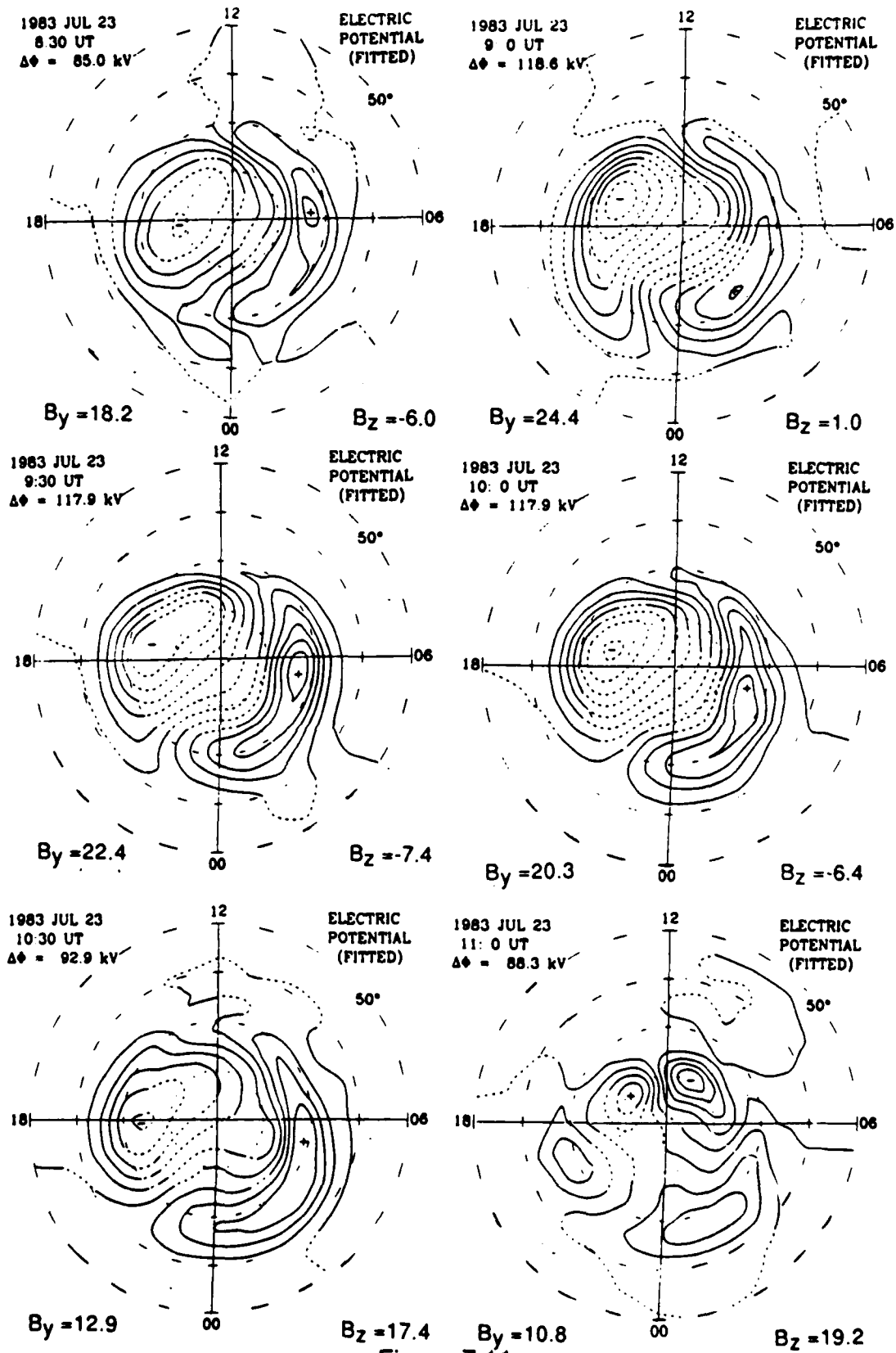


Figure 7.11

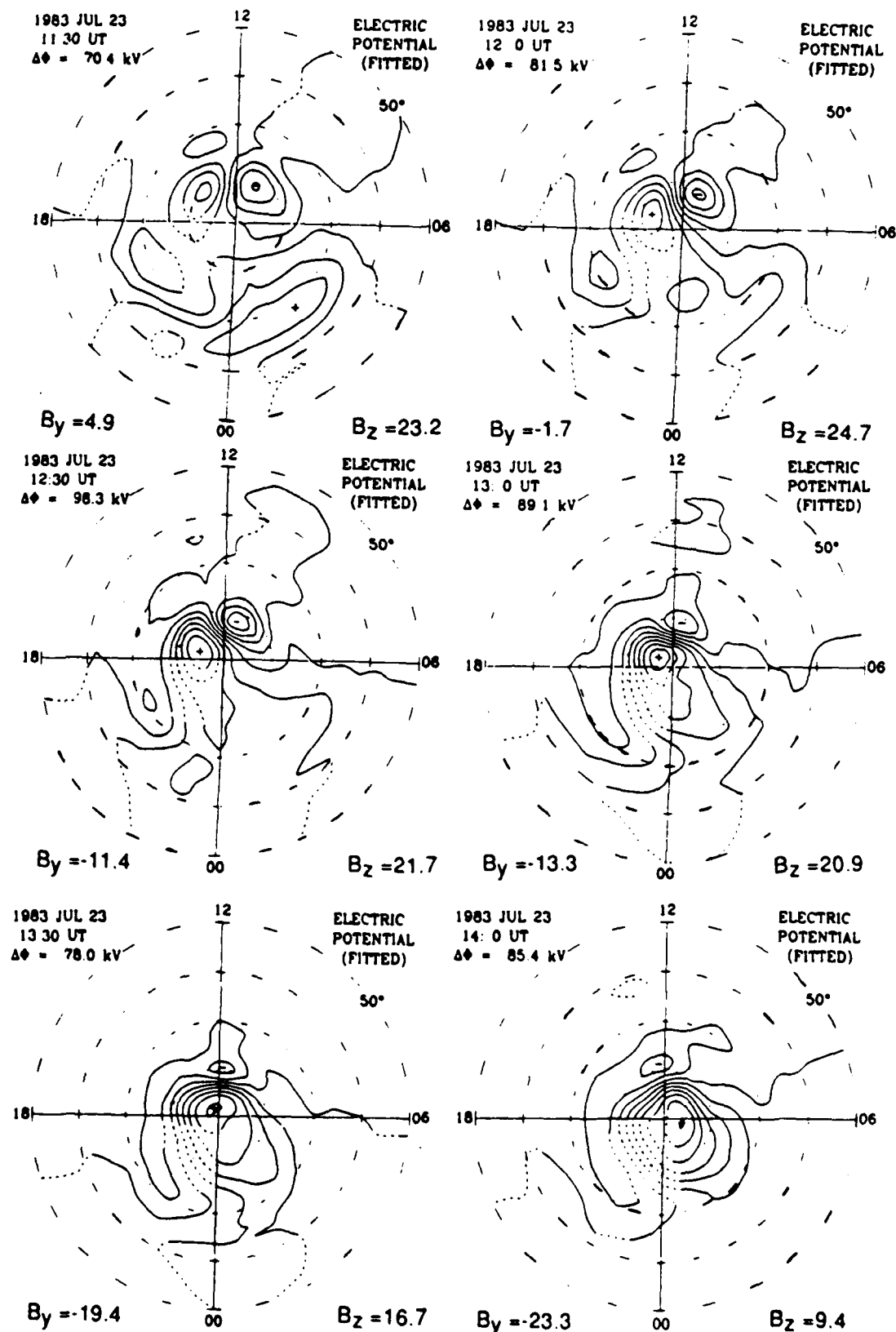


Figure 7.12

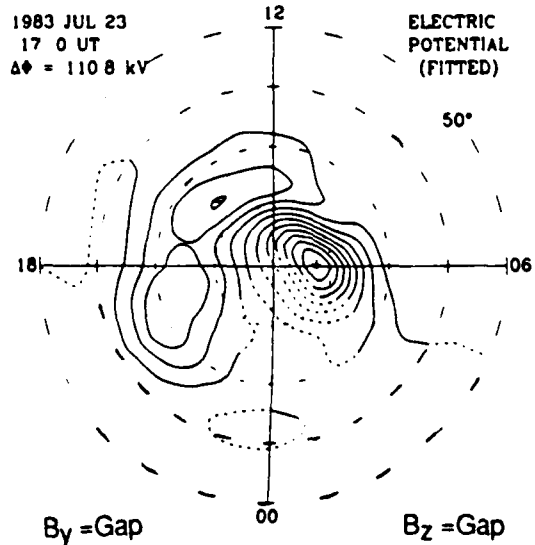
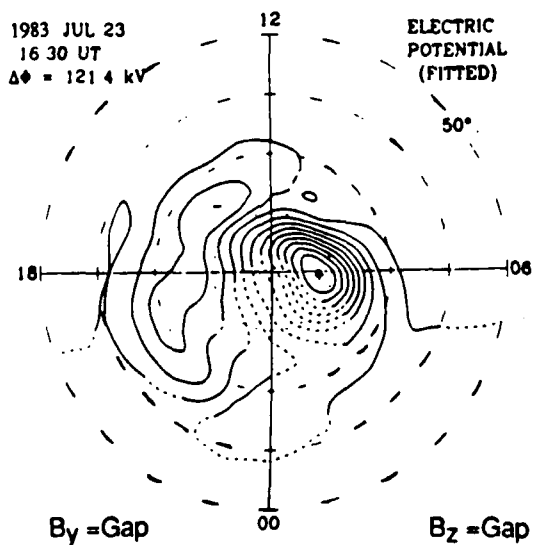
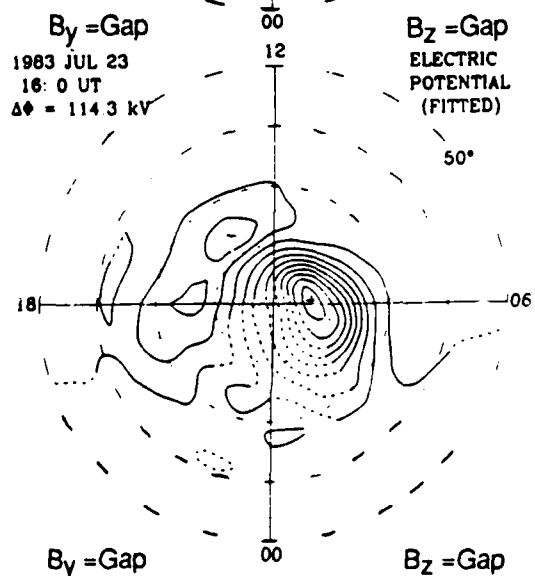
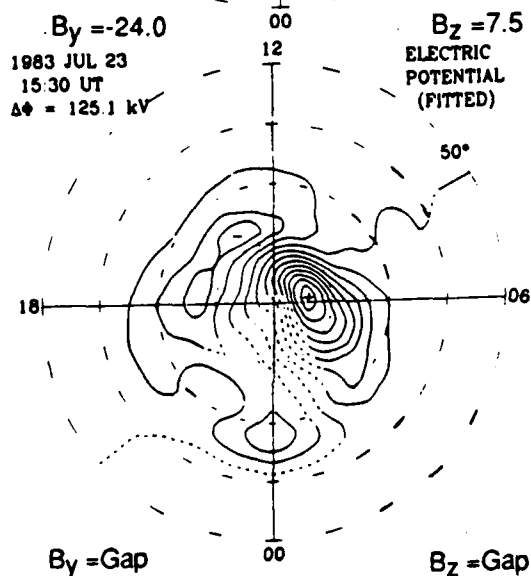
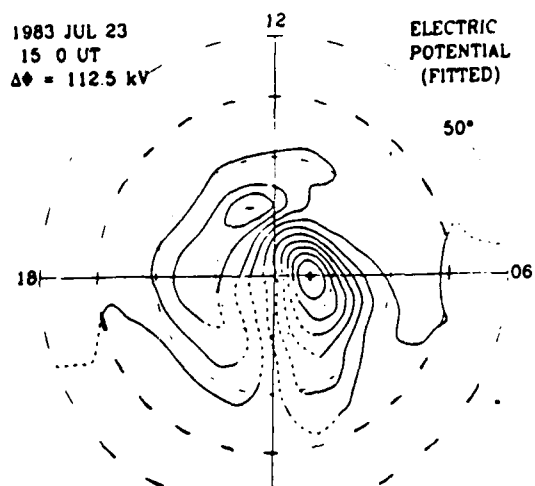
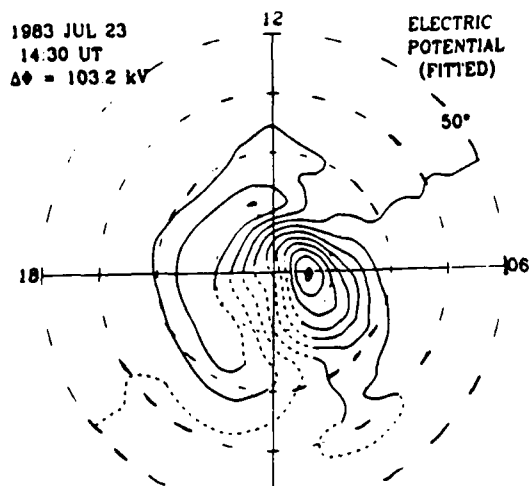


Figure 7.13

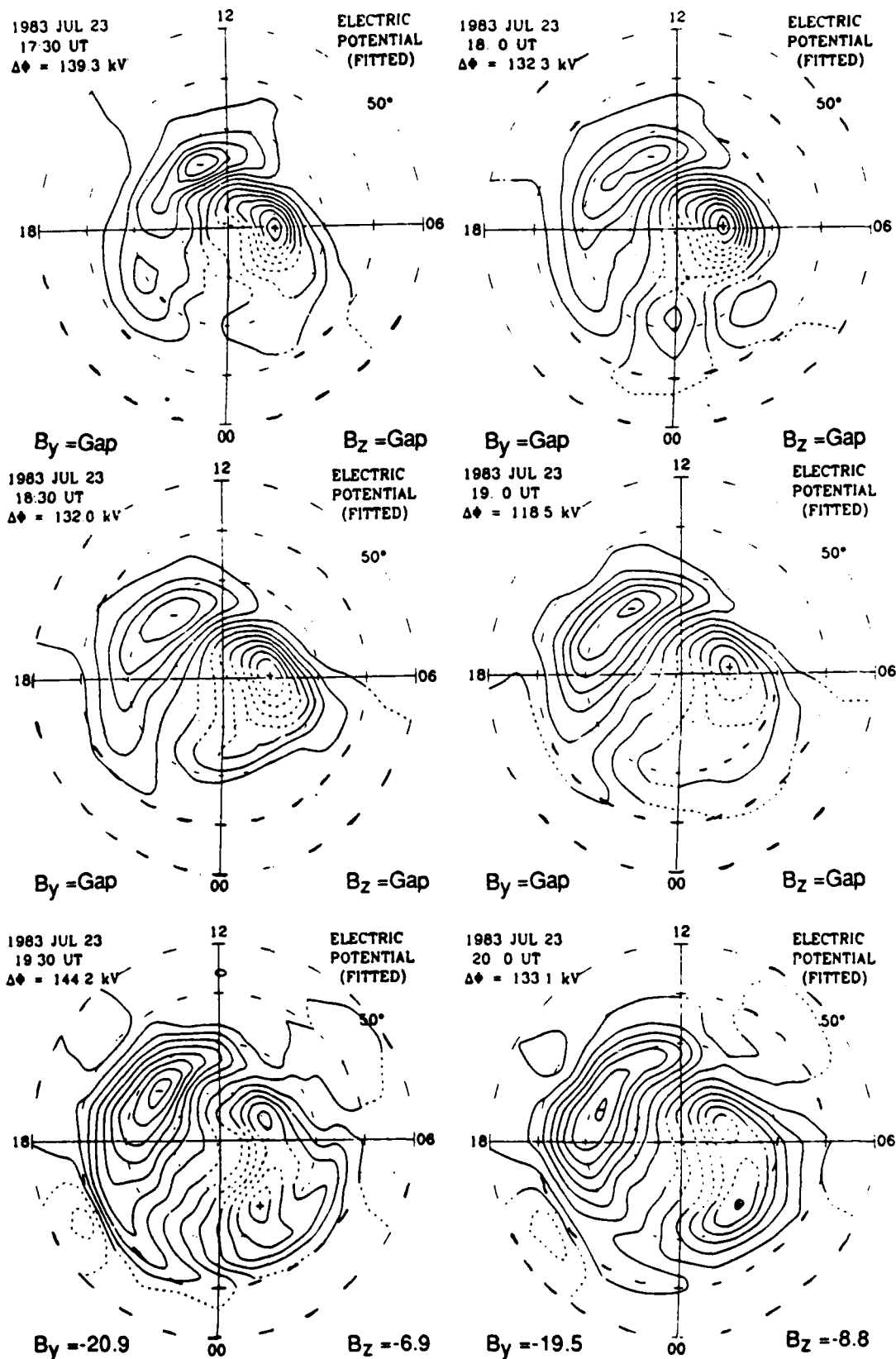


Figure 7.14

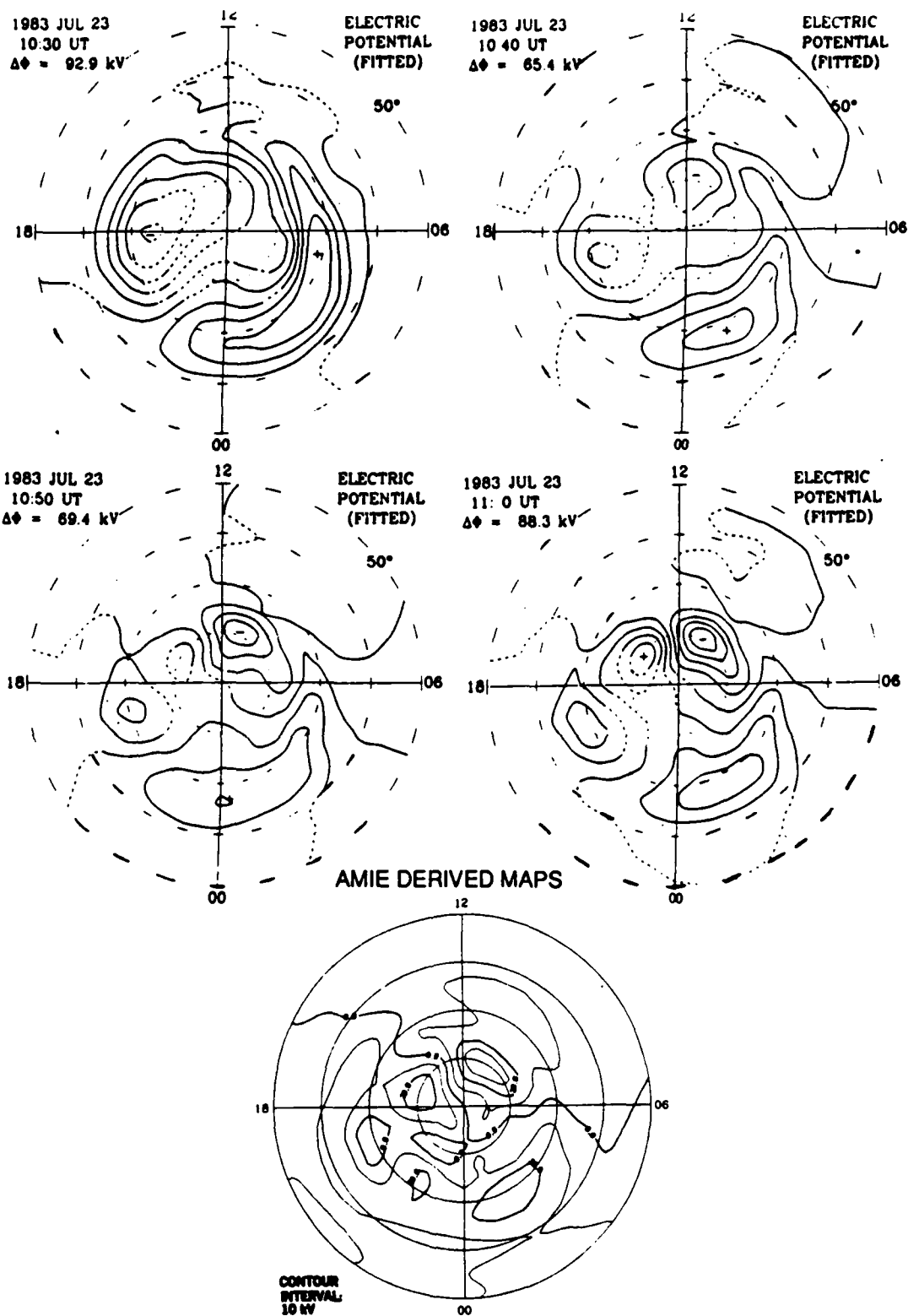


Figure 7.15

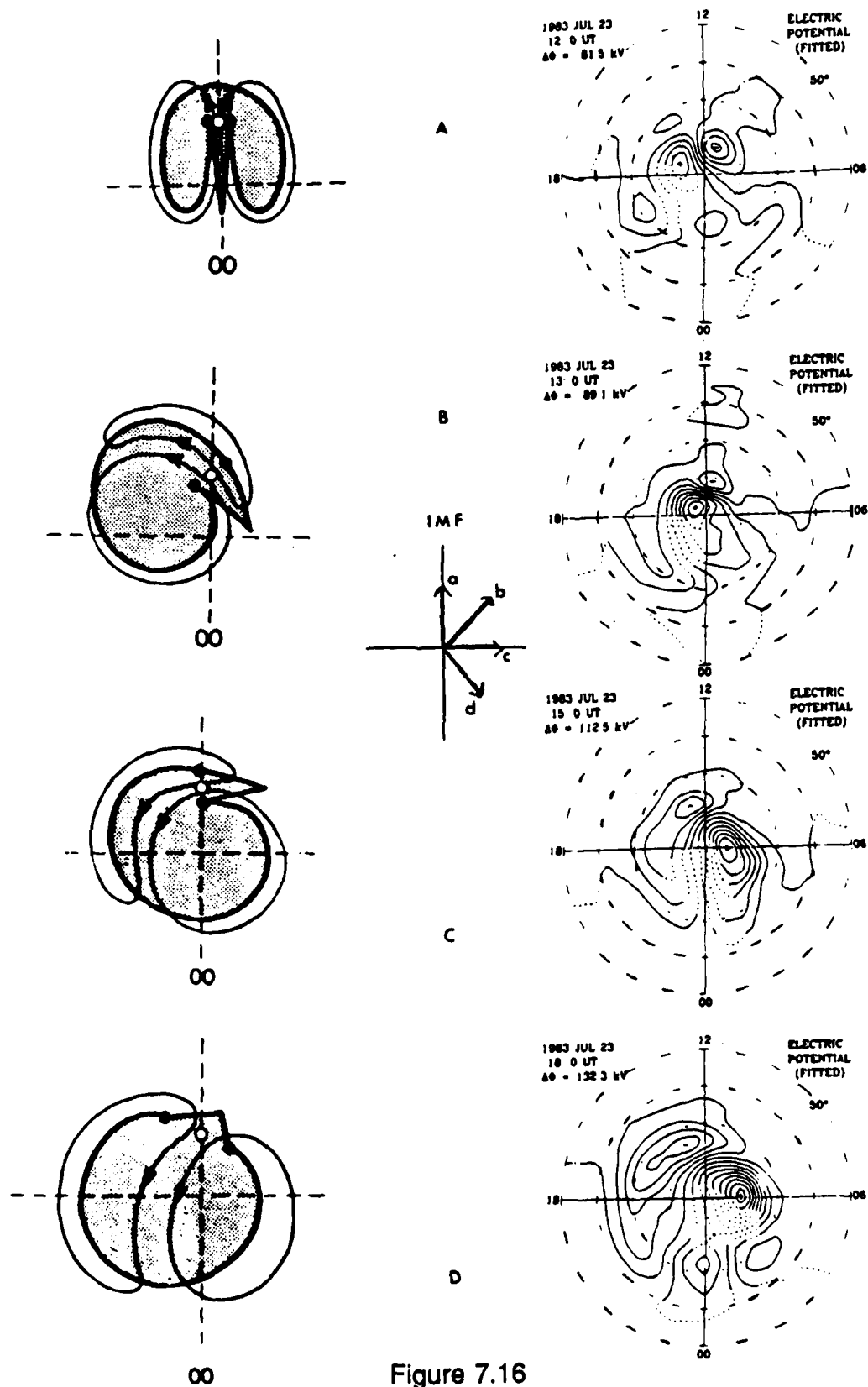
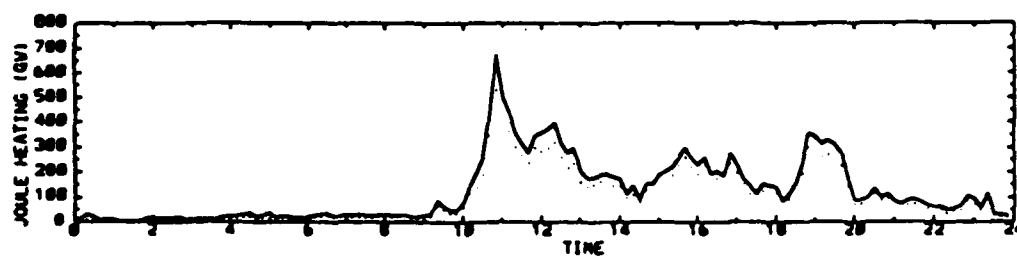


Figure 7.16

19 SEPTEMBER 1984



23-24 JULY 1983

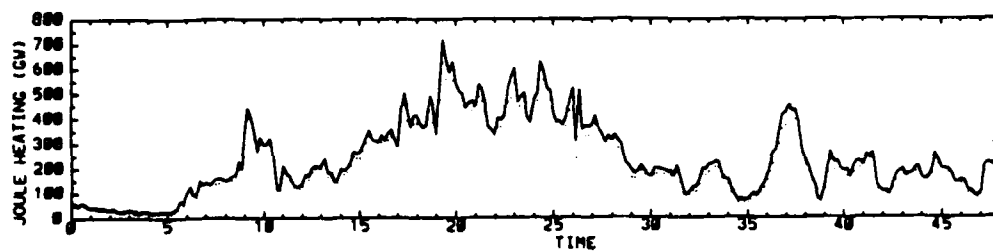


Figure 7.17

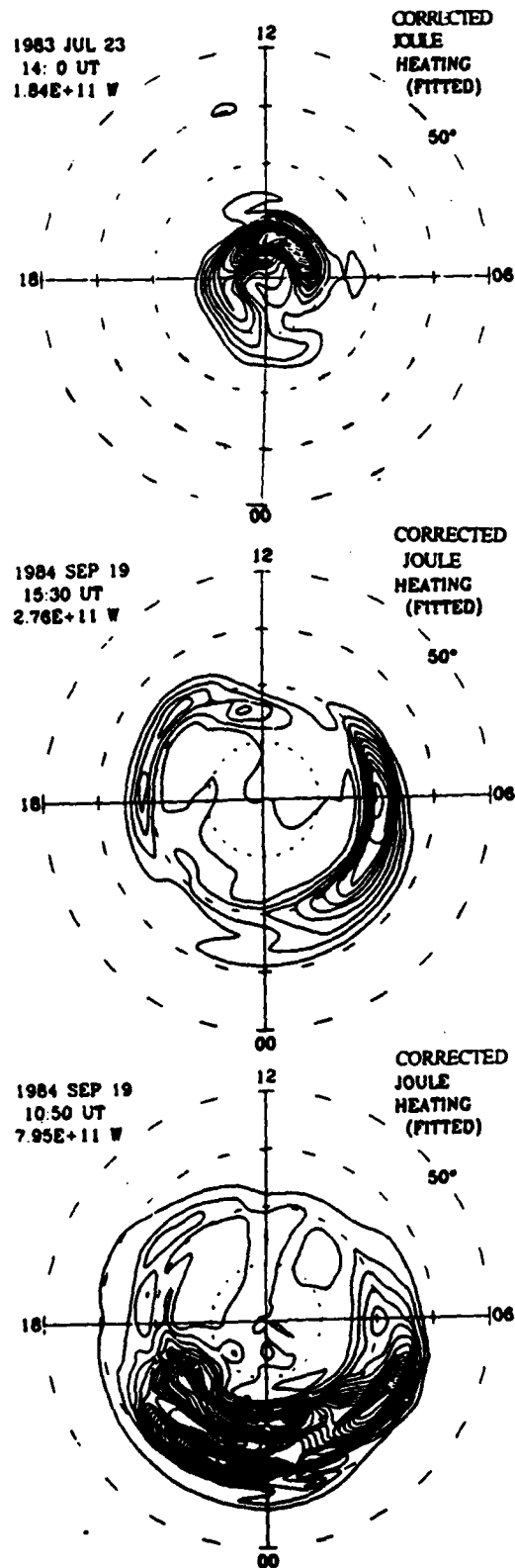


Figure 7.18

CHAPTER 8

SUMMARY

I. REVIEW

In this work we have given a short description of the AMIE procedure with special emphasis on the conductance data assimilation. We provided background chapters and appendices which were designed to familiarize the reader with important physical relations and assumptions necessary for proper assimilation of four new data sources (1) satellite particle precipitation data, (2) satellite X-ray image data, (3) satellite magnetometer data and (4) the vertical component of ground magnetic perturbations.

In chapter 4 we demonstrated the utility of image data which provide snap shots of a large fraction of the auroral oval. In that chapter we also discussed preliminary results from estimating the error propagated into the electric field estimate from errors in the conductance estimate. We have successfully integrated satellite conductance data into the AMIE procedure and shown that the assimilation improves the fit of the estimated electric field to the data. Figure 4.9 illustrates the evolution of the conductance estimate as new data sources are included in the procedure. Figures 4.12 and 4.13 show the temporal and spatial variation of the oval as geomagnetic disturbances develop and decay.

The desire to make the electric field estimates more reliable also motivated the assimilation of new magnetometer data sources as discussed in chapter 5. No simple tests exist to prove that these data always give more reliable estimates, but we have shown representative cases (Figures 6.3 and 6.4) that indicate reductions in the electric field uncertainty. Further

improvements may be achieved by filtering the satellite magnetometer data and correcting for Dst in the vertical ground magnetic perturbations.

Our geophysical results shed light on the development and decay of a DP 1 current system during the first disturbance on 19 September 1984. The derived AMIE current patterns provide a plausible explanation for the previously unexplained decrease in the AU index during the disturbance. We assert that the westward electrojet penetrated deeply enough into the evening sector to generate an "inverted" or negative horizontal bay in the AU index (as suggested by Akasofu, 1965). The electric potential patterns associated with these current patterns show a strong concentration of electric field in the pre-midnight region (in good agreement with the results of Moses et al. (1989)). We also find that the disturbances occurring later in the day develop differently than the first substorm. We conclude that the latter disturbances were triggered by a type of magnetospheric input different from that initiating the first disturbance.

In the 23-24 July 1983 case we focused in the relative impacts of IMF B_y and B_z . We showed the temporal development of a rapid high-latitude convection reversal. Our patterns imply strong magnetic merging in regions poleward of the cusp, as suggested by Dungey (1961), Russell (1972) and Maezawa (1976). We also show that the IMF east-west component can dominate the merging process. Our results are in excellent agreement with the theoretical results of Crooker (1988) and Reiff and Burch (1985), the observational results of Zanetti and Potemra (1986) and the empirical results of Heppner and Maynard (1987).

We also briefly compared modes Joule heating arising from different configurations of the IMF. Although we give only a sample of the AMIE derived Joule heating patterns, the variations in these patterns are sufficient to suggest

that different IMF configurations can lead to dramatically different modes of coupling, energetic and dynamics of atmospheric and near-earth regions.

II. FUTURE WORK

In future work we plan to pursue a more rigorous approach to estimating the conductance error propagated into the electric field estimates. We must also learn whether a more select group of magnetometer stations will allow us to better incorporate the vertical component of ground magnetic perturbations.

From a geophysical stand point further study of Joule heating and field-aligned current patterns are likely to yield significant information about ionosphere-magnetosphere coupling. The spatial dependence of Joule heating on electric fields and conductance is also an important topic of investigation.

In terms of new data sources the addition of satellite ion drift measurements will provide a more direct measure of electric fields over a significant region of the ionosphere. This project is slated to begin within the next few months.

Improvements to the estimation procedure itself may include improving the model electric field and conductance distribution. It may also be possible to include a linkage between the field-aligned currents and the conductance patterns as suggested by Marklund et al. (1988).

We plan to make our results available to other researchers wishing to compare their theories and observations with an objective high-latitude analysis. We will provide AMIE fields and distributions for 19 September 1984 and 23-24 July 1983 (derived at ten minute intervals) to the National Center for Atmospheric Research Incoherent Scatter Radar data base.

The temporal and spatial resolution available from the AMIE procedure make it a significant tool for (1) analyzing events such as individual substorms, (2) providing coherency in coordinated campaign results by deriving electrodynamic patterns consistent with all available data and (3) answering questions regarding the mix of instrumentation necessary for diagnosis of geophysical events.

APPENDIX I

FITTING TECHNIQUES

Least squares fitting is a standard technique employed whenever there is reason to believe that observations are linearly related to some combination of dependent variables.

I. Standard Least Squares Estimation

The simplest approach is standard least squares (SLS) estimation. In SLS estimation the observations are linearly related to unknown quantities \mathbf{s} by the expression

$$\mathbf{z} = \mathbf{L}\mathbf{s} + \mathbf{v} \quad 1.1$$

where \mathbf{z} is a column vector of J observations, \mathbf{s} is a column vector of I coefficients, \mathbf{L} is a $J \times I$ matrix of basis functions and \mathbf{v} is a column vector of J errors. In making an estimate of \mathbf{s} we want to choose the set of coefficients $\hat{\mathbf{s}}$ that minimizes the difference between the estimated value of the function $\mathbf{L}\hat{\mathbf{s}}$ and the observations. The best fit of the coefficients to the data occurs when

$$Q = (\mathbf{L}\hat{\mathbf{s}} - \mathbf{z})^T (\mathbf{L}\hat{\mathbf{s}} - \mathbf{z}) \rightarrow \min \quad 1.2$$

where the cost function, Q , is a scalar resulting from the inner product operation.

To minimize Q we set the derivative of Q with respect to $\hat{\mathbf{s}}$ equal to zero:

$$\frac{\partial Q}{\partial \hat{\mathbf{s}}} = \frac{\partial}{\partial \hat{\mathbf{s}}} (\hat{\mathbf{s}}^T \mathbf{L}^T \mathbf{L} \hat{\mathbf{s}} - \hat{\mathbf{s}}^T \mathbf{L}^T \mathbf{z} - \mathbf{z}^T \mathbf{L} \hat{\mathbf{s}} + \mathbf{z}^T \mathbf{z}) = 0 \quad 1.3$$

Note that the matrix multiplication inside the parenthesis produces scalar quantities. Since a scalar quantity is equal to its transpose we may write $\hat{\mathbf{s}}^T \mathbf{L}^T \mathbf{z} = \mathbf{z}^T \mathbf{L} \hat{\mathbf{s}}$. Therefore

$$\frac{\partial Q}{\partial \hat{\mathbf{s}}} = 2 \mathbf{L}^T \mathbf{L} \hat{\mathbf{s}} - 2 \mathbf{L}^T \mathbf{z} = 0 \quad 1.4$$

$$\Rightarrow \hat{\mathbf{s}} = (\mathbf{L}^T \mathbf{L})^{-1} \mathbf{L}^T \mathbf{z} \quad 1.5$$

Equation 1.5 is a standard textbook expression that can be used if all observations are believed to be equally valid and if the fit is to be applied to the observations exclusively (versus observations + prior data). Of course equation 1.5 is valid if and only if $(L^T L)^{-1}$ exists (i.e. has a non zero determinant).

II. Weighted Least Squares

In many real life situations not all observations in a data set are equally valid. It is often desirable to pass the relative validity of each datum to the fitting procedure, thus allowing the procedure to fit more closely to observations with low relative error. This constitutes a weighted least squares fit of the coefficients to the data. As an example of weighting, one may impose the inverse square of the expected error as a weight for any given datum. The best fit of the coefficients to the data in this situation occurs when

$$Q = (L \hat{s} - z)^T C_v^{-1} (L \hat{s} - z) \rightarrow \min \quad 1.6$$

where C_v^{-1} is the inverse error covariance matrix consisting of only diagonal terms. Setting the derivative of Q with respect to \hat{s} equal to zero gives:

$$\frac{\partial Q}{\partial \hat{s}} = \frac{\partial}{\partial \hat{s}} (\hat{s}^T L^T C_v^{-1} L \hat{s} - \hat{s}^T L^T C_v^{-1} z - z^T (C_v^{-1})^T L \hat{s} + z^T C_v^{-1} z) = 0 \quad 1.7$$

Using the scalar transpose rule and noting that C_v^{-1} is symmetric yields

$$\hat{s}^T L^T C_v^{-1} z = z^T (C_v^{-1})^T L \hat{s} \quad 1.8$$

$$\frac{\partial Q}{\partial \hat{s}} = 2 L^T C_v^{-1} L \hat{s} - 2 L^T C_v^{-1} z = 0 \quad 1.9$$

Therefore

$$\Rightarrow \hat{s} = (L^T C_v^{-1} L)^{-1} L^T C_v^{-1} z \quad 1.10$$

Again \hat{s} can only be evaluated if and only if $(L^T C_v^{-1} L)^{-1}$ exists.

III. Constrained Least Squares Fit

In some cases it is desirable to constrain the estimated coefficients. Such situations arise when observations are not dense enough or of good

enough quality to properly limit the values of the coefficients, or when there exists some overwhelming body of knowledge about the likely values of the coefficients. A constrained least squares fit can be employed in these cases.

The cost function takes on the form:

$$Q = \hat{\mathbf{s}}^T \mathbf{C}_s^{-1} \hat{\mathbf{s}} + (\mathbf{L} \hat{\mathbf{s}} - \mathbf{z})^T \mathbf{C}_v^{-1} (\mathbf{L} \hat{\mathbf{s}} - \mathbf{z}) \rightarrow \min \quad 1.11$$

Minimizing with respect to $\hat{\mathbf{s}}$ gives

$$\frac{\partial Q}{\partial \hat{\mathbf{s}}} = \frac{\partial}{\partial \hat{\mathbf{s}}} (\hat{\mathbf{s}}^T \mathbf{C}_s^{-1} \hat{\mathbf{s}} + \hat{\mathbf{s}}^T \mathbf{L}^T \mathbf{C}_v^{-1} \mathbf{L} \hat{\mathbf{s}} - \hat{\mathbf{s}}^T \mathbf{L}^T \mathbf{C}_v^{-1} \mathbf{z} - \mathbf{z}^T (\mathbf{C}_v^{-1})^T \mathbf{L} \hat{\mathbf{s}} + \mathbf{z}^T \mathbf{C}_v^{-1} \mathbf{z}) = 0 \quad 1.12$$

$$= \frac{\partial}{\partial \hat{\mathbf{s}}} [\hat{\mathbf{s}}^T (\mathbf{C}_s^{-1} + \mathbf{L}^T \mathbf{C}_v^{-1} \mathbf{L}) \hat{\mathbf{s}} - \hat{\mathbf{s}}^T \mathbf{L}^T \mathbf{C}_v^{-1} \mathbf{z} - \mathbf{z}^T (\mathbf{C}_v^{-1})^T \mathbf{L} \hat{\mathbf{s}} + \mathbf{z}^T \mathbf{C}_v^{-1} \mathbf{z}] = 0 \quad 1.13$$

Again using the scalar transpose rule and noting that \mathbf{C}_v^{-1} is symmetric yields

$$\frac{\partial Q}{\partial \hat{\mathbf{s}}} = 2(\mathbf{C}_s^{-1} + \mathbf{L}^T \mathbf{C}_v^{-1} \mathbf{L}) \hat{\mathbf{s}} - 2 \mathbf{L}^T \mathbf{C}_v^{-1} \mathbf{z} = 0 \quad 1.14$$

$$\Rightarrow \hat{\mathbf{s}} = (\mathbf{C}_s^{-1} + \mathbf{L}^T \mathbf{C}_v^{-1} \mathbf{L})^{-1} \mathbf{L}^T \mathbf{C}_v^{-1} \mathbf{z} \quad 1.15$$

In this case the matrix \mathbf{C}_s^{-1} helps to guarantee the existence of

$$(\mathbf{C}_s^{-1} + \mathbf{L}^T \mathbf{C}_v^{-1} \mathbf{L})^{-1}$$

APPENDIX II

OPTIMAL LINEAR ESTIMATION

I. Estimating $\hat{\mathbf{s}}$

Richmond and Kamide (1988) use a constrained least squares fit of the estimated coefficients to the data. The estimates $\hat{\mathbf{s}}$ are made with a minimum mean square error estimator:

$$\mathbf{e} = (\hat{\mathbf{s}} - \mathbf{s}) \quad \text{II.1}$$

where \mathbf{s} is a true but unknown vector whose values are sought and \mathbf{e} is to be minimized. One method of minimizing \mathbf{e} is to choose to minimize the diagonal terms of

$$\mathbf{C}_e \equiv \langle \mathbf{e}\mathbf{e}^T \rangle = \langle (\hat{\mathbf{s}} - \mathbf{s})(\hat{\mathbf{s}} - \mathbf{s})^T \rangle \quad \text{II.2}$$

where $\langle \rangle$ indicates expected value. The Gauss-Markov theorem states that

$$\hat{\mathbf{s}} = \mathbf{C}_{sz} \mathbf{C}_z^{-1} \mathbf{z} \quad \text{II.3}$$

is a linear minimum mean square estimate of \mathbf{s} . The matrix \mathbf{C}_{sz} is the covariance between the independent and dependent variables. The matrix \mathbf{C}_z is the variance of the data and is used to weight the data in the estimation. We will assume the observations are linearly related to \mathbf{s} , that is

$$\mathbf{z} = \mathbf{L}\mathbf{s} + \mathbf{v} \quad \text{II.4}$$

where \mathbf{L} in this case is the matrix of basis functions and the elements of \mathbf{v} are assumed to be randomly distributed with zero mean and covariance \mathbf{C}_v . Then

$$\begin{aligned} \mathbf{C}_{sz} &= \langle \mathbf{s}\mathbf{z}^T \rangle = \langle \mathbf{s}(\mathbf{L}\mathbf{s} + \mathbf{v})^T \rangle \\ &= \langle \mathbf{s}(\mathbf{s}^T \mathbf{L}^T + \mathbf{v}^T) \rangle \\ &= \langle \mathbf{s}\mathbf{s}^T \mathbf{L}^T \rangle + \langle \mathbf{s}\mathbf{v}^T \rangle \\ &= \mathbf{C}_s \mathbf{L}^T + \mathbf{C}_{sv} \end{aligned} \quad \text{II.5}$$

and

$$\begin{aligned}
C_z &= \langle zz^T \rangle \\
&= \langle (Ls + v)(Ls + v)^T \rangle \\
&= \langle (Ls + v)(s^T L^T + v^T) \rangle \\
&= \langle Lss^T L^T + vs^T L^T + Lsv^T + vv^T \rangle \\
&= L \langle ss^T \rangle L^T + \langle sv^T \rangle L^T + L \langle sv^T \rangle + \langle vv^T \rangle \\
&= LC_s L^T + C_{sv}^T L^T + LC_{sv} + C_v
\end{aligned} \tag{II.6}$$

Using these results and the Gauss-Markov Theorem gives:

$$\hat{s} = [C_s L^T + C_{sv}] [LC_s L^T + (LC_{sv})^T + LC_{sv} + C_v]^{-1} z \tag{II.7}$$

We will assume that the estimates and data variances are uncorrelated.

Therefore, $C_{sv} \rightarrow 0$ and

$$\hat{s} = [C_s L^T] [LC_s L^T + C_v]^{-1} z \tag{II.8}$$

$$\text{or} \quad \hat{s} = Az \tag{II.9}$$

$$\text{where} \quad A = [C_s L^T] [LC_s L^T + C_v]^{-1} \tag{II.10}$$

This formulation for A is useful if the number of coefficients to be estimated is less than the number of observations. If this is not the case then we can express the formulation for A in another way. Using Liebelt's (1967) matrix identity 1-51 $XY^T(Z + YXY)^{-1} = (X^{-1} + Y^T Z^{-1} Y)^{-1} Y^T Z^{-1}$, where X and Z are square matrices and letting $C_s \rightarrow X$, $L \rightarrow Y$, $C_v \rightarrow Z$ then:

$$\hat{s} = (C_s^{-1} + L^T C_v^{-1} L)^{-1} L^T C_v^{-1} z \tag{II.11}$$

which is computationally easier than (II.8) if $J < I$

II Uncertainty C_s

It is possible to quantify the uncertainty in the estimation by again considering the minimum mean square of the estimate

$$\begin{aligned}
C_e &\equiv \langle ee^T \rangle \\
&\equiv \langle ee^T \rangle \\
&= \langle (Az - s)(Az - s)^T \rangle \\
&= \langle (Az - s)(z^T A^T - s^T) \rangle \\
&= \langle Azz^T A^T - sz^T A^T - Azs^T + ss^T \rangle \\
&= \langle Azz^T A^T \rangle - \langle sz^T A^T \rangle - \langle Azs^T \rangle + \langle ss^T \rangle \\
&= A \langle zz^T \rangle A^T - \langle sz^T \rangle A^T - A \langle zs^T \rangle + \langle ss^T \rangle \\
&= AC_z A^T - C_{sz} A^T - AC_{zs} + C_s
\end{aligned} \tag{II.12}$$

but $C_{zs} = \langle zs^T \rangle = \langle sz^T \rangle^T = C_{sz}^T$.

$$\therefore C_e = AC_z A^T - C_{sz} A^T - AC_{sz}^T + C_s \tag{II.13}$$

Now using Liebelt's (1967) matrix identity (1-53):

$$XZX^T - YX^T - XY^T = (X - YZ^{-1})Z(X - YZ^{-1})^T - YZ^{-1}Y^T \text{ where } Z = Z^T \text{ and letting}$$

$$A \rightarrow X, C_{sz} \rightarrow Y, C_z = C_z^T \rightarrow Z \text{ then,}$$

$$C_e = (A - C_{sz}C_z^{-1})C_z(A - C_{sz}C_z^{-1})^T - C_{sz}C_z^{-1}C_{sz}^T + C_s \tag{II.14}$$

This quantity is minimized if $A = C_{sz}C_z^{-1}$ leaving only the terms:

$$\begin{aligned}
C_e &= C_s - C_{sz}C_z^{-1}C_{sz}^T \\
&= C_s - AC_{sz}^T
\end{aligned} \tag{II.15}$$

But

$$\begin{aligned}
C_{sz} &= \langle sz^T \rangle = \langle s(Ls + v)^T \rangle \\
&= \langle s(s^T L^T + v^T) \rangle \\
&= \langle ss^T \rangle L^T + \langle sv^T \rangle \\
&= C_s L^T + C_{sv} = C_s L^T + 0
\end{aligned} \tag{II.16}$$

$$\begin{aligned}
\therefore C_e &= C_s - A(C_s L^T)^T \\
&= C_s - ALC_s^T
\end{aligned} \tag{II.17}$$

Now, recalling equations II.15, II.6 and II.5:

$$C_e = C_s - C_{sz}C_z^{-1}C_{sz}^T \text{ and } C_z = LC_s L^T + C_{sv}^T L^T + LC_{sv} + C_v$$

and $C_{sz} = C_s L^T$ along with $C_{sv} \rightarrow 0$ yields:

$$\begin{aligned}
\therefore C_s &= C_s - (C_s L^T) (C_s L^T + C_{sv}^T L^T + L C_{sv} + C_v)^{-1} (C_s L^T)^T \\
&= C_s - (C_s L^T) (C_s L^T + 0 + 0 + C_v)^{-1} (C_s L^T)^T \\
&= C_s - (C_s L^T) (C_s L^T + C_v)^{-1} (L C_s^T)
\end{aligned}
\tag{II.18}$$

Again, assuming Z and X are square matrices and using Liebelt's (1967) matrix identity (1-45) $(Z^{-1} + Y^T X^{-1} Y)^{-1} = Z - ZY^T(YZY^T + X)^{-1}YZ$ for the inverse term and letting $C_v \rightarrow X$, $L \rightarrow Y$, $C_s \rightarrow Z$ yields:

$$C_s = (C_s^{-1} + L^T C_v^{-1} L)^{-1} \tag{II.19}$$

Equating results from equations II.17 and II.19 gives

$C_s = (C_s^{-1} + L^T C_v^{-1} L)^{-1} = C_s - ALC_s^T \tag{II.20}$
--

APPENDIX III

CONDUCTANCE DERIVATIONS

The balance of forces on ions gives:

$$-\nabla p_j + n_j e_j \left[\mathbf{E} + \mathbf{u} \times \mathbf{B} + \left(\frac{m_j}{e} \right) \mathbf{G} \right] + n_j e_j \mathbf{v}_j \times \mathbf{B} = n_j m_j \nu_j \mathbf{v}_j \quad \text{III.1}$$

where

j is the particular ion species of interest,

p_j is the ion pressure,

\mathbf{u} is the center of mass velocity of the atmosphere (approximately equal to the neutral wind velocity),

\mathbf{v}_j is the ion velocity relative to the center of mass,

\mathbf{G} is the gravitational acceleration and

ν_j is the ion collision frequency, summed over all particles

Similarly the electron momentum conservation equation is

$$-\nabla p_e - n_e e \left[\mathbf{E} + \mathbf{u} \times \mathbf{B} + \left(\frac{m_e}{e} \right) \mathbf{G} \right] - n_e e \mathbf{v}_e \times \mathbf{B} = n_e m_e \nu_e \mathbf{v}_e \quad \text{III.2}$$

where ν_e is the electron collision frequency. The effects of conductivity are most usefully classified according to their contribution parallel and perpendicular to the magnetic field lines. To determine the parallel contribution, effective electric fields

$$\mathbf{E}'_{\parallel j} = \mathbf{E} + \mathbf{u} \times \mathbf{B} + \left(\frac{m_j}{e} \right) \mathbf{G} - \frac{1}{n_j e_j} \nabla p_j \quad \text{III.3a}$$

$$\mathbf{E}'_{\parallel e} = \mathbf{E} + \mathbf{u} \times \mathbf{B} + \left(\frac{m_e}{e} \right) \mathbf{G} - \frac{1}{n_e e} \nabla p_e \quad \text{III.3b}$$

are usually defined. Using the effective electric field, \mathbf{E}' , the parallel component of equation 4.5 can be rearranged as

$$\mathbf{E}'_{\parallel j} \cdot \mathbf{b} = \frac{m_j \nu_j}{e} \mathbf{v}_j \cdot \mathbf{b} \quad \text{III.4a}$$

$$\mathbf{E}'_{\parallel e} \cdot \mathbf{b} = \frac{m_e \nu_e}{e} \mathbf{v}_e \cdot \mathbf{b} \quad \text{III.4b}$$

Collisions in the ionosphere reduce ion mobility therefore $\mathbf{j} \approx \mathbf{j}_e = -n_e e \mathbf{v}_e$ and equation 4.6 can be further simplified to

$$\mathbf{E} \cdot \mathbf{b} = + \frac{\mathbf{j} \cdot \mathbf{b}}{\sigma_{\parallel}} \quad \text{III.5}$$

where $\sigma_{\parallel} = n_e e^2 / m_e v_e$ III.6

and $j_{\parallel} = \frac{n_e e^2}{m_e v_e} E_{\parallel}$ III.7

The components perpendicular to the magnetic field lines may be determined by writing the perpendicular effective electric fields as

$$\mathbf{E}_{\perp i} = \left[\mathbf{E} + \mathbf{u} \times \mathbf{B} - \frac{1}{n_i e} \nabla p + \frac{m_i}{e} \mathbf{G} \right] \quad \text{III.8a}$$

$$\mathbf{E}_{\perp e} = \left[\mathbf{E} + \mathbf{u} \times \mathbf{B} - \frac{1}{n_e e} \nabla p + \frac{m_e}{e} \mathbf{G} \right] \quad \text{III.8b}$$

Then the equation for perpendicular ion and electron motion becomes

$$\frac{e}{m_i} \mathbf{E}_{\perp i} + \mathbf{v}_i \times \Omega_i = v_i \mathbf{v}_i \quad \text{III.9a}$$

and

$$\frac{e}{m_e} \mathbf{E}_{\perp e} + \mathbf{v}_e \times \Omega_e = v_e \mathbf{v}_e \quad \text{III.9b}$$

where

$$\Omega_i = e \mathbf{B} / m_i \text{ and } -\Omega_e = -e \mathbf{B} / m_e \text{ or } |\Omega| = e \mathbf{B} / m_e$$

Solving for the perpendicular velocities gives

$$\mathbf{v}_{i\perp} = \frac{e}{m_i} \left[\mathbf{v}_i / (\Omega_i^2 + v_i^2) \right] \mathbf{E}_{\perp i} - \frac{e}{m_i} \left[\Omega_i / (\Omega_i^2 + v_i^2) \right] \mathbf{b} \times \mathbf{E}_{\perp i} \quad \text{III.10a}$$

$$\mathbf{v}_{e\perp} = \frac{e}{m_e} \left[\mathbf{v}_e / (\Omega_e^2 + v_e^2) \right] \mathbf{E}_{\perp e} - \frac{e}{m_e} \left[\Omega_e / (\Omega_e^2 + v_e^2) \right] \mathbf{b} \times \mathbf{E}_{\perp e} \quad \text{III.10b}$$

The perpendicular current components are

$$\begin{aligned} \mathbf{j}_{i\perp} &= \Sigma n_i e_i \mathbf{v}_{i\perp} \\ &= \Sigma \frac{n_i e_i}{B} \left[\left(\frac{v_i |\Omega_i|}{1 + (v_i / \Omega_i)^2} \right) \mathbf{E}_{\perp i} - \left(\frac{1}{1 + (v_i / \Omega_i)^2} \right) \mathbf{b} \times \mathbf{E}_{\perp i} \right] \end{aligned} \quad \text{III.11a}$$

$$\begin{aligned} \mathbf{j}_{e\perp} &= n_e e_e \mathbf{v}_{e\perp} \\ &= \frac{n_e e_e}{B} \left[\left(\frac{v_e |\Omega_e|}{1 + (v_e / \Omega_e)^2} \right) \mathbf{E}_{\perp e} + \left(\frac{1}{1 + (v_e / \Omega_e)^2} \right) \mathbf{b} \times \mathbf{E}_{\perp e} \right] \end{aligned} \quad \text{III.11b}$$

The two components of conductivity arise from these latter formulations: the conductivity component perpendicular to B but parallel to E is called the Pedersen conductivity and is given by

$$\sigma_p = \frac{e}{B} \left[\left(\frac{n_e v_e / |\Omega_e|}{1 + (v_e / \Omega_e)^2} \right) + \sum_i n_i \left(\frac{v_i / \Omega_i}{1 + (v_i / \Omega_i)^2} \right) \right] \quad \text{III.12a}$$

which can also be written as

$$\sigma_p = \left[\frac{n_e}{m_e v_e} \left(\frac{v_e^2}{v_e^2 + \Omega_e^2} \right) + \frac{n_i}{m_i v_i} \left(\frac{v_i^2}{v_i^2 + \Omega_i^2} \right) \right] |e|^2 \quad \text{III.12b}$$

The conductivity perpendicular to both B and E is the Hall conductivity and is given by

$$\sigma_H = \frac{e}{B} \left[\left(\frac{n_e}{1 + (v_e / \Omega_e)^2} \right) - \sum_i n_i \left(\frac{1}{1 + (v_i / \Omega_i)^2} \right) \right] \quad \text{III.13a}$$

which can also be expressed as

$$\sigma_H = \left[\frac{n_e}{m_e v_e} \left(\frac{\Omega_e v_e}{v_e^2 + \Omega_e^2} \right) - \frac{n_i}{m_i v_i} \left(\frac{\Omega_i v_i}{v_i^2 + \Omega_i^2} \right) \right] |e|^2 \quad \text{III.13b}$$

The Hall conductivity dominates for electrons since at auroral heights $v_e \ll \Omega_e$. Contributions to the ion Pedersen conductance is significant around 140 km where $v_i > \Omega_i$ but decreases below that height due to the square factor in the denominator in the second term of equation 4.14. In these formulas the magnetic induction B and the ion and electron gyrofrequencies are generally well known. The collision frequency proves to be more problematic with different researchers using slightly different values. Robinson et al. (1987) use $v_i (\text{s}^{-1}) = 3.75 \times 10^{-10} n_n (\text{cm}^{-3})$ where n_n is the neutral density derived from standard atmospheric models. The height-integrated Hall and Pedersen conductivities (conductances) are defined by

$$\Sigma_p = \int \sigma_p dh \quad \text{and} \quad \Sigma_H = \int \sigma_H dh \quad \text{III.14}$$

Conductivity units in MKS are in mhos per meter (mho/m) or Siemens per meter (S/m) and the conductances are given in mhos or Siemens (S).

ELECTRODYNAMIC RELATIONS

APPENDIX IV

The purpose of the appendix is to show the relations between magnetic perturbations, magnetic potential and electric current .

I. HORIZONTAL CURRENTS

A External currents

If we consider a current density \mathbf{J} flowing on a thin shell located at radius a we can express the current in terms of a current function Ψ

$$\mathbf{J} = \hat{\mathbf{r}} \times \nabla \Psi \delta(r - a) = I \delta(r - a) \quad \text{IV.1}$$

where \mathbf{r} is a unit radius vector and δ is a Dirac delta function.

1. Horizontal Component

It is often the case that we would like to know what magnetic perturbations are caused by such a current (or vice versa). From Ampere's Law we have:

$$\nabla \times \Delta \mathbf{B} = \hat{\mathbf{r}} \times \mu_0 \mathbf{J} \quad \text{IV.2}$$

For a thin current shell the curl is manifest only in the transverse or horizontal component of the magnetic perturbations:

$$\Delta \mathbf{B}_h^+ - \Delta \mathbf{B}_h^- = - \mu_0 \hat{\mathbf{r}} \times \mathbf{l} \quad \text{IV.3}$$

where $\Delta \mathbf{B}_h^+$ and $\Delta \mathbf{B}_h^-$ are the horizontal perturbations above and below the current shell. The radial component of $\Delta \mathbf{B}$ is unchanged across the current sheet. The horizontal discontinuity in the magnetic perturbations can be expressed as the horizontal gradient in the current function by combining IV.1 and IV.3 (note for a two dimensional function like Ψ the vertical gradient does not exist).

$$\Delta \mathbf{B}_h^+ - \Delta \mathbf{B}_h^- = - \mu_0 \hat{\mathbf{r}} \times (\hat{\mathbf{r}} \times \nabla \Psi) = \mu_0 \nabla_{\perp} \Psi \quad \text{IV.4}$$

We can also represent the magnetic perturbation in the regions above and below the shell where no current flows in terms of the scalar potential V .

$$\mathbf{B} = -\nabla V \quad \text{IV.5}$$

From Jackson (1975, Chp 3), the general expression for V is

$$V = V^+ + V^- = \sum_{n=0}^{\infty} \sum_{m=-n}^n \left[V_n^m Y_n^m(\theta, \phi) \left(\frac{a}{r}\right)^{n+1} + V_n^m Y_n^m(\theta, \phi) \left(\frac{r}{a}\right)^n \right] \quad \text{IV.6}$$

where $Y_n^m(\theta, \phi)$ are the spherical harmonics of the potential and V_n^m are the associated coefficients. Above the shell the V_n^m 's are zero, while below the shell the V_n^m 's are zero (ignoring effects of induced earth currents).

Evaluating the discontinuity at $r=a$ and expanding in harmonics yields:

$$\Delta \mathbf{B}_{ha}^+ - \Delta \mathbf{B}_{ha}^- = -\nabla_h V_a^+ + \nabla_h V_a^- = \mu_0 \nabla_{ha} \Psi$$

IV.7

$$\sum_{n=0}^{\infty} \Delta \mathbf{B}_{an}^+ - \Delta \mathbf{B}_{an}^- = \sum_{n=0}^{\infty} \sum_{m=-n}^n [-V_n^m + V_n^m] \nabla_h Y_n^m(\theta, \phi) \quad \text{IV.8}$$

$$= \mu_0 \sum_{n=0}^{\infty} \sum_{m=-n}^n \nabla_h \Psi_n^m \nabla_h Y_n^m(\theta, \phi) \quad \text{IV.9}$$

Summing over m gives

$$\Delta \mathbf{B}_{ha}^+ - \Delta \mathbf{B}_{ha}^- = \mu_0 \sum_{n=0}^{\infty} \Psi_n \quad \text{IV.10}$$

It is possible to determine the coefficients from the boundary conditions on the radial component.

2. Radial Component

The radial component of \mathbf{B} is continuous across the current sheet, that is:

$$\begin{aligned} \hat{r} \cdot (\Delta \mathbf{B}_a^+ - \Delta \mathbf{B}_a^-) &= 0 = - \left[\frac{\partial V^+}{\partial r} - \frac{\partial V^-}{\partial r} \right]_{r=a} \\ &= - \frac{\partial}{\partial r} \left[\sum_{n=0}^{\infty} V_n^m Y_n^m(\theta, \phi) \left(\frac{a}{r}\right)^{n+1} - V_n^m Y_n^m(\theta, \phi) \left(\frac{r}{a}\right)^n \right]_{r=a} \end{aligned} \quad \text{IV.11a}$$

$$= - \left\{ \sum_{n=0}^{\infty} \left(- \frac{(n+1)}{a} V_n^m \cdot Y_n^m(\theta, \phi) \left(\frac{a}{r} \right)^{n+2} \right) \Big|_{r=a} - \frac{n}{a} V_n^m \cdot Y_n^m(\theta, \phi) \left(\frac{r}{a} \right)^{n-1} \Big|_{r=a} \right\}$$

IV.11b

$$\Rightarrow - (n+1) V_n^{m+} - n V_n^{m-} = 0$$

IV.11c

$$\Rightarrow V_n^{m+} = - \frac{n}{n+1} V_n^{m-}$$

IV.11d

Using IV.7 and IV.11d

$$\mu_0 \psi_n^m = \left(1 + \frac{n}{n+1} \right) V_n^{m-}$$

IV.12

$$\Rightarrow V_n^{m-} = \mu_0 \left(\frac{n+1}{2n+1} \right) \psi_n^m$$

IV.13

The horizontal component at any height above the current sheet is given by

Above: $\Delta \mathbf{B}_h^+ = - \nabla_h V^+$ IV.14

Below: $\Delta \mathbf{B}_h^- = - \nabla_h V^-$ IV.15

Combining IV.6, IV.12 IV.15 gives

$$V^+ = \sum_{n=0}^{\infty} \sum_{m=-n}^n V_n^m \cdot Y_n^m(\theta, \phi) \left(\frac{a}{r} \right)^{n+1}$$

IV.16a

$$= \sum_{n=0}^{\infty} \sum_{m=-n}^n \frac{-n}{n+1} V_n^{m-} \cdot Y_n^m(\theta, \phi) \left(\frac{a}{r} \right)^{n+1}$$

IV.16b

$$= \mu_0 \sum_{n=0}^{\infty} \sum_{m=-n}^n \left(\frac{-n}{2n+1} \right) \psi_n^m Y_n^m(\theta, \phi) \left(\frac{a}{r} \right)^{n+1}$$

IV.16c

$$V^- = \mu_0 \sum_{n=0}^{\infty} \sum_{m=-n}^n \frac{n+1}{2n+1} \psi_n^m Y_n^m(\theta, \phi) \left(\frac{r}{a} \right)^n$$

IV.17

The total magnetic perturbation is then

$$\Delta \mathbf{B}^+ = \sum_{n=0}^{\infty} \frac{\mu_0 n}{2n+1} \left(\frac{a}{r} \right)^{n+1} \nabla \psi_n - \frac{\mu_0 n(n+1)}{2n+1} \left(\frac{a}{r} \right)^{n+2} \frac{\psi_n}{a} \hat{r}$$

IV.18

$$\Delta \mathbf{B}^- = \sum_{n=0}^{\infty} \frac{-\mu_0(n+1)}{2n+1} \left(\frac{r}{a}\right)^n \nabla \psi_n - \frac{\mu_0 n(n+1)}{2n+1} \left(\frac{r}{a}\right)^{n-1} \frac{\psi_n}{a} \hat{\mathbf{r}} \quad \text{IV.19}$$

B. Internal Currents

We may also wish to know what magnetic perturbations are produced by internal earth currents. The magnetic perturbations are associated with the scalar potential above the induced current shell

$$\Delta \mathbf{B}^{+i} = -\nabla V^{+i} \quad \text{IV.20}$$

From equation IV.6 we know this term is proportional to $\left(\frac{c}{r}\right)^{n+1}$ where c is the location of the induced current. Therefore

$$V^{+i} = \alpha \left(\frac{c}{r}\right)^{n+1} \quad \text{IV.21}$$

where α is to be found from boundary conditions. We also know from IV.11 that

$$\left. \frac{\partial V^i}{\partial r} \right|_{r=c} = \frac{(n+1)\alpha}{c} = \Delta \mathbf{B}_r^i \quad \text{IV.22}$$

The fact that the internal and external $\Delta \mathbf{B}_r$'s must sum to zero at the induced current sheet provides the condition

$$\Delta \mathbf{B}_r^{+i} = -\Delta \mathbf{B}_r^{-e} = \frac{n(n+1)}{2n+1} \frac{\mu_0 \Psi}{a} \left(\frac{c}{a}\right)^{n-1} \quad \text{IV.23}$$

$$\Rightarrow \alpha = \frac{n\mu_0 \Psi}{2n+1} \left(\frac{c}{a}\right)^{n-1} \quad \text{IV.24}$$

Therefore

$$V^{+i} = \frac{n\mu_0 \Psi}{2n+1} \left(\frac{c}{a}\right)^{n-1} \left(\frac{c}{r}\right)^{n+1} \quad \text{IV.25}$$

$$\Delta \mathbf{B}_h = -\nabla V^{+i} = \sum_{n=0}^{\infty} \sum_{m=-n}^n \frac{-n\mu_0}{2n+1} \left(\frac{c}{a}\right)^{n-1} \left(\frac{c}{r}\right)^{n+1} \nabla \Psi \quad \text{IV.26}$$

$$\Delta \mathbf{B}_r = -\frac{\partial V^{+i}}{\partial r} = \sum_{n=0}^{\infty} \sum_{m=-n}^n \frac{-n\mu_0}{2n+1} \frac{n+1}{c} \left(\frac{c}{a}\right)^{n-1} \left(\frac{c}{r}\right)^{n+2} \Psi \quad \text{V.27}$$

Summing over m gives

$$\Delta \mathbf{B}^{+i} = \left(\frac{c}{a}\right)^{n-1} \left[\sum_{n=0}^{\infty} \frac{-n\mu_0}{2n+1} \left(\frac{c}{r}\right)^{n+1} \nabla \Psi_n + \frac{-n\mu_0}{2n+1} \frac{n+1}{c} \left(\frac{c}{r}\right)^{n+2} \Psi_n \hat{\mathbf{r}} \right] \quad \text{IV.28}$$

II. FIELD-ALIGNED CURRENT

In dealing with the effects of field-aligned currents we again consider magnetic perturbations $\Delta \mathbf{B}$ from the main field. The source of the magnetic perturbations in this case is a poloidal current I_p which can be expressed as

$$I_p = -\nabla_h \tau \quad \text{IV.29}$$

The magnetic perturbations produced by field-aligned current below the current shell are assumed to be zero therefore:

$$\Delta \mathbf{B}^+ = -\mu_0 \hat{\mathbf{r}} \times I_p \quad \text{IV.30}$$

Ampere's Law gives

$$\Delta \mathbf{B}_{(r=a^+)} = \mu_0 \hat{\mathbf{r}} \times (\nabla \tau) \quad \text{IV.31}$$

$$\nabla \times (\Delta \mathbf{B}) = -\nabla \times (\mu_0 (\hat{\mathbf{r}} \times \nabla \tau)) \quad \text{IV.32}$$

$$\nabla \times (\Delta \mathbf{B}) = -[\mu_0 (\nabla \cdot \nabla \tau) - (\nabla \times \hat{\mathbf{r}}) \nabla \tau] \quad \text{IV.33}$$

The radial component of the associated current is given by

$$\nabla \times (\Delta \mathbf{B}) = -\mu_0 (\nabla^2 \tau) = \mu_0 J_{||} \quad \text{IV.34}$$

It is important to point out that a radial dependence will appear in the field-aligned current intensity. If the field-aligned currents are assumed to be radial (as in AMIE) the divergence of the magnetic flux tubes along which the currents travel introduce a r^{-1} dependency to the current density. If the field-aligned current are assumed to flow along dipolar field lines the dependency is $(r / R_E)^{3/2}$. Failure to account for the dipole nature of the field-lines may account for ~ 20% error in the current density estimates (Rich et al., 1987)

REFERENCES

- Ahn, B.-H., R. M. Robinson, Y. Kamide, and S.-I. Akasofu, Electric conductivities, electric fields and auroral particle energy injection rate in the auroral ionosphere and their empirical relations to the horizontal magnetic disturbances, Planet. Space Sci., **31**, 641, 1983.
- Ahn, B.-H., E. Friis-Chistensen, D. J. Gorney, Y. Kamide, H. W. Kroehl, P. F. Mizera, A. D. Richmond, C. G. Sucksdorf, and C. D. Wells, Numerical modeling of polar ionospheric electrodynamics for July 23-24, 1983 utilizing ionospheric conductances deduced from DMSP X-ray images, Report UAG-97 World Data Center A, National Geophysical Data Center, Boulder CO, 1988.
- Akasofu, S.-I., The development of the auroral substorm, Planet. Space Sci., **12**, 273, 1964.
- Akasofu, S.-I., S. Chapman and C.-I. Meng, The polar electrojet, J. Atmos and Terr. Phy., **27**, 1275, 1965.
- Akasofu, S.-I., Recent progress in studies of DMSP auroral photographs, Space Sci. Rev., **19**, 169, 1976.
- Akasofu, S.-I., Study of individual geomagnetic storms in terms of the solar wind, Planet. Space Sci., **28**, 933, 1980.
- Akasofu, S. -I., G. J. Romick, B.-H. Ahn, H. W. Kroehl J. H. Allen, and J. L. Kisabeth, Average daily magnetic variation pattern and its equivalent current pattern determined by the IMS Alaska meridian chain of observatories, Geophys. Res. Lett., **6**, 885, 1979.
- Akasofu, S.-I., and Y. Kamide, The aurora, in *The Solar Wind and the Earth*, edited by S.-I. Akasofu and Y. Kamide, 143, Terra Scientific Publishing Co., Tokyo, Japan, 1987.

- Akasofu, S.-I., Y. Kamide, and J. L. Kisabeth, Comparison of two modeling methods for three-dimensional current systems, J. Geophys. Res., **86**, 3389, 1981.
- Appleton, E. V., and M. A. F. Barnett, On some direct evidence for downward atmospheric reflection of electric rays, Proc. Roy. Soc. (London) **109**, 621, 1926.
- Armstrong, J. C., and A. J. Zmuda, Triaxial magnetic measurements of field-aligned currents at 800 km in the auroral region: Initial results, J. Geophys. Res., **78**, 6802, 1973.
- Axford, W. I., and C. O. Hines, A unifying theory of high-latitude geophysical phenomena and geomagnetic storms, Can. J. Phys., **39**, 1433, 1961.
- Banks, P. M. and A. F. Nagy, Photoelectron fluxes in the ionosphere, J. Geophys. Res., **75**, 6260, 1970.
- Baumjohann, W., Ionospheric and field-aligned current systems in the auroral zone: A concise review, Adv. Space Res., **2**, 55, 1983.
- Birkeland, K. , *The Norwegian Aurora Polaris Expedition 1902-1903, Vol 1, 1st Sec.*, Aschhoug, Christiana, 1908.
- Boström, R., A model of the auroral electrojets, J. Geophys. Res., **69**, 4983, 1964.
- Breit, G. and M. Tuve, A radio method for estimating the height of the ionosphere conducting layer, Nature, **116**, 357, 1925.
- Brekke, A., J. R. Doupnik, and P. M. Banks, Incoherent scatter measurements of E region conductivities and current in the auroral zone, J. Geophys. Res., **79**, 3773, 1974.
- Brekke, A., and C. Hall, Auroral ionospheric quiet summer time conductances, Ann. Geophys., **6**, 361, 1988.

- Buneman, O., Scattering of radiation by the fluctuations in a nonequilibrium plasma, J. Geophys. Res., 67, 2050, 1962.
- Burch, J. L., The Magnetosphere, in *The Upper Atmosphere and Magnetosphere*, 42 National Academy of Science, Printing and Publishing Office, Washington D. C., 1977.
- Burch, J. L., P. H. Reiff, J. D. Meneitte, R. A. Hellis, W. B. Hanson, S. D. Shawhan, E. G. Shelley, M. Sugiura, D. R. Weimer, and J. D. Winningham, IMF By-dependent plasma flow and Birkeland currents in the dayside magnetosphere. 1. Dynamics Explorer observations, J. Geophys. Res., 90, 1577, 1985.
- Chapman, S., The electric current system of magnetic storms, Terr. Magn., 40, 349, 1935.
- Chappell, C. R. The terrestrial plasma source: A new perspective in solar-terrestrial processes from Dynamics Explorer, Rev. Geophys., 26, 229, 1988.
- Clauer, C. R. , and Y. Kamide, DP 1 and DP 2 current systems for the March 22, 1979, substorms, J. Geophys. Res., 90, 1343, 1985.
- Clauer, D. R., and R. L. McPherron, Mapping of local time-universal time development of magnetospheric substorms using mid-latitude magnetic observations, J. Geophys. Res., 79, 2811, 1974.
- Crooker, N. U., Dayside merging and cusp geometry, J. Geophys. Res., 84, 951, 1979.
- Crooker, N. U., Mapping the merging potential from the magnetosphere to the ionosphere through the dayside cusp, J. Geophys. Res., 93, 7338, 1988.
- Crooker, N. U., and G. L. Siscoe, Birkland currents as the cause of the low-latitude asymmetric disturbance field, J. Geophys. Res., 86, 11201, 1981.

- Crowley, G., B. A. Emery, R. G. Roble, and H. C. Carlson, D. J. Knipp, Thermospheric Dynamics During the Equinox Transition Study Magnetic Storm of 19 September, 1984, I: Model Simulations, submitted to J. Geophys. Res., 1989.
- De La Beaujardiere, O., R. Johnson, and V. B. Wickwar, Ground-based measurements of Joule heating rates, submitted to *Proceedings of the International Conference on Auroral Physics*, Cambridge, 1989.
- De La Beaujardiere, and L. R. Lyons, Instantaneous measurements of the global high latitude convection pattern, submitted to Proceedings of 1988 Yosemite Conference "Outstanding Problems in Solar System Plasma Physics: Theory and Instrumentation, 1988
- Dungey, J. W., Interplanetary magnetic field and the auroral zones, Phys. Rev. Lett., 6, 47, 1961.
- Emery, B. A., private communication, 1989.
- Evans, D. S., Precipitating electron fluxes formed by a magnetic field-aligned potential difference, J. Geophys. Res., 79, 2853, 1974.
- Evans, J. V., J. M. Holt, and R. H. Wand, Millstone Hill incoherent scatter results of auroral convection over $60^\circ < \Lambda < 75^\circ$, 1, Observing and data reduction procedures, J. Geophys. Res., 84, 7059, 1979.
- Evans, J. V., J. M. Holt, W. L. Oliver, and R. H. Wand, Millstone Hill incoherent scatter results of auroral convection over $60^\circ < \Lambda < 75^\circ$, 2, Initial Results, J. Geophys. Res., 85, 41, 1980.
- Feldstein, Y. I., Some problems concerning the morphology of auroras and magnetic disturbances at high latitude, Geomag. Aeron., SSR 3, 183, 1963.
- Feldstein, Y. I., and G. V. Starkov, Dynamics of auroral belt and polar geomagnetic disturbances, Planet. Space Sci., 15, 209, 1967.

- Folkstead, K., T. Hagfors, and S. Westerlund, EISCAT: An updated description of technical characteristics and operational capabilities, Radio Sci., 18, 867, 1983.
- Foster, J. C., J. M. Holt, R. G. Musgrove, and D. S. Evans, Ionospheric convection associated with discrete levels of particle precipitation, Geophys. Res. Lett., 13, 656, 1986.
- Friis-Christensen, E., Y. Kamide, A. D. Richmond, and S. Matsushita, Interplanetary magnetic field control of high-latitude electric fields and currents determined from Greenland magnetometer data, J. Geophys. Res., 90, 1325, 1985.
- Fukushima, N., Equivalence in ground geomagnetic effect of Chapman-Vestine's and Birkeland-Alfvén's current systems for polar magnetic storms, Rep. Ionos. Space Res. Jap., 32, 219, 1969.
- Fuller-Rowell, T. J., and D. S. Evans, Height-integrated Pedersen and Hall conductivity patterns inferred from the TIROS-NOAA satellite data, J. Geophys. Res., 92, 7606, 1987.
- Gorney, D. J., P. F. Mizera and J. L. Roeder, A maximum-entropy technique for deconvolution of atmospheric bremsstrahlung spectra, Air Force Systems Command, Space Division, SD-TR-86-65, Los Angeles CA, 1986.
- Gorney, D. J., private communication, 1989.
- Haines, G. V., Spherical cap harmonic analysis, J. Geophys. Res., 90, 2583, 1985.
- Hardy, D. A., M. S. Gussenhoven, J. Reihl, R. Burkhardt, N. Heinemann, and T. Schumaker, The characteristics of polar cap precipitation and their dependence on the interplanetary magnetic field and the solar wind, in

- Solar-Wind Magnetosphere Coupling*, edited by Y. Kamide and A. Slavin, 575, Terra Scientific Publishing Company, Tokyo, 1986.
- Hardy, D. A., M. S. Gussenhoven, and R. Raistrick, Statistical and Functional Representations of the Pattern of Auroral Energy Flux, and Conductivity, J. Geophys. Res., 92, 12,275, 1987.
- Harel, M. A., R. A. Wolf, P. H. Reiff, R. W. Spiro, W. J. Burke, F. J. Rich, and M. Smiddy, Quantitative simulation of a magnetosphere substorm, 1. Model logic and overview, J. Geophys. Res., 86, 2242, 1981a.
- Harel, M., R. A. Wolf, R. W. Spiro, P. H. Reiff, C. K. Chen, W. J. Burke, F. J. Rich, and M. Smiddy, Quantitative simulation of a magnetospheric substorm, 2. Comparison with observations, J. Geophys. Res., 86, 2242, 1981b.
- Hargreaves, J. K., *The Upper Atmosphere and Solar-Terrestrial Relations*, Van Nostrand Reinhold Co., Berkshire, England, 1979.
- Hayashi, T., and T. Sato, Magnetic reconnection: acceleration, heating, and shock formation, J. Geophys. Res., 83, 217, 1978.
- Heikkila, W. J., J. D. Winningham, R. H. Eather, and S.-I. Akasofu, Auroral emission and particle precipitation in the noon sector, J. Geophys. Res., 77, 4100, 1972.
- Heppner, J. P., Polar cap electric field distributions related to the interplanetary magnetic field direction, J. Geophys. Res., 77, 4877, 1972.
- Heppner, J. P., Empirical models of high latitude electric fields, J. Geophys. Res., 82, 1115, 1977.
- Heppner, J. P., and N. C. Maynard, Empirical high-latitude electric field models, J. Geophys. Res., 92, 4467, 1987.

- Hones, E. W., Substorm processes in the magnetotail: comments on 'On hot tenuous plasmas, fireballs and boundary layers in earth's magnetotail' by L. A. Frank et al., J. Geophys. Res., 82, 4467, 1977.
- Hughes, T. J., and G. Rostoker, Current flow in the magnetosphere and ionosphere during periods of moderate activity, J. Geophys. Res., 82, 2271, 1977.
- Iijima, T. and T. A. Potemra, The amplitude distribution of field-aligned currents at northern high latitudes observed by TRIAD, J. Geophys. Res., 81, 2165, 1976a.
- Iijima, T., and T. A. Potemra, Field-aligned currents in the dayside cusp observed by TRIAD, J. Geophys. Res., 81, 5971, 1976b.
- Iijima, T., and T. A. Potemra, Large-scale characteristics of field-aligned currents associated with substorms, J. Geophys. Res., 83, 599, 1978.
- Imhof, W. L., T. J. Rosenberg, L. J. Lanzerotti, J. B. Reagan, H. D. Voss, D. W. Datlowe, J. R. Kilner, E. E. Gaines, J. Mobilia and R. G. Joiner, A coordinated satellite and ground-based study of an intense electron precipitation spike over the southern polar cap, J. Geophys. Res., 89, 10837, 1984.
- Jackson, D. D., The use of a priori data to resolve non-uniqueness in linear inversions, J. Geophys. Res., 84, 137, 1979.
- Jackson, D., personal communication, 1989.
- Jackson, J. D., *Classical Electrodynamics*, John Wiley and Sons, New York, 1962.
- Jones, A. V., *The Aurora*, D. Reidel Publishing Co., 1974.
- Jones, A. G., Geomagnetic induction studies in Scandinavia II. geomagnetic depth sounding, induction vectors and coast effect, J. Geophys. Res., 50, 23, 1981.

- Kamide, Y., *Electrodynamic Processes in the Earth's Ionosphere and Magnetosphere*, Kyoto Sangyo University Press, Kyoto, Japan, 1988.
- Kamide, Y., and A. D. Richmond, Ionospheric conductivity dependence on electric fields and current estimated from ground magnetic observations, J. Geophys. Res., 87, 8331, 1982.
- Kamide, Y., and G. Rostoker, The spatial relationship of field-aligned currents and auroral electrojet to the distribution of nightside auroras, J. Geophys. Res., 82, 5589, 1977.
- Kamide, Y., A. D. Richmond and S. Matsushita, Estimation of ionospheric fields, ionospheric currents and field-aligned currents from ground magnetic records, J. Geophys. Res., 86, 801, 1981.
- Kamide, Y., J. D. Craven, L. A. Frank, B.-H. Ahn, and S.-I. Akasofu, Modeling substorm current systems using conductivity distributions inferred from DE auroral images, J. Geophys. Res., 91, 11235, 1986.
- Kamide, Y., Y. Ishihara, T. L. Killeen, J. D. Craven, L. A. Frank, and R. A. Heelis, Combining electric field and auroral observations from DE 1 and 2 with ground magnetometer records to estimate ionospheric electromagnetic quantities, J. Geophys. Res., 94, 6723, 1989.
- Kaufmann, R. L. and P. M. Kintner, Upgoing ion beams. 2. Fluid analysis and magnetospheric-ionospheric coupling, J. Geophys. Res., 87, 2195, 1984.
- Kawasaki, K., C.-I. Meng, and Y. Kamide, The development of three-dimensional current system during a magnetospheric substorm, Planet. Space Sci., 22, 1471, 1974.
- Kelly, J. D., Sondrestrom radar--initial results, Geophys. Res. Letts., 10, 1112, 1983.

- Kisabeth, J. L., On calculating magnetic and vector potential fields due to large-scale magnetospheric current systems and induced currents in an infinitely conducting earth, in *Quantitative Modeling of Magnetospheric Processes*, ed. by W.P. Olson, 473, Amer. Geophys. Union, Washington, D.C., 1979.
- Kisabeth, J. L., and G. Rostoker, Modelling of three-dimensional current systems associated with magnetospheric substorms, Geophys. J. R. Astron. Soc., **49**, 655, 1977.
- Klumpar, D. M., Field-aligned currents in the evening MLT sector and their association with primary and secondary auroral particles fluxes (abstract), EOS Trans. AGU, **57**, 988, 1976.
- Knipp, D. J., A. D. Richmond, G. Crowley, O. de la Beaujardiere, E. Friis-Christensen, D. S. Evans, J. C. Foster, M. S. Gussenhoven, R. P. Lepping, I.W. McCrea, F. J. Rich, J. A. Waldock, Electrodynamic patterns for September 19 1984, J. Geophys. Res., in press, 1989.
- Krane, K., *Modern Physics*, John Wiley and Sons, New York, 1983.
- Kuppers, F., J. Untiedt, and W. Baumjohann, A two dimensional array for ground-based observations of auroral zone electric currents during the IMS, J. Geophys., **46**, 429, 1979.
- Liebelt, P. B., *An Introduction to Optimal Estimation*, pp. 135-185, Addison-Wesley Publishing Company, Reading, MA, 1967.
- Liu, A. T. Y., D. Venkatesan, C. D. Anger, S.-I. Akasofu, W. J. Heikkila, J. D. Winningham, and J. R. Burrows, Simultaneous observations of particle precipitations and auroral emission by the Isis 2 Satellite, J. Geophys. Res., **82**, 2210, 1977.
- Luhmann, J. G., Auroral bremsstrahlung spectra in the atmosphere, J. Atmos and Terr. Phy., **39**, 595, 1977.

- Maezawa, K., Magnetospheric convection induced by the positive and negative Z components of the interplanetary magnetic field: Quantitative analysis using polar cap magnetic records, J. Geophys. Res., 81, 2289, 1976.
- Maggs, J. E., and T. N. Davis, Measurements of the thickness of auroral structures, Planet. Space Sci., 16, 205, 1968.
- Marklund, L. G. Blomberg, K. Stasiewicz, J. S. Murphree, R. Pottelette, L. J. Zanetti, T. A. Potemra, D. A. Hardy, and F. J. Rich, Snapshots of High-latitude electrodynamics using Viking and DMSP F7 observations, J. Geophys. Res., 93, 14479, 1988.
- McPherron, R. L., C. T. Russell, M. G. Kivelson, and P. J. Coleman, Jr., Substorms in space: The correlation between ground and satellite observations of the magnetic field, Radio Sci., 8, 1059, 1973.
- McPherron, R.L., The use of ground magnetograms to time the onset of magnetospheric substorms, J. Geomag. Geoelectr., 30, 149, 1978.
- McPherron, R.L., Magnetic variations during substorms, in *Dynamics of the Magnetosphere*, ed. by S.-I. Akasofu, 631, Reidel, Hingman, Mass, 1979.
- McPherron, R.L., private communication, 1989.
- Mishin, V. M., A.D. Bazarzhapov, and G.B. Shpynev, Electric fields and currents in the Earth's magnetosphere, in *Dynamics of the Magnetosphere*, ed. by S.-I. Akasofu, 249, D. Reidel, Hingman, Mass, 1979.
- Mishin, V.M., S.B. Lunyushkin, D. Sh. Shirapov, and W. Baumjohann, A new method for generating instantaneous ionospheric conductivity models using ground-based magnetic data, Planet. Space Sci., 34, 713, 1986.
- Mizera, P. F., J. F. Fennell, D. R. Croley, A. L. Vampola, F. S. Mazer, R. B. Torbert, M. Temerin, R. L. Lysak, M. K. Hudson, C. A. Cattell, R. G. Johnson,

- R. D. Sharp, A. Ghielmetti, and P. M. Kintner, The auroral inferred from S3-3 particles and fields, J. Geophys. Res., 86, 2329, 1981a.
- Mizera, P. F., J. F. Fennell, D. R. Croley, and D. J. Gorney, Charged particle distributions and electric field measurements from S3-3, J. Geophys. Res., 86, 2329, 1981b.
- Moses, J. J., G. L. Siscoe, R. A. Heelis, and W. D. Winningham, Polar cap deflation during magnetospheric substorms, J. Geophys. Res., 94, 3785, 1989.
- Nagy, A. F., and P. M. Banks, Photoelectron fluxes in the ionosphere, J. Geophys. Res., 75, 6260, 1970.
- Nisbet, J., M. J. Miller, and L. A. Carpenter, Currents and electric fields, in the ionosphere due to field-aligned auroral currents, J. Geophys. Res., 83, 2647, 1978.
- Nishida, A., Geomagnetic DP2 fluctuations and associated Magnetospheric Phenomena, J. Geophys. Res., 73, 1795, 1968.
- Obayashi, T., and A. Nishida, Large-scale electric field in the magnetosphere, Space. Sci. Rev., 8, 3, 1968.
- Parkinson, W. D., and F. W. Jones, The Geomagnetic Coast Effect, Rev. Geophys. Space Phys., 17, 1999, 1979.
- Perreault, P. D., and S.-I. Akasofu, A study of geomagnetic storms, Geophys. J. R. Astron. Soc., 54, 547, 1978.
- Potemra, T. A., J. P. Dwyer, W. K. Peterson, C. O. Bostrom, R. A. Hoffman, and L. H. Brace, AE-C observations of low energy particle and ionospheric temperatures in the turbulent polar cusp: Evidence for the Kelvin-Helmholtz instability. J. Geophys. Res., 83, 3877, 1978.

- Potemra T. A., T. Iijima, and N. A. Saflekos, Large-scale characteristics of Birkeland currents, in *Dynamics of the Magnetosphere*, pp. 165, D. Reidel, Hingham, Mass., 1979.
- Pytte, T., R. L. McPherron and S. Kokobun, The ground signatures of the expansion phase during multiple onset substorms, Planet. Spa. Sci., 24, 1115, 1978.
- Rasmussen, C. E., R. W. Schunk, and V. B. Wickwar, A photochemical equilibrium model of ionospheric conductivity, J. Geophys. Res., 93, 9831, 1988.
- Rees, M. H., Auroral ionization and excitation by incident energetic electrons, Planet. Space Sci., 11, 1209, 1963.
- Rees, M. H., and R. A. Jones, Time dependent studies of the aurora-II. spectroscopic morphology, Planet. Spa. Sci., 21, 1213, 1973.
- Rees, M. H., D. Lummerzheim, R. G. Roble, J. D. Winningham, J. D. Craven and L. A. Frank, Auroral energy deposition rate, characteristic electron energy and ionospheric parameters derived from Dynamics Explorer 1 images, J. Geophys. Res., 93, 12841, 1988.
- Reiff, P. H., and J. L. Burch, B_y -dependent dayside plasma flow and Birkeland currents in the dayside magnetosphere: 2. A global model for northward and southward IMF, J. Geophys., 90, 1595, 1985.
- Reiff, P. H., and J. G. Luhmann, Solar wind control of the polar cap voltage, in, *Solar-Wind Magnetosphere Coupling*, edited by Y. Kamide and A. Slavin, pp. 453-494, Terra Scientific Publishing Company, Tokyo, 1986.
- Rich, F.J., M.S. Gussenhoven, M.E. Greenspan, Using simultaneous particle and field observations on a low altitude satellite to estimate Joule heat energy flow into the high latitude ionosphere, Ann. Geophys., 5, 527, 1987.

- Richmond, A. D., Large-amplitude gravity wave energy production and dissipation in the thermosphere, J. Geophys. Res., 84, 1880, 1979.
- Richmond, A. D., S.-I. Akasofu, D. Alcayde, M. Blanc, O. de la Beaujardiere, D. S. Evans, J. C. Foster, E. Friis-Christensen, J. M. Holt, Y. Kamide, R. J. Pellinen, C. Senior, A. N. Zaitzev, Global measures of ionospheric electrodynamic activity inferred from combined incoherent-scatter radar and ground magnetometer observations, submitted to J. Geophys. Res., 1989.
- Richmond, A. D., and W. Baumjohann, Three-dimensional analysis of magnetometer array data, J. Geophys., 54, 138, 1983.
- Richmond, A. D., and Y. Kamide, Mapping electrodynamic features of the high-latitude ionosphere from localized observations: Technique, J. Geophys. Res., 93, 5741-5759, 1988.
- Richmond, A. D., Y. Kamide, B.-H. Ahn, S.-I. Akasofu, D. Alcayde, M. Blanc, O. de la Beaujardiere, D. S. Evans, J. C. Foster, E. Friis-Christensen, T. J. Fuller-Rowell, J. M. Holt, D. Knipp, H. W. Kroehl, R. P. Lepping, R. J. Pellinen, C. Senior, A. N. Zaitzev, Mapping electrodynamic features of the high-latitude ionosphere from localized observations: Combined incoherent scatter radar and localized observations: Measurements for January 18-19, 1984, J. Geophys. Res., 93, 5760, 1988.
- Richmond, A. D., private communication 1989.
- Robinson, R. M., and R. R. Vondrak, Measurements of E region ionization and conductivity produced by solar illumination at high latitudes, J. Geophys. Res., 89, 3951, 1984.
- Robinson, R. M., R. R. Vondrak, K. Miller, T. Dabbs, and D. Hardy, On calculating ionospheric conductances from the flux and energy of precipitating electrons, J. Geophys. Res., 92, 2565, 1987.

- Robinson, R. M., R. R. Vondrak, J. D. Craven, L. A. Frank and K. Miller, A comparison of ionospheric conductances and auroral luminosities observed simultaneously with the Chatanika radar and the DE 1 auroral imagers, J. Geophys. Res., 94, 5382, 1989.
- Roble, R. G., R. E. Dickinson and E. C. Ridley, Global circulation and temperature structure of the thermosphere with high-latitude plasma convection, J. Geophys. Res., 87, 1599, 1982.
- Rosenburg, T. J., D. L. Detrick, P. F. Mizera, D. J., Gorney, F. T. Berkey, R. H. Eather and L. J. Lanzerotti, Coordinated ground and space measurements of an auroral surge over south pole, J. Geophys. Res., 92, 11123, 1987.
- Rostoker, G., Electric and magnetic fields in the ionosphere and magnetosphere, J. Geomag. Geoelectr., 30, 67, 1978.
- Rostoker, G., The role of magnetospheric substorms in magnetosphere-ionosphere coupling, in *The Solar Wind and the Earth*, edited by S.-I. Akasofu and Y. Kamide, 163, Terra Scientific Publishing Co., Tokyo, Japan, 1987.
- Rostoker, G., and T. J. Hughes, A comprehensive model current system for high latitude magnetic activity, Geophys. J. R. Astron. Soc., 58, 571, 1979.
- Russell, C. T., The configuration of the magnetosphere, in *Critical Problems of Magnetospheric Physics*, ed. by E. R. Dyer, pp. 1-16, Inter-Union Commission on Solar-Terrestrial Physics Secretariat, National Academy of Sciences, Washington, D. C., 1972.
- Russell, C.T., and R.L. McPherron, The magnetotail and substorms, Space Sci. Rev., 15, 205, 1973.
- Shepherd, G. G., Dayside cleft aurora and its ionospheric effects. Rev. Geophys. Space Phys., 17, 2017, 1979.

- Sonnerup, B. U. Ö., Magnetic field reconnexion in a highly conducting incompressible fluid, J. Plasma. Phy., 4, 161, 1970.
- Speiser, T. W., Particle trajectories in model current sheets, II: Application to auroras using geomagnetic tail model, J. Geophys. Res., 72, 3919, 1967.
- Spiro, R.W., P.H. Reiff, and L.J. Maher, Precipitating electron energy flux and auroral zone conductivities--An empirical model, J. Geophys. Res., 87, 8215, 1982.
- Stamnes, K., Analytical approach to auroral electron transport and energy degradation, Planet. Space Sci., 28, 427, 1980.
- Stamnes, K., A unified theory of interhemispheric electron transport and energy degradation, Geophysica Norvegica, 33, 41, 1985.
- Stenbaek-Nielsen, H. C., E. M. Wescott, T. N. Davis, and R. W. Peterson, Differences in auroral intensity at conjugate points, J. Geophys. Res., 78, 659, 1973.
- Strickland, D. J., D. L. Book, T. P. Coffey, and J. A. Fedder, Transport equation techniques for the deposition of auroral electrons, J. Geophys. Res., 81, 275, 1976.
- Sugira, M., and T. A. Potemra, A net field-aligned current observed by TRIAD, J. Geophys. Res., 81, 2155, 1976.
- Swift, D. W., Mechanisms for auroral precipitation: A review, Rev. Geophys. Space Phys., 19, 185, 1981.
- Vickery, J. F., R. R. Vondrak, and S. J. Matthews, The diurnal and latitudinal variation of auroral zone ionospheric conductivity, J. Geophys. Res., 86, 1225, 1981.

- Wallis, D.D., Comparison of auroral electrojets and the visible aurora, in *Magnetospheric Particles and Fields*, ed. by B. M. McCormac, 247, Reidel, Hingham, MA, 1976.
- Wallis, D. D. and E. E. Budzinski, Empirical models of height integrated conductivities, J. Geophys. Res., **86**, 125-137, 1981.
- Wickwar, V. B., J. D. Kelly, O. de la Beaujardiere, C. A. Leger, F. Steenstrup, and C. D. Dawson, Sondrestrom overview, Geophys. Res. Lett., **11**, 883, 1984.
- Winningham, J. D., F. Yasuhara, S.-I. Akasofu, and W. J. Heikkila, The latitudinal morphology of 10-eV to 10-keV electron fluxes during magnetically quiet and disturbed times in the 2100-0300 MLT sector, J. Geophys. Res., **80**, 3148, 1975.
- Yasahura, F., Y. Kamide and S.-I. Akasofu, Field-aligned and ionospheric currents, Planet. Spa. Sci., **23**, 1355, 1975.
- Yasahura, F., and S.-I. Akasofu, Field-aligned currents and ionospheric electric fields, J. Geophys. Res., **82**, 1279, 1977.
- Zanetti, L. J. and T. A. Potemra, The relationship of Birkeland and ionospheric current systems to the interplanetary magnetic field, in *Solar Wind Magnetosphere Coupling*, ed. by Kamide and Slavin, 547, 1986.